Carbon Nanotubes: Electrons in One Dimension

by

Marc William Bockrath

B.S. (Massachusetts Institute of Technology) 1993

A dissertation submitted in partial satisfaction of the requirements

for the degree
of

Doctor of Philosophy
in

Physics

In the

GRADUATE DIVISION

of the

UNIVERSITY OF CALIFORNIA, BERKELEY

Committee in charge:

Professor Paul McEuen, Chair
Professor Steven Louie
Professor Gabor Somorjai

Fall 1999

Abstract

Carbon Nanotubes: Electrons in One Dimension

by

Marc William Bockrath

Doctor of Philosophy in Physics

University of California, Berkeley

Professor Paul McEuen, Chair

The work presented in this thesis will discuss transport measurements on individual single-walled nanotubes (SWNTs) and SWNT bundles. SWNTs, which are essentially rolled-up sheets of graphite, are either one-dimensional (1D) metals or 1D semiconductors depending on how they are rolled-up. Measurements on both metallic and semiconducting SWNTs will be presented.

Chapter 1 will present an introductory overview to the thesis, discussing prior related experimental work and introducing basic concepts that are used in subsequent chapters. Chapter 2 discusses the experimental methods we have used to study transport in SWNTs.

Chapters 3 and 4 discuss low temperature measurements of metallic SWNTs. Chapter 3 will discuss the low temperature behavior of the conductance of a SWNT bundle, or rope, that shows quantum mechanical effects resulting from the finite size of the sample. Chapter 4 will discuss how these finite size effects can be used to experimentally study the quantum level structure in metallic nanotubes and the effects of an applied magnetic field.

In chapters 5 and 6, we discuss transport measurements of semiconducting SWNTs. In chapter 5, we show that semiconducting SWNTs can be doped with potassium. Chapter 6 presents experiment and theory that indicate that the elastic mean free path in metallic tubes is far longer than in semiconducting tubes.

Chapters 7 and 8 address the effects of electron-electron (e-e) interactions on the transport properties of metallic SWNTs. Chapter 7 discusses some theoretical aspects of 1D wires when e-e interactions are taken account, giving a simplified picture of the Luttinger-liquid state expected for a 1D system of interacting electrons. Finally, chapter 8 will discuss measurements on metallic samples with extremely long mean free paths. These experiments show evidence of this Luttinger-liquid behavior, in which the electron-electron interactions lead to a qualitatively different ground state than what would be expected with Fermi-liquid theory.

To my parents

Acknowledgments

The work of this thesis has been largely a collaborative effort. While there are many people to thank for their contributions, I would first like to thank my advisor Paul McEuen. His insight into physics (and everything else!) has been a constant source of inspiration. I am grateful that I have had the opportunity to learn from him.

I also owe a large debt of gratitude to Dave Cobden. His hard work and guidance were crucial in ensuring the success of these experiments. If not for his efforts, this thesis would have been much shorter.

The potassium doping experiments would not have happened if not for Jim Hone. Thanks to his efforts, we were able to get data in record time. I would also like to thank Jia Lu for providing nanotube samples that permitted clear observations of Luttinger liquid behavior.

Overall, our efforts have been accelerated by the contributions of Steve Louie, Young-Gui Yoon, and Leon Balents, who provided theoretical support. Of course, research on nanotubes would not be possible without nanotubes -- Nasreen Chopra, Alex Zettl, Andreas Thess, Andrew Rinzler, and Richard Smalley have provided us with the invaluable material as well as helpful discussions.

Finally, I would also like to thank my co-workers for making the lab an exciting and stimulating place to work. In particular, I would like to thank Hongkun Park for his guidance (scientific and otherwise), encouragement, and rides up the hill.

Outside of the lab, I am grateful that I have had the support of my family and friends for these years. Also, I can not thank Debbie enough for her support and encouragement. I will always cherish our time together here.

Table of Contents

Chapter 1

Carbon Nanotubes: Electrons in One Dimension

1.1 Introduction

The dimensionality of a system has a profound influence on its physical behavior. With advances in technology over the past few decades (*e.g.* molecular beam epitaxy), it has become possible to fabricate and study reduced-dimensional systems in which electrons are strongly confined in one or more dimensions. The study of reduced-dimensional systems has yielded many important new results. This is evident from Fig. 1-1, which shows a table of the properties of systems with different dimensionalities. As can be seen from the table, much of the basic physics of electrons in any dimension can be understood in terms of non-interacting electrons in a perfect crystal. For example, non-interacting electrons models can explain why bulk Si is a semiconductor or why two-dimensional (2-D) graphene is a semi-metal.

However, many striking phenomena require models that go beyond the above simple picture. When considering such models the dimension of the system plays an important role. For example, in three dimensions (3-D) it is possible for electrons to remain delocalized even in the presence of disorder, unlike in one-dimensional (1-D) systems. The dimensionality is no less important in determining the effects of electron-electron interactions. For a 3-D electron system, unless the interactions are very strong, the low energy excitations from the ground state behave

Interacting Electrons in Solids

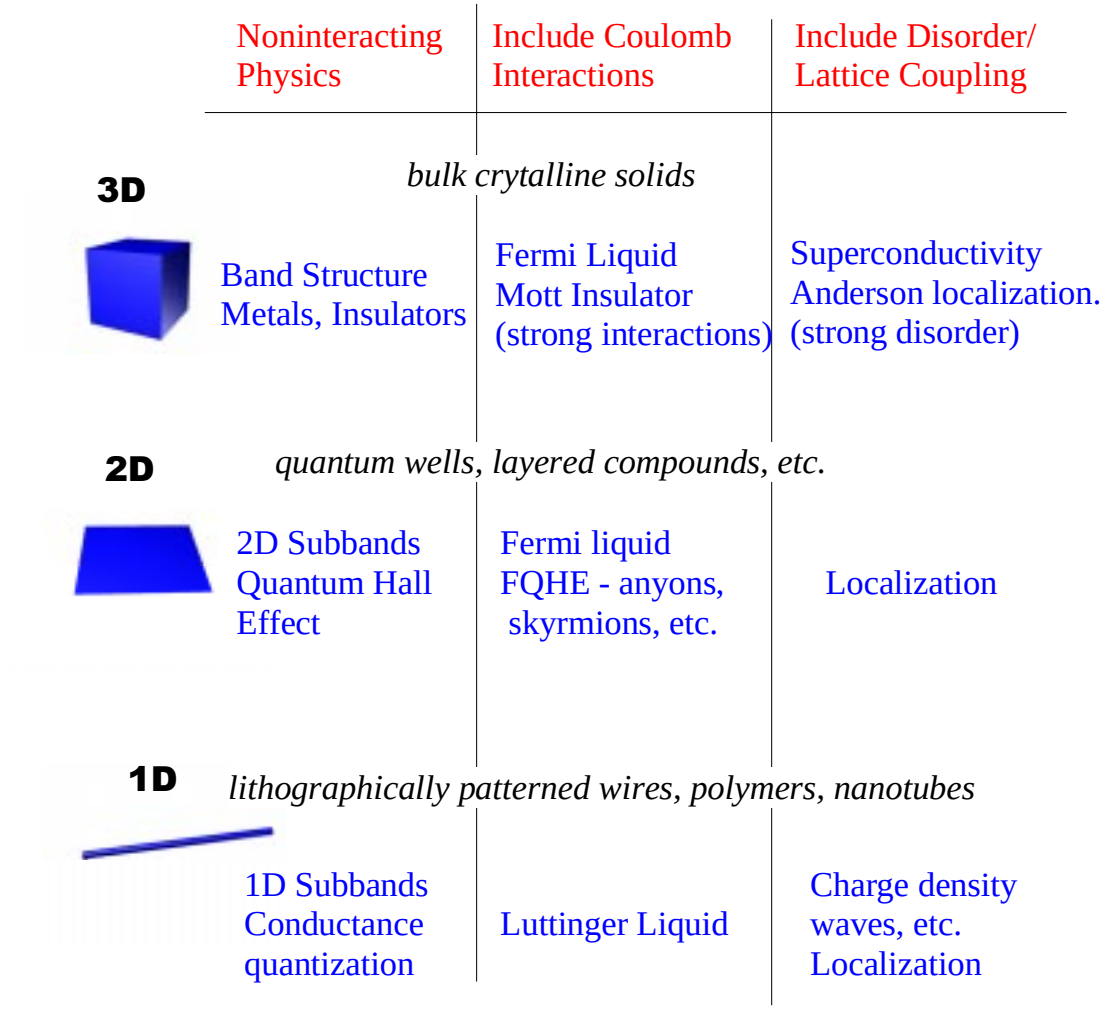

Figure 1-1: Electronic systems in varying dimensions. While the non-interacting electron picture explains many of the basic features, many phenomena require including the effects Coulomb interactions, particularly in reduced dimensions.

essentially like weakly interacting electrons. This is the well-known Fermi-liquid behavior; electron-electron interactions do not qualitatively change the picture given by the independent electron model.

Electrons in 2-D at low magnetic fields are also well described by Fermi-liquid theory. This has been demonstrated by a wealth of experiments on 2-D electron gasses in GaAs heterojunctions. When a magnetic field is applied, the single-particle states are Landau levels, which are then filled with electrons up to the Fermi level. The number of filled Landau levels at a given magnetic field is referred to as the filling factor ν. When ν is an integer greater than one, the electrons behave like a Fermi liquid, as in the integer quantum Hall effect (IQHE). However, at high magnetic fields when only one Landau level is partially filled, the fractional quantum Hall effect is observed. Unlike the IQHE, understanding the FQHE requires the inclusion of electron-electron interactions. Coulomb interactions break the degeneracy of the lowest Landau level leading to a unique ground state and a gap for excitations. These excitations can be very different from the bare electrons, having for example fractional charge. Unlike a 3-D electron system, a 2-D electron system is qualitatively altered by the effects of electron-electron interactions.

The study of 1-D electron systems based on *e.g.*, semiconductor wires or constrictions has also yielded important results. Most of these results, such as conductance quantization, have been explained in terms of non-interacting electrons. Unlike in 2-D and 3-D, however, the question of what role e-e interactions play in real 1-D systems has been difficult to address, because of the difficulty in obtaining long, relatively disorder-free 1-D wires. Nevertheless, the prediction of dramatic effects in 1-

D due to e-e correlations has motivated a lengthy search for a good experimental realization of a 1-D system. At last, single-walled carbon nanotubes (SWNTs) have emerged as a material that promises to overcome these difficulties and provide a model system for the study of electrons in 1-D.

1.2 Brief History of Carbon Nanotubes

The history of SWNTs begins with the discovery of multi-walled carbon nanotubes (MWNTs.) MWNTs were first observed by transmission electron microscopy (TEM) in carbon-arc soot by Iijima in 1991 [1]. These micron-long nanotubes consisted of two or more concentric shells and range in outer diameter from ~2-20 nm (see Fig. 1-2A-B). Soon after, techniques were developed to increase the yield of nanotube material[2]. Approximately two years after the discovery of MWNTs, single-walled nanotubes (SWNTs) consisting of only a single shell of carbon atoms were discovered independently by Iijima and by Bethune[3, 4]. In contrast to MWNTs, the typical diameter of these SWNTs was ~ 1 nm. Later work enabled the bulk production of ~1 nm diameter SWNTs[5]. Figure 1-2C shows an image of an isolated SWNT. The bulk production of these nanotubes has led to a vast array of experiments exploring their chemical, mechanical, and electrical properties. Here we will concentrate on the electrical properties.

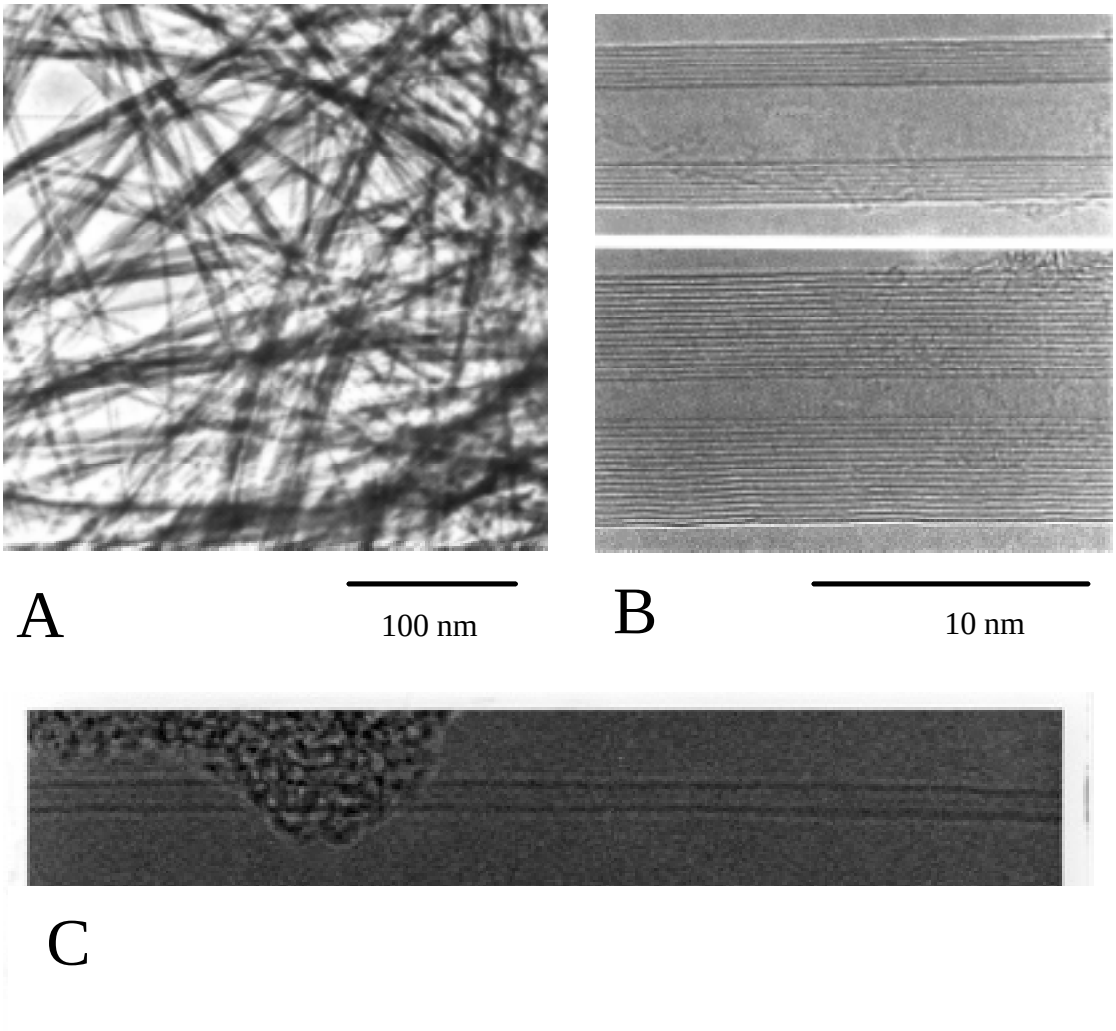

Figure 1-2: A) TEM images of multi-walled nanotubes. Image is a few hundred nanometers by few hundred nanmeters. B) High resolution TEM image of Multi-walled nanotubes showing the concentric walls of the two nanotubes and hollow core. C) TEM image of an individual 1.4 nm diameter single-walled nanotube.

1.3 Nanotube Band structure

A SWNT is essentially a single 2-D layer of graphite (a graphene sheet) rolled into a tube. Graphene is an sp^2 bonded network of carbon atoms arranged in a hexagonal lattice with two atoms per unit cell. This is shown in Fig. 1-3A, which depicts the honeycomb lattice in which a carbon atom is located at each vertex. Figure 1-3A also shows the primitive lattice vectors $\mathbf{a}_1$ and $\mathbf{a}_2$, as well as the lattice constant a. A nanotube of a particular radius and chirality may be specified by choosing a "roll-up" vector that maps two given hexagons in the lattice on top of each other. The blue arrows in Fig. 1-3A show an example of this for the two hexagons shown in gray. Since any vector connecting two hexagons in the lattice is a Bravais lattice vector, it is a linear combination of the primitive vectors with integer weight. Thus, a given nanotube is associated with two indices that specify these integers. The nanotube formed by identifying the two gray hexagons in Fig. 1-3A would thus be a (3,1) nanotube. Note that this indexing scheme is one of convention as the choice of primitive lattice vectors is not unique. However, this scheme appears to be the most commonly used in the literature. Figure 1-3B shows how a (10,10) nanotube may be rolled up from graphene.

For a very large radius tube, one might expect that the properties of the tube are very similar to that of graphene. It has been found that even for very small diameter tubes (~1 nm) that the basic electronic properties of nanotubes may be deduced from the band structure of graphene[6]. Figure 1-4 shows this band structure in the first Brillouin zone. Since there are two atoms per unit cell, the lower band is completely

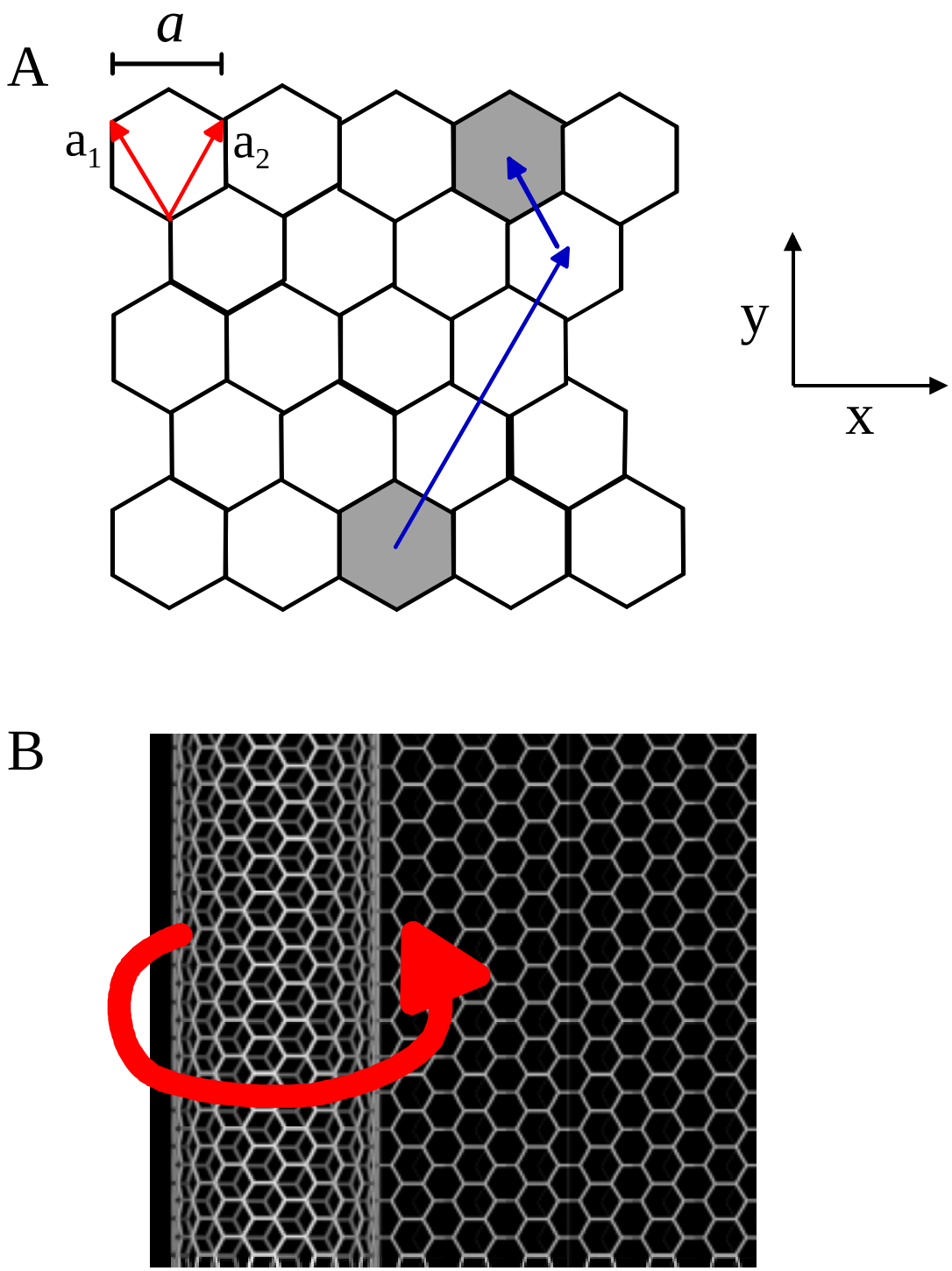

Figure 1-3: A) Lattice parameters for graphene: $\mathbf{a}_1$ and $\mathbf{a}_2$ are the Bravais lattice vectors, a = .243 nm is the lattice constant, and the blue arrows show how a (3,1) nanotube may be formed by rolling the hexagons shown in gray on top of each other. B) A (10,10) nanotube rolled up from graphene

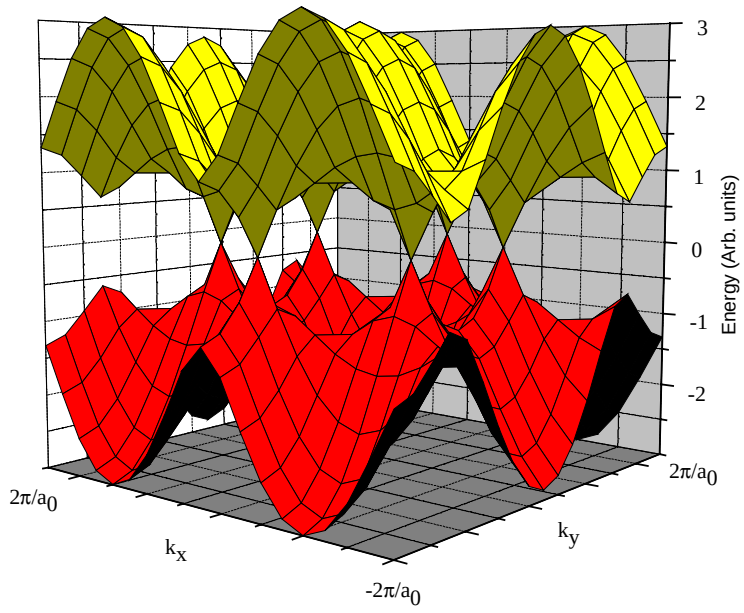

Figure 1-4: Graphene band structure. The conduction and valence bands touch at the six Fermi points indicated. Because there are two electrons per unit cell, the valence band is filled and the conduction band is empty. Graphene is thus a zero gap semiconductor, or semimetal.

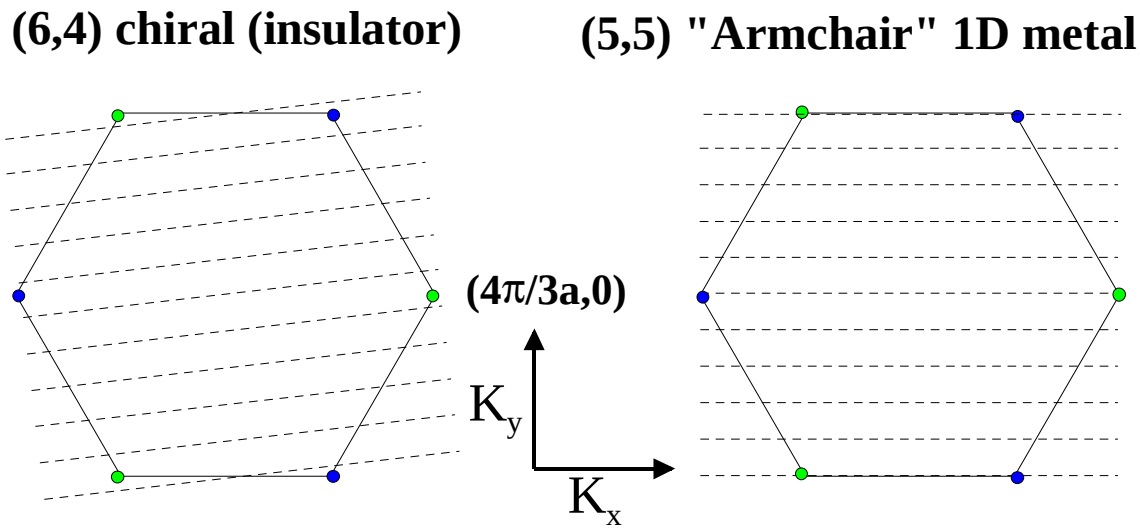

Figure 1-5: In a nanotube, the periodic boundary conditions quantize the allowed *k*-values. The nanotube may be insulating or metallic depending on whether the Fermi points coincide with an allowed *k*-value.

filled. The Fermi surface then consists of two inequivalent Fermi points at the opposite corners of the hexagonal Brillouin zone where the conduction band (CB) and valence band (VB) touch. The six points where the CB and VB touch shown in Fig. 1-4 are obtained by translating the two inequivalent points by reciprocal lattice vectors.

In the simplest possible model, the band structure of nanotubes can be derived directly from the band structure of graphene. This is accomplished by imposing strictly periodic boundary conditions for translations by the roll-up vector that defines the nanotube. The allowed $\boldsymbol{k}$ values are then quantized in the direction perpendicular to the roll-up vector $\boldsymbol{R}$: $\boldsymbol{k}\bullet\boldsymbol{R} = 2\pi n$, where n is an integer. Thus, the band structure of a nanotube consists of 1-D subbands. For a 1 nm diameter tube the subband splitting is expected to be on the order of one eV[7], and therefore nanotubes are expected to be truly 1-D materials. Figure 1-5 depicts these allowed $\boldsymbol{k}$ values for a (5,5) tube and a (6,4) tube. The nanotube will have a band gap unless the lines of allowed $\boldsymbol{k}$ pass though the two gapless points. Thus, the (5,5) tube is metallic while the (6,4) tube is semiconducting, despite the fact that their radii are identical to within less than 1%. In general, an (n,m) nanotube will have a band gap unless n-m = 3p, where p is an integer[6-8]. This behavior may also be derived within the context of a low-energy effective theory[9]. Effects due to curvature result in corrections to this picture. For example, some tubes that the above model would predict to be metallic may actually develop a small band gap. However, since these effects have not been observed experimentally, we will not discuss them here, but refer to the literature (see *e.g.* [9-11].)

1.4 Experimental Work

STM experiments on individual ~1 nm SWNTs have been able to provide conclusive evidence for the above theoretical picture[12, 13]. In these experiments, both the atomic structure and the tunneling spectra for a variety of nanotubes could be simultaneously measured. The picture given above was found to describe the experimental results quite well. Depending on the chirality of the nanotube, they were either metallic or had a band gap of ~0.6 eV. Furthermore, Van Hove singularities in the density of states were observed at the band edges arising from the one-dimensionality of the nanotubes. In addition to the STM work, resonant Raman scattering[14] and transport experiments (for review see *e.g.* [15]) have also supported this picture.

A number of these transport experiments will be discussed in the remainder of this thesis. Some of the chapters describing these experiments have appeared previously as publications. Specifically, Chapter 3 has been published as Science **275** 1922 (1997), Chapter 4 as Phys. Rev. Lett. **81** 681 (1998), and Chapter 8 as Nature **397** 598 (1999). Other chapters have been submitted for publication but have not yet appeared. Chapter 5 has been submitted to Applied Physics Letters, and Chapter 6 has been submitted to Physical Review Letters

References

1 S. Iijima, Nature **354**, 56 (1991).

2 T. W. Ebbesen and P. M. Ajayan, Nature **358**, 220 (1992).

3 S. Iijima and T. Ichihashi, Nature **363**, 603 (1993).

4 D. S. Bethune, C. H. Kiang, M. S. deVries, *et al*., Nature **363**, 605 (1993).

5 A. Thess, R. Lee, P. Nikolaev, *et al*., Science **273**, 483 (1996).

6 R. Saito, M. Fujita, G. Dresselhaus, *et al*., Applied Physics Letters **60**, 2204 (1992).

7 N. Hamada, S. Sawada, and A. Oshiyama, Physical Review Letters **68**, 1579 (1992).

8 J. W. Mintmire, D. H. Robertson, and C. T. White, Journal of the Physics and Chemistry of Solids **54**, 1835 (1993).

9 C. L. Kane and E. J. Mele, Physical Review Letters **78**, 1932 (1997).

10 X. Blase, L. X. Benedict, E. L. Shirley, *et al*., Physical Review Letters **72**, 1878 (1994).

11 L. Balents and M. P. A. Fisher, Physical Review B **55**, R11973 (1997).

12 J. W. G. Wildoer, L. C. Venema, A. G. Rinzler, *et al*., Nature **391**, 59 (1998).

13 T. W. Odom, H. Jin-Lin, P. Kim, *et al*., Nature **391**, 62 (1998).

14 A. M. Rao, E. Richter, S. Bandow, *et al*., Science **275**, 187 (1997).

15 C. Dekker, Physics Today **52**, 22 (1999).

Chapter 2

Experimental Techniques

2.1 Sample Preparation

As discussed in the introduction, SWNTs represent a ready-made 1-D electron system. Thus, all that is required to study the electrical properties of electrons in 1-D is to connect these nanotubes to external wires. This section will describe how we attach leads to individual nanotubes or nanotube bundles and make electrical measurements.

We begin with the raw "felt" material, which is shown in Figure 2-1A. We obtain this material from Professor Richard Smalley and co-workers at Rice University, where it is made by laser vaporizing carbon along with small amounts of Co and Ni, which act as a catalyst. Closer inspection with a scanning electron microscope (SEM) such as shown in Fig. 2-1B reveals that the felt material consists of very long, tangled strands. These strands are bundles of SWNTs as shown in cross section in Fig. 2-1C. They consist of 2D hexagonally packed SWNTs of a nearly monodisperse diameter ~1 nm. An isolated individual SWNT is shown in Fig. 2-1D. In order to make electrical measurements of single nanotubes or few-nanometer bundles, the individual nanotubes or bundles must first be isolated from the felt.

To accomplish this, the raw felt material shown in Fig. 2-1A is placed in a liquid and exposed to ultrasound. The ultrasound produces microscopic bubbles in the liquid.

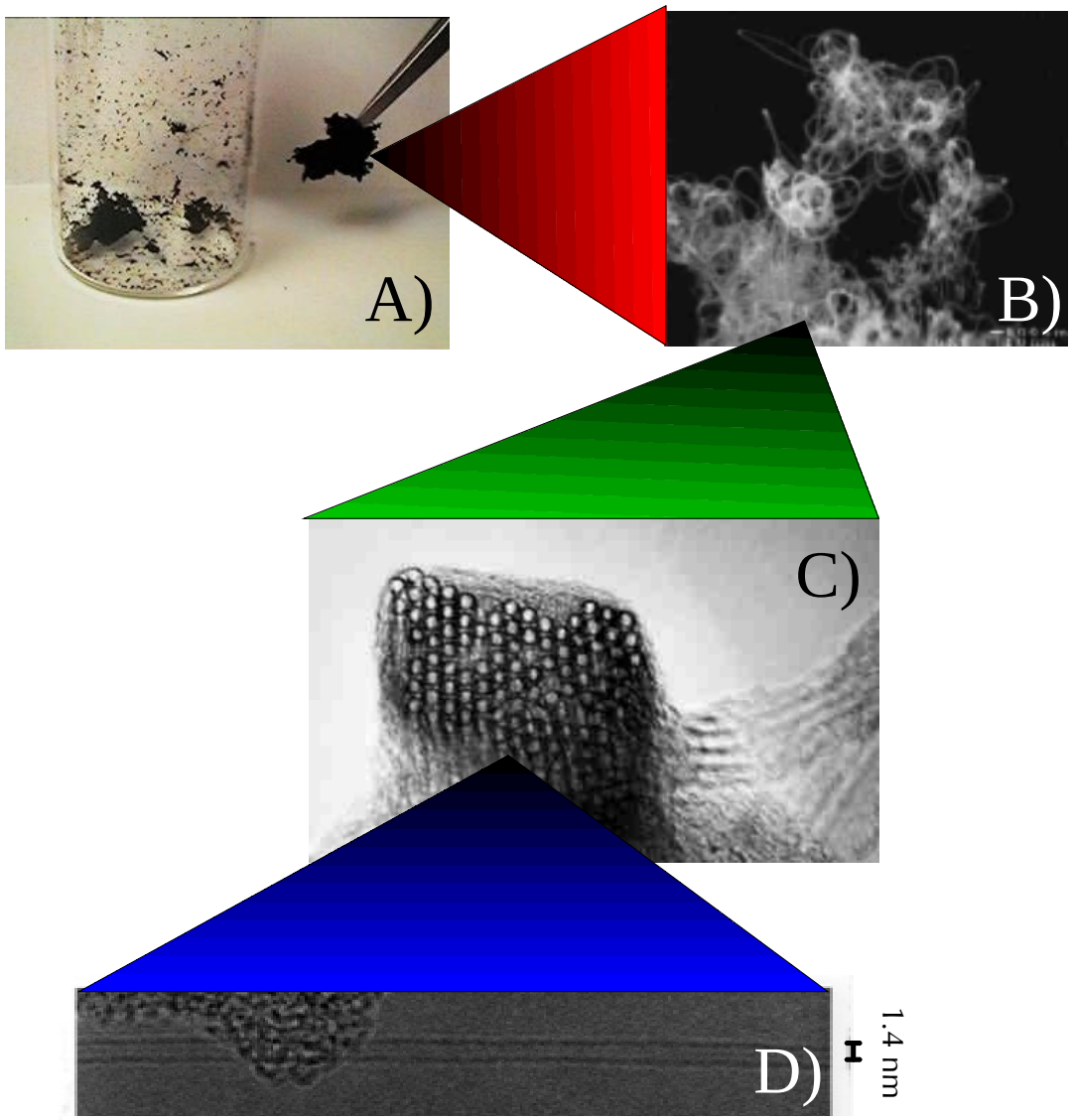

Figure 2-1: Single walled nanotube material shown at various levels of magnification. A) Nanotube material as it appears on a macroscopic scale. B) At the lowest level of magnification, the material appears as a tangled mass of rope-like strands. (Image from R. E. Smalley.) C) Higher magnification reveals bundles of SWNTs arranged in a hexagonal 2D lattice. (Image from R. E. Smalley.) D) The highest level of magnification shows a side view of a single 1.4 diameter SWNT. (Image from Nasreen Chopra.)

When these bubbles collapse, the resulting shock waves serve to cut the ropes and disperse them in the solvent. The diameter of the bundles, the prevalence of single nanotubes, and the degree to which they are untangled by this procedure depends critically on precisely which solvent is used. It has been found that 1,2 Dichloroethane (DCE) is an excellent solvent in this regard. Ultrasounding the felt material in DCE results in a suspension of nanotubes and bundles with a spectrum of lengths ranging from < 1 μm to ~ 10 μm, and diameters in the 1-10 nm range. Presently, it is not understood why DCE works so well. However, the attractive forces between suspended particles in a liquid depends on many physical properties of the liquid, such as the dielectric constant, the surface energies of the solvent and solute, etc. Thus, it is not surprising that different liquids will have different levels of effectiveness at suspending nanotubes and preventing them from coalescing.

Once the nanotubes are suspended in DCE, they can be deposited on a surface by placing a drop of the suspension on a substrate. It is found that nanotubes suspended in DCE will readily adhere to SiO_2 by Van der Waals forces. After a few seconds and before the DCE dries, the suspension is rinsed away with 2-propanol (IPA). This results in a relatively uniform coverage of nanotubes on the surface. Once the IPA is blown dry, the tubes remain immobilized on the surface. Figure 2-2 shows an atomic force microscope (AFM) image of silicon dioxide with tubes deposited in this way.

To attach leads to the nanotubes, we start with a degenerately doped Si wafer that has 1 μm of thermal oxide grown on the surface. Optical lithography is used to etch

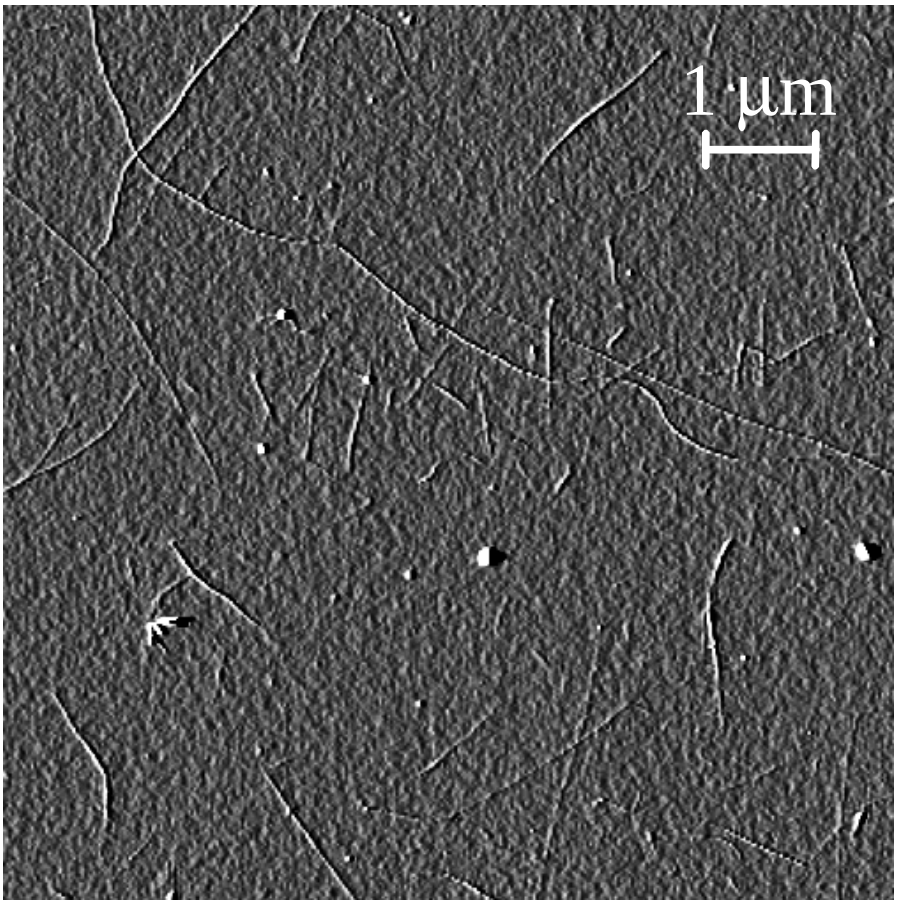

Figure 2-2: AFM image of tubes and ropes on SiO_2. Faintest objects are ~1 nm in height. (Image courtesy of Michael Fuhrer.)

holes in the oxide and define Al contacts to the degenerately doped Si, which is used as a gate. In this procedure, the wafer is first covered with photoresist. Exposure to UV light through a mask chemically changes the resist. The pattern defined by the mask is then developed to produce holes in the resist layer. The wafer is then immersed in HF, which removes the exposed oxide. Finally, Al is evaporated onto the wafer, and then the unwanted metal is removed by lift-off. These steps are shown in Fig. 2-3A-C.

Starting with this wafer with back gate contacts, making electrical contact to the nanotubes is then done in either of two ways. In the first method[1], leads are first defined using a combination of optical lithography and electron-beam lithography (EBL) to make an array of 42 junctions on a few-mm by few-mm chip. Tubes are deposited on top of the leads, as is shown schematically in Fig. 2-3D and 2-3E. Promising candidate devices are then found by using a probe station to test the electrical properties. These devices are then examined with an AFM to determine the number and size of the nanotubes/bundles bridging the contacts. Figure 2-4A shows a device made using this technique.

In the second method[2], nanotubes are deposited on an oxidized Si wafer that has pre-defined alignment marks in addition to the back gate contacts. These alignment marks consist of ~ 1 μm Au squares that were formed in a prior lithography step. A suitable tube or bundle is located with an AFM, and its position is noted relative to the alignment marks. A resist polymer (either PMMA or PMMA/MAA) is then spun on the sample and leads to the nanotubes are defined with EBL. A completed device is shown in Figure 2-4B.

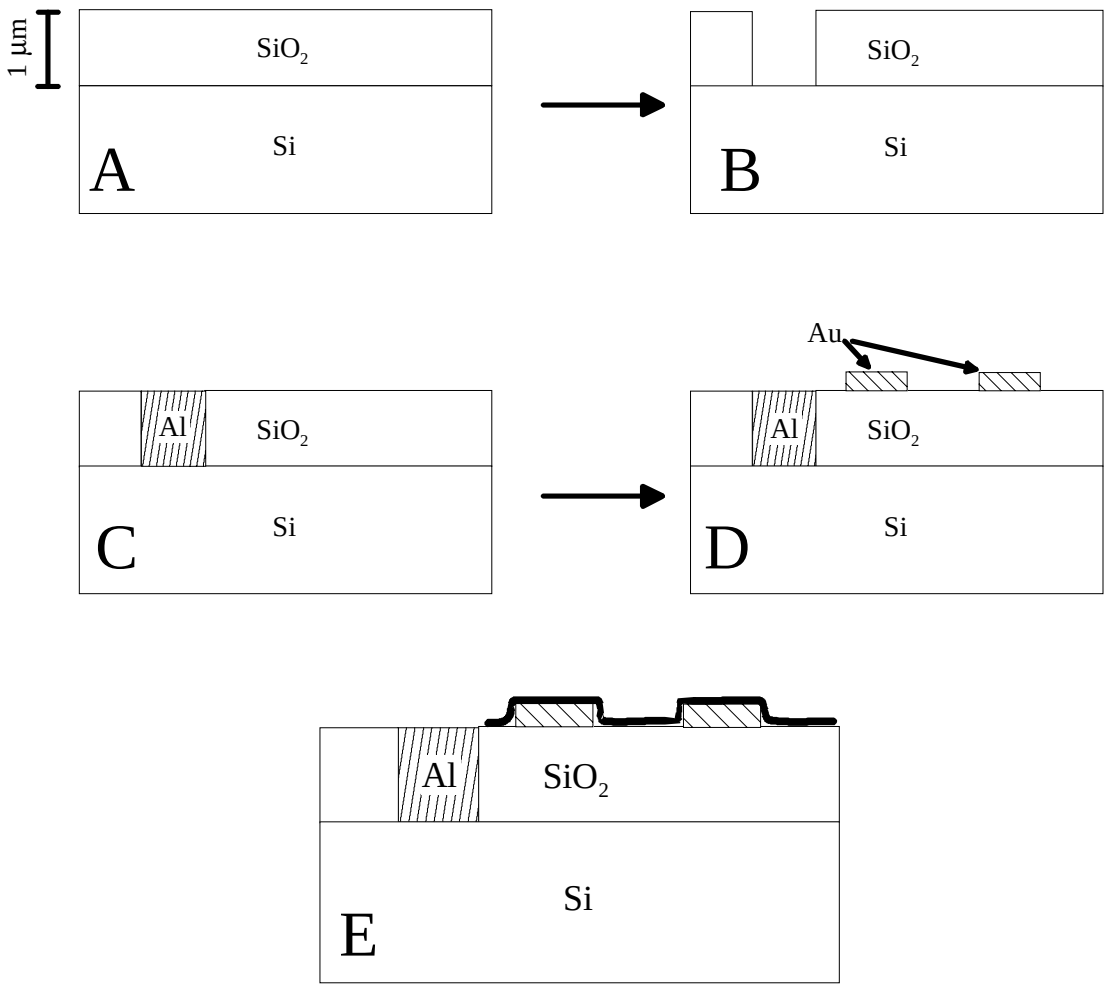

Figure 2-3: Fabrication steps for a nanotube device. A) Starting substrate consisting of a degenerately doped Si wafer with 1 μm of thermally grown oxide. The degenerately doped Si is used as a gate electrode. B) optical lithography and an HF etch creates windows in the oxide layer. C) Contact to the gate is made by evaporating Al through the windows. D) Leads are defined using a combination of optical and e-beam lithography. E) Nanotubes are deposited on the leads to form the completed device.

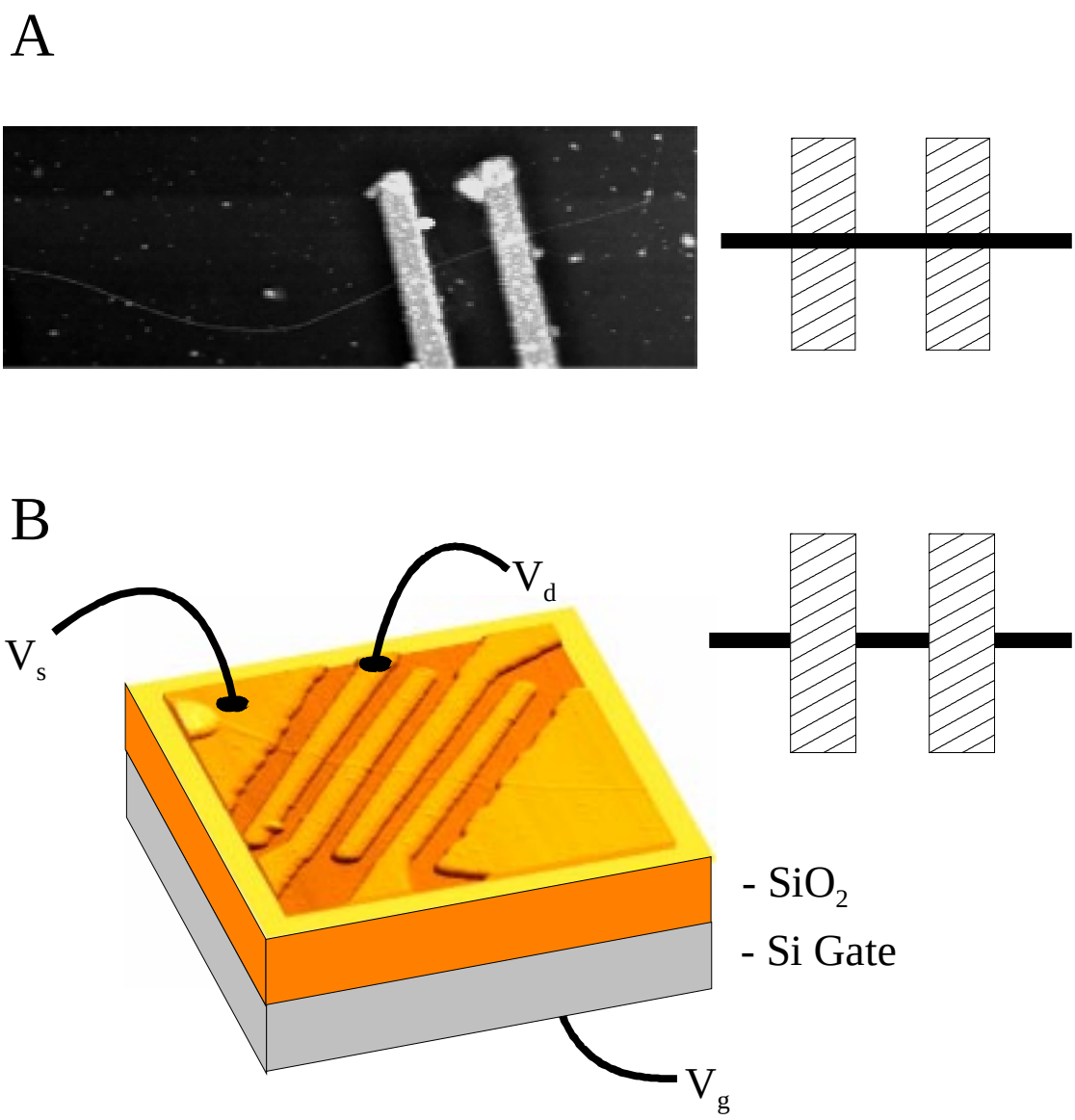

Fig 2-4: A) A device made by depositing the tubes on top of the leads. B) A device made by evaporating the leads on top of the nanotubes. The source and drain leads are shown as well as the lead to the back gate.

In either method, once the leads have been attached, the device is mounted in a chip package using colloidal silver paint. Electrical contact between the bonding pads on the chip and the package is made by 2-mil Al wire, using ultrasonic wire bonding. Finally, the package can then be inserted into standard 16-pin sockets and is ready for electrical measurements.

2.2 Low Temperature Electrical Measurements

Making transport measurements of the samples requires that we apply voltages and measure the resulting currents. To apply voltages to the sample, we use a standard Windows PC computer with a National Instruments analog-to-digital (ADC) and digital-to-analog (DAC) converter card. The voltages are applied via the output from the DACs, which are software controlled. Using multiple DACs allows both a source-drain voltage to be applied as well as a voltage on the gate. The current is measured using an Ithaco current pre-amplifier that outputs a voltage proportional to the measured current. This output voltage is read by the ADC and data acquisition software allows the data to be plotted in real time.

The DACs can produce independent voltages from –10 V to +10 V with approximately 0.5 mV resolution. Typically, the voltage applied to the sample is < 100 mV, and thus using the full range of the DAC is seldom necessary. Hence, depending on the desired bias, the DAC output voltage can be divided down with a resistive divider before appearing across the sample to sacrifice the full range of voltage for increased resolution. For example, dividing by 100 gives a full range of –100 mV to

+100 mV with 5 μV resolution. A schematic of the typical measurement circuit is shown in Figure 2-5.

To enable low-temperature measurements of nanotube devices, we have employed several different methods. The simplest method involves dipping the package into a partially filled liquid ^{4}He dewar. By raising the sample above the liquid level, the sample can be brought to equilibrium at different temperatures. The temperature is measured by mounting a resistance thermometer near the sample. This allows measurements over a temperature range from 4.2 K to approximately room temperature.

For increased thermal stability and a temperature range from 1.4 K to 280 K, we use an Oxford variable temperature system. This cryostat is designed to work while immersed in liquid ^{4}He (LHe.) The sample is isolated from the LHe by a vacuum jacket. However, ^{4}He may enter the sample space through a motorized needle valve and heat exchanger. The temperature of the heat exchanger is regulated by a feedback system, which can apply voltage to a heater and control the needle valve. By pumping on the sample space, the sample temperature can then maintained by flowing ^{4}He gas.

Finally, for the lowest temperature measurements, we have used an Oxford Kelvinox 300 ^{4}He/^{3}He dilution refrigerator (DR). This works as follows. A mixture of ^{3}He and ^{4}He is known to phase separate at low temperatures into a dilute and concentrated phase. In the limit of zero temperature, the dilute phase will still be approximately 6% ^{3}He. In a DR, the cooling power is obtained by pumping the ^{3}He

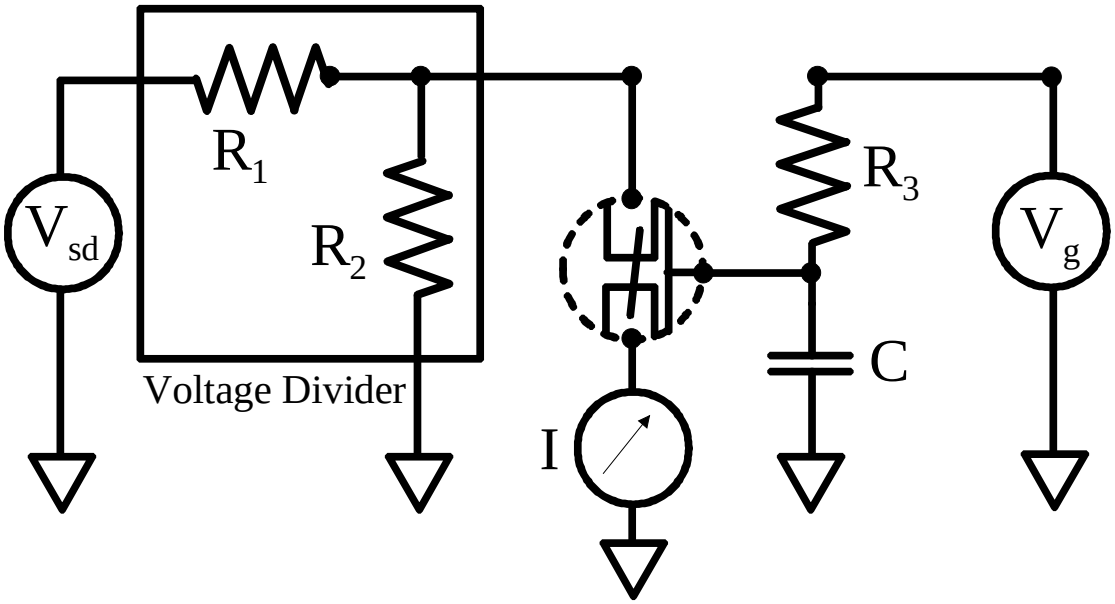

Figure 2-5: Typical measurement setup. The nanotube device is indicated schematically by the dashed circle. The device consists of a nanotube contacted by two leads a gate electrode. A source-drain voltage is applied through the voltage divider formed by R_1 and R_2. The gate voltage V_g is applied through the low-pass filter formed by the resistor R_3 and the capacitor C. R_3 is typically one the order of 100 MΩ, which serves to protect the device in case of a gate oxide breakdown or some other mishap. The current though the device is measured with the Ithaco current amplifier as shown.

from the dilute phase. To restore the equilibrium concentration, ^{3}He from the concentrated phase must migrate across the phase boundary into the dilute phase. Since the highest energy atoms leave preferentially, this cools the concentrated phase. The ^{3}He removed from the dilute phase can be recondensed and returned to the mixture, resulting in closed cycle refrigeration. The circulation rate can be increased significantly by heating the dilute phase, and because there is always ^{3}He present in the dilute phase the DR can continue to provide cooling power down to extremely low temperatures. In our lab, we typically reach a base temperature of ~50 mK.

2.3 Basic Observations

How these devices operate at room temperature depends on whether the nanotubes bridging the contacts are semiconducting[3] or metallic[1, 2]. The conductance of semiconducting nanotubes shows strong gate voltage dependence, while the conductance of metallic nanotubes does not. This behavior is shown in Figure 2-6, which shows the linear response conductance of a metallic and a semiconducting nanotube vs. the gate voltage. As can be seen, the conductance of the metallic tube is ~20 μS over the entire gate voltage range. In contrast, the semiconducting tube can be made insulating by applying a positive voltage to the gate (note the log scale for the conductance). This implies that the carriers are holes. This hole doping is believed to result from charge transfer due to work function differences between the nanotube and the gold leads[3]. A diagram depicting the band structure for

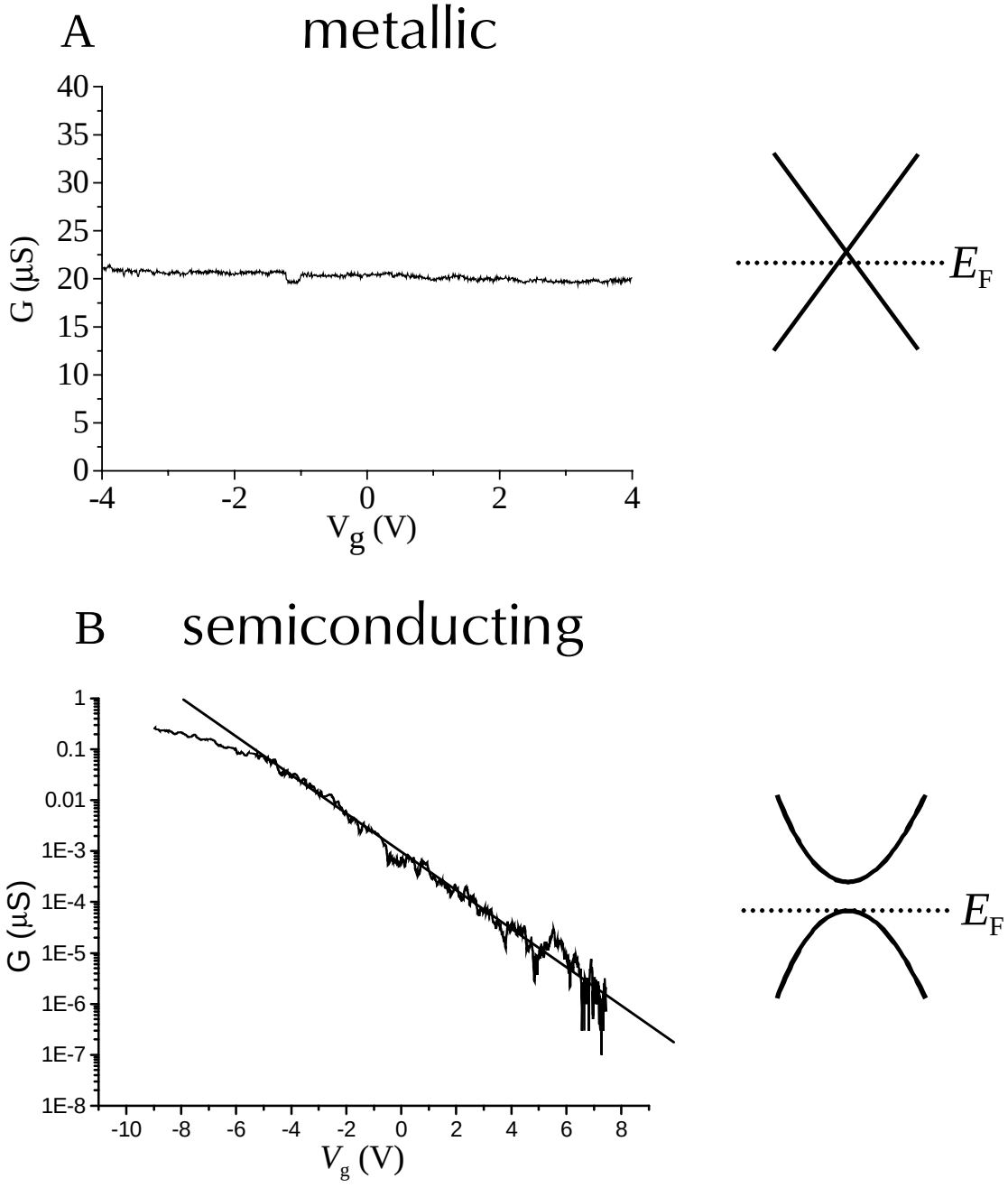

Figure 2-6: A) A metallic tube. The conductance shows very little dependence on gate voltage. B) A semiconducting tube. The conductance shows a strong gate voltage dependence.

both types of nanotube is shown to the right of the data. We have performed extensive low-temperature measurements on both types of nanotube, as will be discussed in detail in the following chapters.

References

1 S. J. Tans, et al., *Nature* **386**, 474 (1997).

2 M. Bockrath, et al., *Science* **275**, 1922 (1997).

3 S. J. Tans, R. M. Verschueren, C. Dekker, *Nature* **393**, 49 (1998).

Chapter 3

Single-Electron Transport in Ropes of Carbon Nanotubes

Marc Bockrath, David H. Cobden, Paul L. McEuen, Nasreen G. Chopra, and A. Zettl

Molecular Design Institute, Lawrence Berkeley National Laboratory and

Department of Physics, University of California at Berkeley, Berkeley, CA 94720, USA

Andreas Thess and R. E. Smalley

Center for Nanoscale Science and Technology, Rice Quantum Institute, and

Departments of Chemistry and Physics, Rice University MS-100, Rice University, P.O. Box 1892, Houston, TX 77251, USA.

Abstract

The electrical properties of individual bundles, or "ropes," of single-walled carbon nanotubes have been measured. Below ~10 Kelvin, the low bias conductance was suppressed for voltages below a few millivolts. In addition, dramatic peaks were observed in the conductance as a function of a gate voltage that modulated the number of electrons in the rope. These results are interpreted in terms of single electron charging and resonant tunneling through the quantized energy levels of the nanotubes comprising the rope.

In the past decade, transport measurements have emerged as a primary tool for exploring the properties of nanometer-scale structures. For example, studies of quantum dots have illustrated that single-electron charging and resonant tunneling through quantized energy levels regulate transport through small structures[1]. Recently, much attention has been focused on carbon nanotubes[2]. Their conducting properties are predicted to depend upon the diameter and helicity of the tube, parameterized by a rollup vector (n, m). One type of tube, the so-called (n, n), or armchair, tube, is expected to be a one-dimensional (1D) conductor with current carried by a pair of 1D subbands[3] whose dispersion relations near the Fermi energy E_F are indicated in the right inset to Fig. 3-1. A recent breakthrough has made it possible to obtain large quantities of the (10,10) single-walled nanotube (SWNT), which is ~1.4 nm in diameter[4]. This advance, in combination with recent successes in performing electrical measurements on individual multi-walled nanotubes (MWNTs)[5-8] and nanotube bundles[9], makes possible the study of the electrical properties of this novel 1D system.

We have measured transport through bundles, or ropes, of nanotubes bridging contacts separated by 200 to 500 nm. We find that a gap (suppressed conductance at low bias) is observed in the current-voltage (I-V) curves at low temperatures. Further, dramatic peaks are observed in the conductance as a function of a gate voltage V_g that modulates the charge per unit length of the tubes. These observations are consistent with single-electron transport through a segment of a single tube with a typical addition energy of ~ 10 meV and an average level spacing of ~ 3 meV.

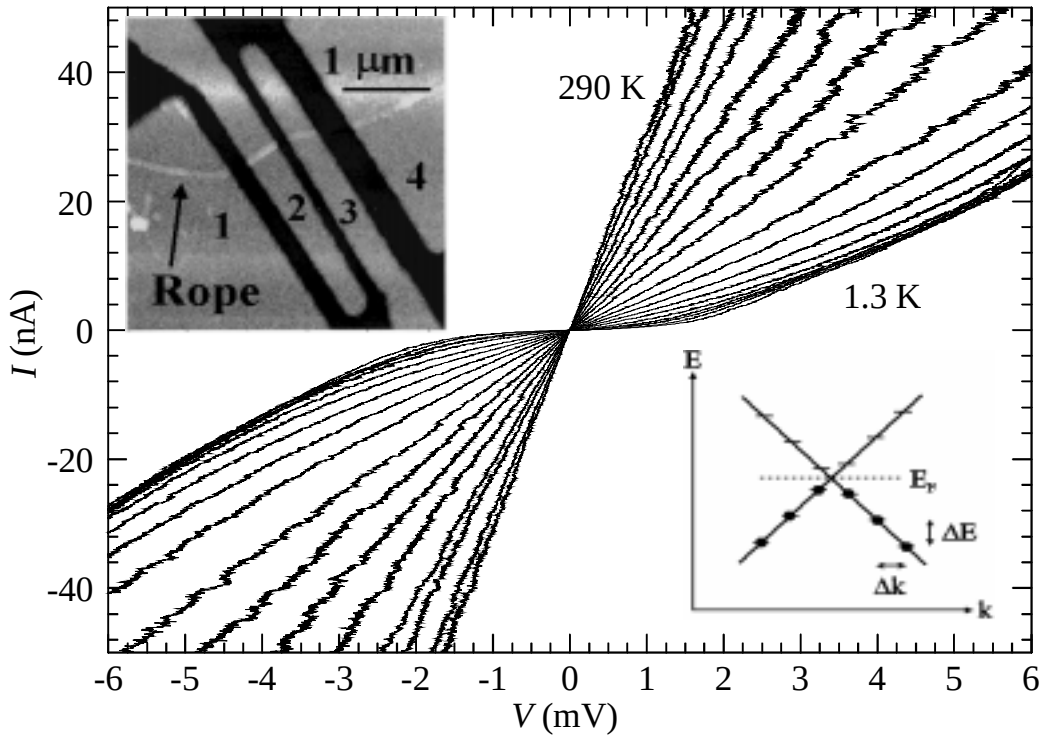

Figure 3-1: The *I-V* characteristics at a series of different temperatures for the rope segment between contacts 2 and 3. Left inset: an atomic force microscope (AFM) image of a completed device. The bright regions are the lithographically defined metallic contacts, labeled 1-4. The rope is clearly visible as a brighter stripe underneath the metallic contacts. In between the contacts (dark region) it is difficult to see the rope because of the image contrast. Note that the width of the rope in the AFM image reflects the convolution of its actual width with the AFM tip radius of curvature. The actual thickness of the rope is experimentally determined by the measuring its height with the AFM and assuming that the rope is cylindrical. Right inset: schematic energy-level diagram of the two 1D subbands near one of the two Dirac points [3], with the quantized energy levels indicated. The *k*-vector here points along the tube axis.

The device geometry (Fig. 3-1, left inset) consists of a single nanotube rope to which lithographically defined leads have been attached. The tubes are fabricated as described in[4] and consist of ropes made up of ~1.4-nm diameter SWNTs. Nanodiffraction studies[10] indicate that ~30 to 40% of these are (10,10) tubes**.** Contacts were made to individual ropes as follows. First, the nanotube material was ultrasonically dispersed in acetone and then dried onto an oxidized Si wafer on which alignment marks had previously been defined. An atomic force microscope (AFM) operating in the tapping mode was used to image the nanotubes. Once a suitable rope was found, its position was noted relative to the alignment marks. Resist was then spun over the sample, and electron beam lithography was used to define the lead geometry. A metal evaporation of 3 nm Cr then 50 nm of Au followed by liftoff formed the leads. This device has four contacts, and allows different segments of the rope to be measured and four-terminal measurements to be performed. The rope is clearly seen underneath the metal layer in the left inset to Fig. 3-1, although it is not visible in betweeen the contacts because of the contrast of the image. The device was mounted on a standard chip carrier, contacts were wire bonded, and the device was loaded into a ^{4}He cryostat. A dc bias could be applied to the chip carrier base to which the sample is attached. This gate voltage V_g modified the charge density along the length of the rope. Four samples were studied at liquid helium temperatures. All of the data presented here, however, were obtained from a single 12 nm diameter rope containing ~60 SWNTs.

Figure 3-1 shows the *I*-*V* characteristics of the nanotube rope section between contacts 2 and 3 as a function of *T*. The conductance is strongly suppressed near $V = 0$ for $T < 10$ K**.** Gaps of a similar magnitude were obtained for the other nanotube ropes with diameters varying from 7 to 12 nm and lengths from 200 to 500 nm. There was

no clear trend in the size of the gap or the high-bias conductance with the rope length or diameter. We note that measurements of MWNTs by ourselves and others[5,7,8] displayed no such gap in their *I-V* curves. These results are in rough agreement, however, with those reported previously by Fischer *et al.*[9] on similar, but longer, ropes of SWNTs. In their experiments, the linear-response conductance also decreased at low temperatures.

Figure 3-2A shows the linear response conductance G of the rope segment as a function of V_g at T = 1.3 K. Remarkably, the conductance consists of a series of sharp peaks separated by regions of very low conductance. The peak spacing varies significantly but is typically ~ 1.5 V. The peaks also vary widely in height, with the maximum amplitude of isolated peaks approaching e^2/h, where e is the electronic charge and h is Planck's constant. The peaks are reproducible, although sudden changes ("switching") in their positions sometimes occur, particularly at larger voltages. Figure 3-2B shows the temperature dependence of a selected peak. The peak width increases linearly with T (Fig. 3-2C) while the peak amplitude decreases. The most isolated peaks remain discernible even at T = 50 K. Figure 3-3 shows the differential conductance dI/dV as a function of both V and V_g for the rope segment between contacts 2 and 3. The data are plotted as an inverted gray scale, with dark corresponding to large dI/dV. The linear response conductance peaks (such as point A in the figure) correspond to the centers of the crosses along the horizontal line at $V = 0$**.** The gap in dI/dV corresponds to the white diamond shaped regions between the crosses (such as the region containing point B). These crosses delineate the point of the onset of conduction at finite V (point C). Because the application of large biases led to

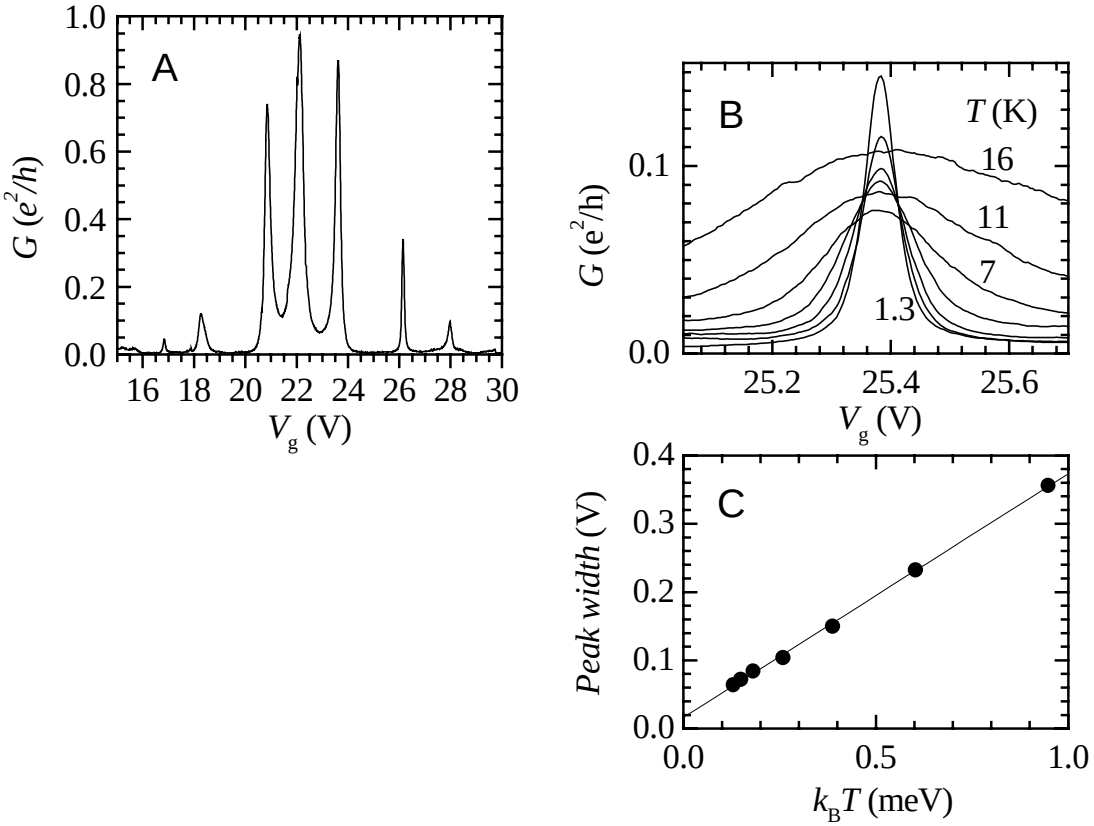

Figure 3-2: A) Conductance versus gate voltage at T =1.3 K for the rope segment between contacts 2 and 3. B) Temperature dependence of a peak. Note that this peak was measured on a different run from the data in A and does not directly correspond to any of the peaks there. C) Width of the peak in B as a function of T.

significant switching of the device, our sweeps were limited to ± 8 mV, and only the center of the diamond regions are visible. Additional features (point D) are also observed above the gap.

These results are reminiscent of previous measurements of Coulomb blockade (CB) transport in metal and semiconductor wires and dots[1]. In these systems, transport occurs by tunneling through an isolated segment of the conductor or dot that is defined by either lithographic patterning or disorder. Tunneling on or off this dot is governed by the single-electron addition and excitation energies for this small system. The period of the peaks in gate voltage, ΔV_g, is determined by the energy for adding an additional electron to the dot. In the simplest model that takes into account both Coulomb interactions and energy level quantization, which we refer to as the CB model, the peak spacing is given by

$$\Delta V_g = (U + \Delta E)/e\alpha \,, \qquad (1)$$

where $U = e^2/C$ is the Coulomb charging energy for adding an electron to the dot, ΔE is the single-particle level spacing, and $\alpha = C_g/C$ is the rate at which the voltage applied to the back gate changes the electrostatic potential of the dot. Here C is the total capacitance of the dot and C_g is the capacitance between the dot and the back gate.

To understand the dependence on V and V_g in more detail, consider the energy level diagrams in Fig. 3-4. They show a dot filled with N electrons, followed by a gap $U + \Delta E$ for adding the $(N+1)$th electron. Above this, additional levels separated by ΔE

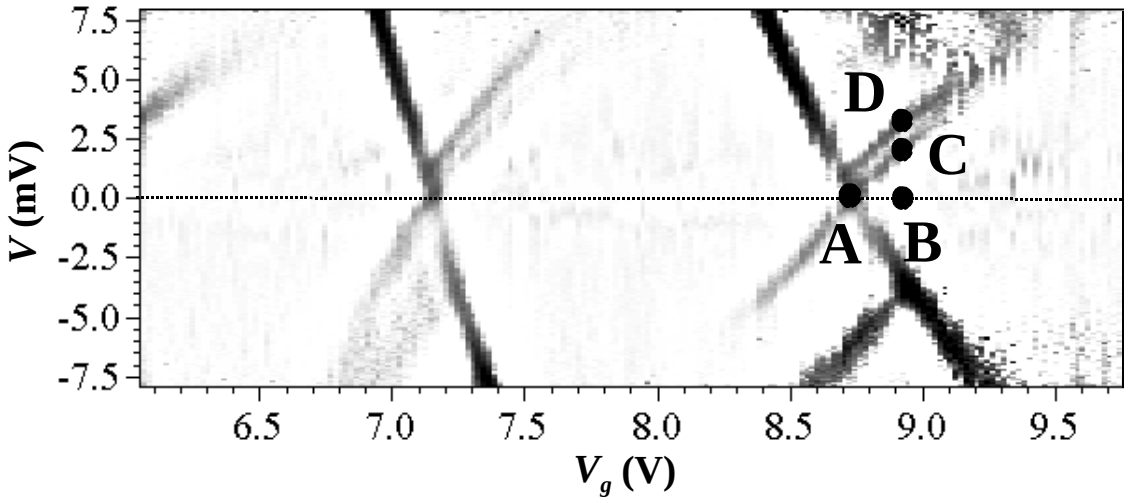

Figure 3-3: Gray scale plot of the differential conductance *dI/dV* of the rope segment between contacts 2 and 3, as a function of V and V_g. To enhance the image contrast a smoothed version of the data was subtracted from the differential conductance. The points marked A-D correspond to the diagrams in Fig. 4.

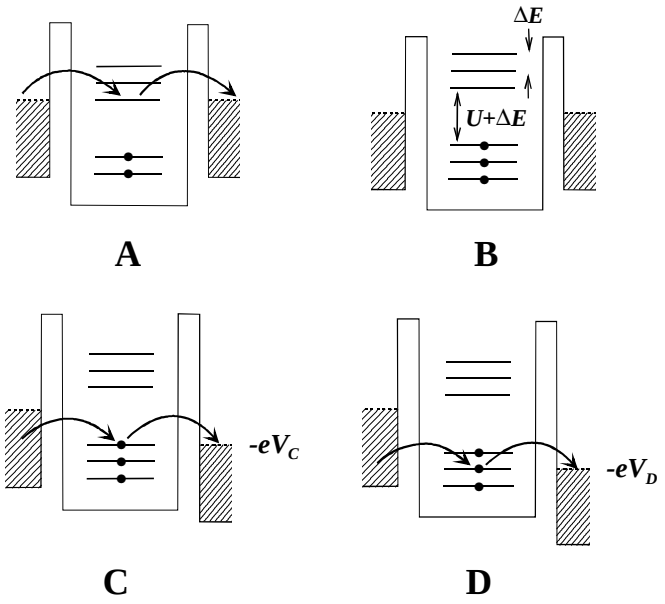

Figure 3-4: Schematic energy-level diagrams within the Coulomb blockade model corresponding to the points marked on Fig. 3: (A) at a Coulomb peak, where linear-response ($V = 0$) transport is possible; (B) between peaks, where linear-response transport is blockaded (the addition energy $U+\Delta E$ and the level spacing ΔE are indicated here); (C) and (D) at two different applied voltages, where transport occurs through the first and second occupied states respectively.

are shown, which correspond to adding the (*N+1*)th electron to one of the excited single-particle states of the dot. At a gate voltage corresponding to a CB peak, the energy of the lowest empty state aligns with the electrochemical potential in the leads and single electrons can tunnel on and off the dot at $V = 0$ (Fig. 3-4A). At gate voltages in between peaks (Fig. 3-4B), tunneling is suppressed because of the single electron charging energy U. However, if V is increased so that the electrochemical potential of the right lead is pulled below the energy of the highest filled state, an electron can tunnel off the dot, resulting in a peak in dI/dV (Fig. 3-4C). Further increasing V allows tunneling out of additional states, giving additional peaks in dI/dV (Fig. 3-4D). Similar processes occur for negative bias, corresponding to tunneling through unoccupied states above the Coulomb gap. At its largest, the required threshold voltage for the onset of conduction of either type is

$$V_{\max} = U + \Delta E \, . \qquad (2)$$

To apply this model to our system, we must postulate that transport along the rope is dominated by single electron charging of a small region of the rope, or perhaps a single tube within the rope (see below). For now, we will use the CB model to infer the properties of this isolated region. We initially restrict ourselves to the data of Figs. 3-2 and 3-3, which corresponds to the rope segment between the two central contacts.

In the CB model the temperature dependence can be used to deduce the parameters in Eq. 1. The width of a CB peak is given by $d(\Delta V_g)/dT = 3.5\, k_B/\alpha e$, where k_B is Boltzmann's constant. Comparison with the data in Fig 3-2C gives $\alpha = 0.01$. From this, and the measured spacing between peaks of 1 to 2 V, we obtain a typical

addition energy: $U + \Delta E$ = 10 to 20 meV. Also note that the disappearance of the oscillations above ~50 K yields a similar estimate for the addition energy.

The amplitude of the conductance peak increases with decreasing temperature at low temperatures. Within the extended CB model, this result indicates that $\Delta E >> k_B T$ and that transport through the dot occurs by resonant tunneling though a single quantum level. The peak height decreases as T is increased up to ~10 K. This sets a lower bound on the energy level splitting of $\Delta E \sim 1$ meV. In addition for some peaks, such as those in the center of Fig. 3-2A, the intrinsic linewidths of the peaks are clearly observable. Fitting the peak shapes (not shown) reveals that they are approximately Lorentzian, as expected for resonant tunneling through a single quantum level.[1]

The nonlinear *I-V* measurements confirm the addition and excitation energies deduced above. The maximum size of the Coulomb gap V_{max} in Fig. 3-3 is a direct measure of the addition energy - for the two peaks in the figure, it is ~ 14 meV . Tunneling through excited states was also visible above the Coulomb gap for some peaks, and the level spacing to the first excited state ranged from 1 to 5 meV[11]. For example, in Fig. 3-4 the level spacing between states labeled by C and D is ΔE = 1 meV.

These parameters compare well with expectations. Consider a single (*n*, *n*) nanotube. The tube is predicted to be metallic[3], with two 1D subbands occupied at E_F. The order of magnitude of the average level spacing should be related to the dispersion *dE/dk* at the Fermi level:[3,12]

$$\Delta E \sim (dE/dk)\Delta k/2 \sim (dE/dk)(\pi/L) \sim 0.5\ eV / L[\text{nm}]\ , \qquad (3)$$

where the 2 arises from non-degeneracy of the two 1D subbands (see Fig. 3-1, right inset.) The charging energy is more difficult to estimate accurately. The actual capacitance of the dot depends on the presence of the leads, the dielectric constant of the substrate, and the detailed dielectric response of the rope[13]. For an order of magnitude estimate, however, we take the capacitance to be given by the size of the object, $C = L$. We then have:

$$U = \frac{e^2}{C} = \frac{e^2}{L} \approx \frac{1.4\,eV}{L[nm]}. \qquad (4)$$

Note the remarkable result that in 1D, both ΔE and U (Eqs. 3 and 4) scale as $1/L$, and hence the ratio of the charging energy to the level spacing is roughly independent of length. This means that the level spacing will be important even in fairly large dots, unlike in 3D systems. For a length of tube $L \sim 200$ nm (the spacing between the leads) we obtain $U = 7$ meV and $\Delta E = 2.5$ meV, consistent with the observed values.

To relate these theoretical results for a single tube to the measurements of rope samples, we first note that current in the rope is likely to flow along a filamentary pathway[14] consisting of a limited number of single tubes or few-tube segments. This is because, first, 60 to 70 % of the tubes are not (10,10), and hence the majority of the tubes in the rope will be insulating at low T[15]. Second, the intertube conductance is small compared to the conductance along the tube, inhibiting intertube transport. Finally, the metal probably only makes contact to those metallic tubes which are on the surface of the rope, further limiting the number of tubes involved in transport.

Disorder along a filamentary pathway will tend to break it up into weakly coupled localized regions. This disorder may result from defects[17], twists[18], or places where intertube hopping is necessary along the pathway. Generally, the conductance should then determined by single electron charging and tunneling between a few such localized regions. For other rope segments that we have measured, the characteristics were consistent with transport through a few segments in series or parallel, each with different charging energies. For the particular rope segment we have focused on here, however, a single well defined set of CB peaks was observed, indicating that transport was dominated by a single localized region. We believe this region is a section of a single tube, or at most a few-tube bundle. The measured charging energies and level spacing indicate that the size of this region is roughly the length between the contacts.

Each peak therefore corresponds to resonant tunneling though a coherent molecular state that extends for up to hundreds of nanometers in a localized region within the nanotube bundle. Furthermore, the amplitudes of some isolated peaks approach the theoretical maximum for single-electron transport of e^2/h. This is only possible if the barriers which confine this state at either end are approximately equal, and there is no other significant resistance in series with the localized region. This is consistent with the barriers being at the contacts between the metal leads and the rope. It is also possible that the barriers are within the rope, in which case the metal-rope contacts must be almost ideal so as not to reduce the maximum conductance from e^2/h[16]. Variation in the coupling to each lead from level to level can account for the varying peak sizes apparent in Fig. 3-2.

Although the above interpretation accounts for the major features in the data, many interesting aspects of this system remain to be explored. First, one would like to establish absolutely that transport is indeed occurring predominantly along a single tube. Second, it should be determined whether all details of the data can be explained within the simple CB model discussed above, since Coulomb interactions may significantly modify the low-energy states from simple 1D non-interacting levels[19]. Of great interest would be measurements of disorder-free tubes, where the intrinsic conducting properties of the tube can be measured without the complications of single-electron charging. To address these issues, experiments on individual single-walled tubes are highly desirable, and progress is being made in this direction[20]. Yet another important experiment would be to measure directly the intertube coupling by making separate electrical contact to two adjacent tubes.

References

A similar version of Chapter 3 appeared in Science **275** 1922 (1997).

1 For a review, see *Single Charge Tunneling*, edited by H. Grabert and M.H. Devoret (Plenum Press, NY, 1991); M. Kastner, Physics Today, **46**, 24 (1993); Leo P. Kouwenhoven and P.L. McEuen, *Nanoscience and Technology*, G. Timp, ed. (AIP Press, NY), to be published.

2 S. Iijima, Nature **354**, 56 (1991); for a recent review, see T. Ebbesen, Physics Today, **49**, 26 (1996).

3 R. Saito, M. Fujita, G. Dresselhaus, and M.S. Dresselhaus, Appl. Phys. Lett. **60**, 2204 (1992); N. Hamada, S. Sawada, and A. Oshiyama, Phys. Rev. Lett. **68**, 1579 (1992).

4 A. Thess *et al*., Science **273**, 483 (1996).

5 L. Langer *et al.*, Phys. Rev. Lett. **76**, 479, (1996).

6 H. Dai, E.W. Wong, and C.M. Lieber, Science **272**, 523 (1996).

7 T.W. Ebbesen *et al.*, Nature 382, **54** (1996).

8 A. Yu. Kasumov, I.I. Khodos, P.M. Ajayan, and C. Colliex, Europhys. Lett. **34**, 429 (1996).

9 J. E. Fischer *et al*, Phys. Rev. B. **55**, 4921 (1997).

10 D. Bernaerts, A. Zettl, N. G. Chopra, A. Thess, R. E. Smalley, *Solid State Communications* **105**, 145-9 (1998); J. M. Cowley, P. Nikolaev, A. Thess, and R. E. Smalley, Chem. Phys. Lett. **265**, 379 (1997).

11 The level spacing can be determined from the data in Fig. 3-3 by two means. The first means is to measure the separation between features in V_g, and employ the

conversion factor $\alpha = V_{max}/\Delta V_g$. The second is to measure the separation between the features in V, and use the slopes of the lines defining the Coulomb gap to infer $\alpha_L = C_L/C$ and $\alpha_R = C_R/C$. For more information, see Ref [1].

12 H.-Y. Zhu, D. J. Klein, T. G. Schmalz, N. H. Rubio, and N. H. March, preprint (1997).

13 L. X. Benedict, S. G. Louie, and M. L. Cohen, Phys. Rev. B, **52**, 8541 (1995).

14 Other measurements on these samples also support the notion that transport is through individual decoupled tubes. In four terminal measurements of the ropes at temperatures > 30 K (where the rope resistance becomes much less than the voltage probe impedance and reliable four-terminal measurements are possible), non-local voltages have been observed. For example, referring to the AFM image shown in Fig. 3-1, a voltage can appear between the terminals 1 and 2 in response to a current flowing between contacts 3 and 4. Such non-local effects are possible if different contacts make contact to different tubes and the intertube coupling is small. Current injected into 4 in a particular tube that is not well connected to 3 can arrive at contact 1 or 2, producing a non-local response.

15 Individual tubes within a rope have chiral angles within 10^o of the achiral (10,10) tube with roughly 30 to 40% of the sample being (10,10) tubes [10]. The indices of tubes consistent with the experimental constraints on chirality and radius [4] are (10,10), (9,11), (8,12), (7,13) and the opposite-handed twins. The gap of the (7,13) tube is small and likely does not survive intertube interactions, but the gaps of the (9,11) and (8,12) tubes are about 0.5 eV, which is probably large enough to maintain semiconducting behavior within the rope.

16 The large peak heights, combined with the fact that the room temperature conductance of the center segment is also approximately e^2/h, imply that good electrical contact has been made between the metal leads and part of the rope.

17 L. Chico, L. X. Benedict, S. G. Louie, and M. L. Cohen, Phys. Rev. B **54,** 2600 (1996); L. Chico *et al*. Phys. Rev. Lett. **76**, 971 (1996).

18 C.L. Kane and E.J. Mele, to be published in Physical Review Letters.

19 Y. A. Krotov, D.-H. Lee, S. G. Louie, Phys. Rev. Lett. **78**, 4245 (1997); C. Kane, L. Balents, M. P. A. Fisher, Phys. Rev. Lett. **79**, 5086 (1997).

20 S. Tans, *et al.*, Nature **386**, 474 (1997).

21 We would like to acknowledge useful discussions with V. Crespi, M. Cohen, D.H. Lee, and S. Louie. We are also indebted to S. Tans for communicating his unpublished results on measurements on nanotubes and emphasizing the importance of a gate voltage. Supported by the U.S. Department of Energy under Contract No. DE-AC03-76SF00098 and by the Office of Naval Research, Order No. N00014-95-F-0099.

Chapter 4

Spin Splitting and Even-Odd Effects in Carbon Nanotubes

David H. Cobden, Marc Bockrath, and Paul L. McEuen

Department of Physics, University of California and Materials Science Division, Lawrence Berkeley National Laboratory, Berkeley, California, 94720

Andrew G. Rinzler and Richard E. Smalley

Center for Nanoscale Science and Technology, Rice Quantum Institute, and Department of Chemistry and Physics, MS-100, Rice University, P.O. Box 1892, Houston, TX 77251

Abstract

The level spectrum of a single-walled carbon nanotube rope, studied by transport spectroscopy, shows Zeeman splitting in a magnetic field parallel to the tube axis. The pattern of splittings implies that the spin of the ground state alternates by ½ as consecutive electrons are added. Other aspects of the Coulomb blockade characteristics, including the current-voltage traces and peak heights, also show corresponding even-odd effects.

The spin state of small multi-electron systems is an important testing ground for our understanding of interacting quantum systems. For N non-interacting electrons in non-degenerate levels with spin, the single-particle states are occupied in order of energy, leading to a total spin $S = 0$ for even N and $S = 1/2$ for odd N. Coulomb interactions among the electrons can alter this behavior, however. In atoms, for example, the exchange interaction among electrons in a shell leads to Hund's rule and a spin-polarized ground state for a partially filled shell. Recently, attention has been focused on similar questions in quantum dots. In small 3D metallic dots, Zeeman splitting consistent with an alternation between $S = 0$ and 1/2 was found [1]. This may be understood within the constant interaction (CI) model [2], where the energy for adding an electron is the non-interacting level spacing ΔE plus a constant charging energy U. On the other hand, in two-dimensional dots evidence for spin polarization in the ground state has been found in recent experiments on both high symmetry [3] and low symmetry dots [4], requiring explanations beyond the CI model.

Of considerable interest is the situation in 1D, where Coulomb interactions are predicted to profoundly influence the properties of the system [5]. Here exact theoretical results are available for many model systems. For instance, for electrons in a box in strictly one dimension (1D), Lieb and Mattis [6] proved that in spite of interactions the ground state has the lowest possible spin. In real systems, however, a variety of factors, such as finite transverse dimensions, multiple 1D subbands, and spin-orbit coupling, may lead to a spin-polarized ground state.

Here we present measurements of the spin state of single-walled carbon nanotubes, a novel quasi-1D conductor where the current is carried by two 1D subbands

[7]. It has recently been shown experimentally [8,9] that when contacts are attached, these nanotubes behave as quasi-1D quantum dots. Here we concentrate on a very short (~200 nm) nanotube dot with a correspondingly large level spacing. To study the spin state, we apply a magnetic field along the axis of the nanotube and examine the Zeeman effects in the transport spectrum. From the pattern of the spin splitting, we conclude that as successive electrons are added the ground state spin oscillates between S_0 and S_0+1/2, where S_0 is most likely zero. This results in an even/odd nature of the Coulomb peaks which is also manifested in the asymmetry of the current-voltage characteristics and the peak height. It may also be reflected in the excited state spectrum.

The devices are made [9] by depositing single-walled nanotubes [10] from a suspension in dichloroethane onto 1-μm thick SiO_2. The degenerately doped silicon substrate is used as a gate electrode. A single rope is located relative to prefabricated gold alignment marks using an atomic force microscope (AFM). Chromium-gold contacts are then deposited on top using 20 keV electron beam lithography. An AFM image of a 5-nm diameter rope (consisting of about a dozen tubes) with six contacts is shown in the inset to Fig. 4-1. Leads labeled s (source), d (drain) and V_g (gate) are drawn in to indicate the typical measurement configuration.

Figure 4-1 shows the linear-response two-terminal conductance, G, versus gate voltage, V_g, at magnetic field $B = 0$ and temperature $T = 100$ mK. It exhibits a series of sharp Coulomb blockade oscillations [8,9,2] that occur each time an electron is added to the nanotube dot. For $T <\sim 10$ K all the peaks have the same width, proportional to T [9], and a T-independent area, indicating that the level spacing ΔE is $>> k_B T$ and that

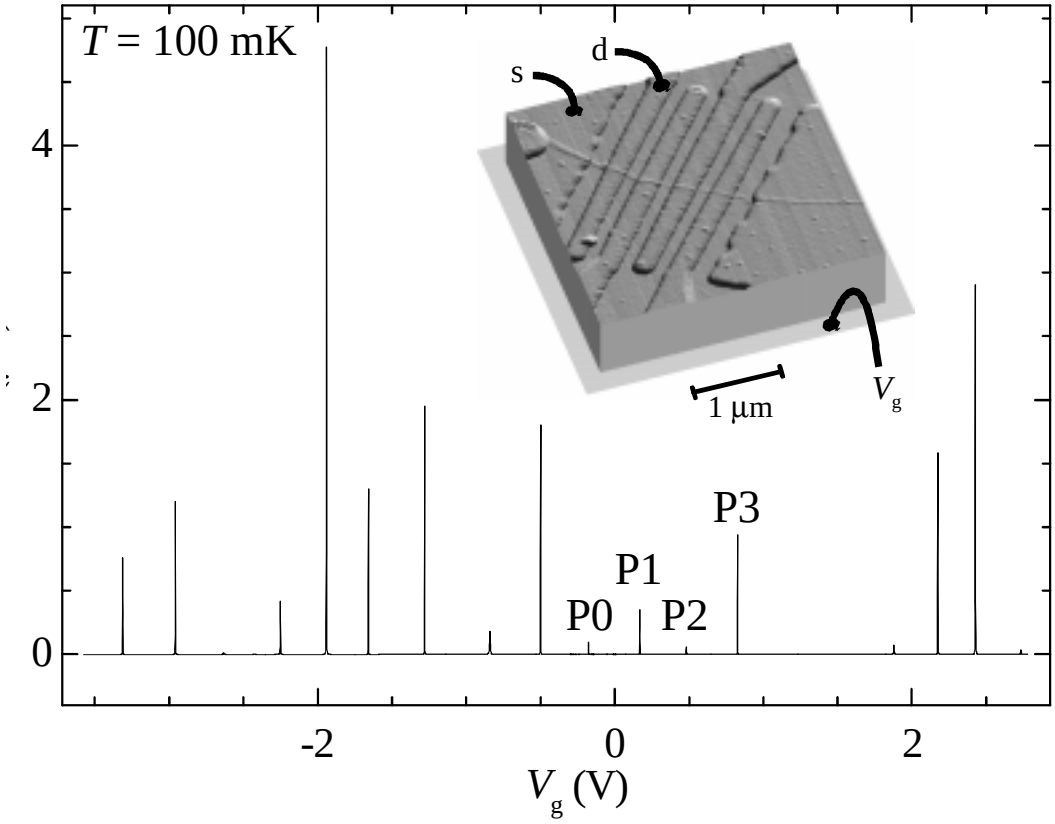

Figure 4-1: A) Conductance G of a nanotube rope vs gate voltage V_g. Inset: AFM image of a device with schematic wires added.

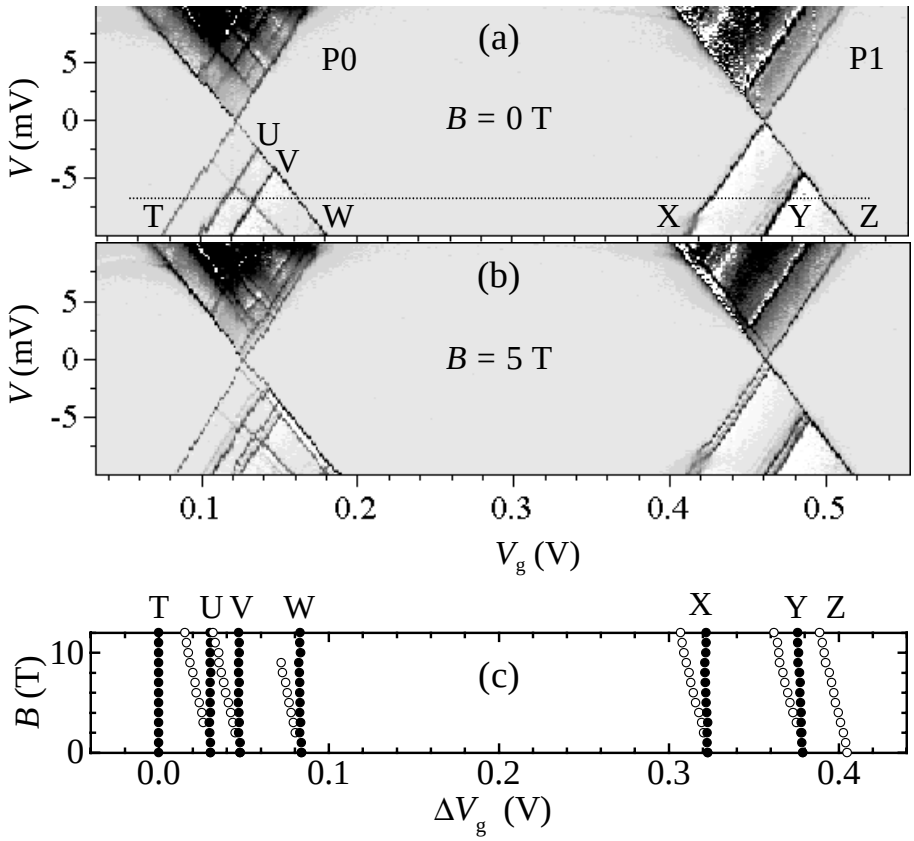

Figure 4-2: A) Greyscale plot of the differential conductance dI/dV of Coulomb peaks P0 and P1 at B = 0 (darker = more positive dI/dV.) B) Same as A but at B = 5 T. C) B-dependence of the relative positions of the peak in dI/dV labeled T-Z in A, at a bias of V = -7 mV as indicated by the dashed line in A. On the x-axis we plot $\Delta V_g = V_g - V_g^T$, where V_g^T is the position of peak T, to remove unreproducible temporal drift of the characteristics along the V_g - axis.

transport is through a single quantum level. We deduce that the dot electrostatic potential V_{dot} is linearly related to V_g, with a coefficient $\alpha \equiv dV_{dot}/dV_g = 0.09$.

Figure 4-2A is a greyscale plot of the differential conductance dI/dV as a function of V and V_g at $B = 0$. Dark lines here are loci of peaks in dI/dV. Crosses P0 and P1 are formed by the identically labeled Coulomb peaks in Fig. 4-1. The interpretation of such a plot in the CI model is well known [3]. Each line is produced by the alignment of a quantized energy level in the dot with the Fermi level in a contact. From the spacing of the lines we infer a typical level spacing $\Delta E \sim 5$ meV, and from the average Coulomb peak spacing we obtain a charging energy $U \sim 25$ meV. These values are consistent with expectations based on previous measurements [8,9] for a 100-200 nm length of tube. Thus we find as before [9] that the portion of nanotube rope forming the dot appears roughly equal in length to the distance between the contacts (nominally 200 nm.)

Figure 4-2B shows the results of the same measurement at $B = 5$ T. Most of the lines observed at $B = 0$ have split into parallel pairs. The splitting is linearly proportional to B. This can be seen in Fig. 4-2 C, where the relative positions of the peaks in dI/dV at $V = -7$ mV (dotted line in Fig. 4-2A) are plotted as a function of B. One group of peaks (denoted by open symbols) moves downwards in V_g relative to the other (solid symbols) by an amount proportional to B. Note that not all the lines at $B = 0$ split. Over a series of ten consecutive crosses in the range $-2\text{ V} < V_g < +1\text{ V}$ [11], the following pattern emerges: on alternate peaks, (P0, P2, etc.,) the leftmost lines in the cross (such as T) do not split, while on the other peaks, (P1, P3, etc.,) the rightmost lines (such as Z) do not split.

These measurements can be used to obtain information about the ground-state spin S_N of the dot with N electrons, as we now discuss. The analysis is based on the following spin selection rules: since the tunneling electron carries spin 1/2, both the total spin, S, and its component along the magnetic field axis, S_z,, must change by ±1/2 for observable transitions [12].

The energy required for a tunneling process is the energy difference between the N- and (N+1)-electron states. In the absence of orbital effects [13], this depends on B only through the Zeeman term $-g\mu_B B\Delta S_z$, where g is the electronic g-factor, ΔS_z is the change in S_z and μ_B is the Bohr magneton. In Fig. 4-2C we therefore associate the open-symbol transitions with $\Delta S_z = +1/2$ and the closed-symbol transitions with $\Delta S_z = -1/2$. Fitting their separation to $g\mu_B B/\alpha$ yields $g = 2.04 \pm 0.05$, which is consistent with $g = 2.0$ for graphite and with the value $g = 1.9 \pm 0.2$ obtained previously for a single excited state in a nanotube [8].

From the pattern of splittings of the lowest-energy transitions (the edges of the crosses in Fig. 4-2A) one can deduce the change in ground-state spin, $\Delta S = S_{N+1}-S_N = \pm 1/2$, across each Coulomb peak. The reason is as follows [1]. First consider an electron tunneling into the N-electron ground state in a magnetic field, where initially the total spin is aligned with the field, so that $S_z = -S_N$. For the case $\Delta S = +1/2$, after tunneling S_z may be either $-S_N-1/2$ or $-S_N+1/2$. The corresponding line therefore splits with B. However, for the case $\Delta S = -1/2$, only $S_z = -S+1/2$ is possible for the final state, because of the requirement $|S_z| \leq S_{N+1} = S-1/2$. The corresponding line therefore does not split with B. A similar argument for an electron tunneling out of the N+1 ground state shows that if $\Delta S = -1/2$ the line splits, while if $\Delta S = +1/2$ it does not. To

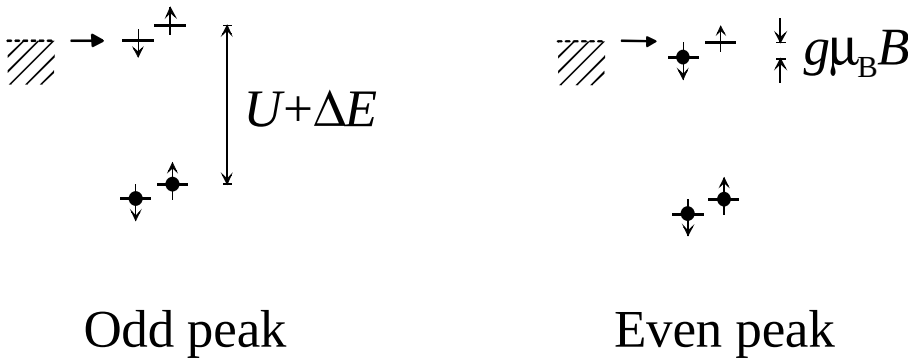

Figure 4-3: Explanation of splitting pattern within the CB model. The lowest-energy transition splits for an odd peak (left), where *N* changes from even to odd, but not for an even peak (right), where *N* changes from odd to even.

summarize: if $\Delta S = +1/2$ for a Coulomb peak, the lines on the right edge of the cross do not split, while if $\Delta S = -1/2$ the lines on the left edge do not split.

This general result is also predicted by the CI model, as indicated in Fig. 4-3. If N is even, $S_N = 0$, and the next electron can be added to either spin-up or spin-down state of the next orbital level (left sketch), resulting in $S_{N+1} = 1/2$. On the other hand, if N is odd, $S_N = 1/2$ and the next electron can only be added to the one empty spin state of that level (right sketch), resulting in $S_{N+1} = 0$. A corresponding story can be told for removing an electron. The predicted pattern of splittings is the same as in the previous paragraph, but with the additional implication that N is even if $\Delta S = +1/2$ and odd if $\Delta S = -1/2$.

Comparing the above predictions with Fig. 4-2, we find that $\Delta S = +1/2$ for peak P0 and $\Delta S = -1/2$ for peak P1. Since the pattern of splitting alternates between the two types over ten Coulomb peaks, we deduce that S_N oscillates between some value S_0 and $S_0+1/2$ as ten successive electrons are added. We cannot rule out the possibility that S_0 is finite. However, since polarization of a system is usually related to states near the Fermi level, and in this system we see the spin alternating as these states are filled, it is most likely that that $S_0 = 0$, as in the CI model. If this is the case, the behavior is consistent with the prediction of Ref. [6] for 1D electrons: the ground state spin alternates between 0 and 1/2. This is our principal result. We subsequently describe Coulomb peaks where N changes from odd to even (P0, P2, etc.) as *even* peaks, because the added electron is even. Peaks P1, P3, etc. we call *odd* peaks, because the added electron is odd. This is indicated in Fig. 4-3.

The alternating spin of the ground state should also be reflected in the *I*-*V* characteristics at zero magnetic field, if the source and drain contacts have different tunnel resistances. If, for instance, the source contact dominates the resistance, the magnitude of the current I_- at negative source bias V is determined by transitions from the N to the N+1 electron ground state, as long as the bias is less than the level spacing. On the other hand, the current I_+ at positive V is determined by transitions from the N+1 to the N electron ground state. The ratio $\beta = I_+/I_-$ therefore reflects the differences caused by the spin selection rules in these two situations. This can easily be understood in the CI model, as illustrated for an even peak (ΔS = -1/2) in Fig. 4-4A. For negative V (left sketch) an electron tunneling in from the source can only go into one available spin state. On the other hand, for positive V (right sketch), either of two electrons can tunnel out. The current is therefore larger for positive V. An elementary calculation gives $\beta = (2G_s+G_d)/(G_s+2G_d)$, where G_s and G_d are the source and drain barrier conductances respectively. For $G_s < G_d$, this predicts $1 < \beta < 2$. In contrast, for an odd peak (ΔS = +1/2), the inverse ratio is found, and $1/2 < \beta < 1$ is predicted.

The solid line in fig. 4-4B is the *I*-*V* characteristic measured at the center of peak P0. Near $V = 0$, the *I*-*V* is ohmic, but for $|V| >\sim 0.5$ mV the current saturates into a slowly varying form. The saturation current is larger for positive than for negative V. Moreover, if the same data is plotted (dashed line) with the current scaled by a factor $-\beta$, where $\beta = 1.57$, the *I*-*V*'s in the two bias directions can be brought onto the same interpolated curve (dotted line.) For each peak an appropriate value of β can be chosen to achieve a similar matching. The results are plotted in the top panel of Fig. 4-4C. We find that $1 < \beta < 2$ for P0 and P2, while $1/2 < \beta < 1$ for P1 and P3. Comparing these

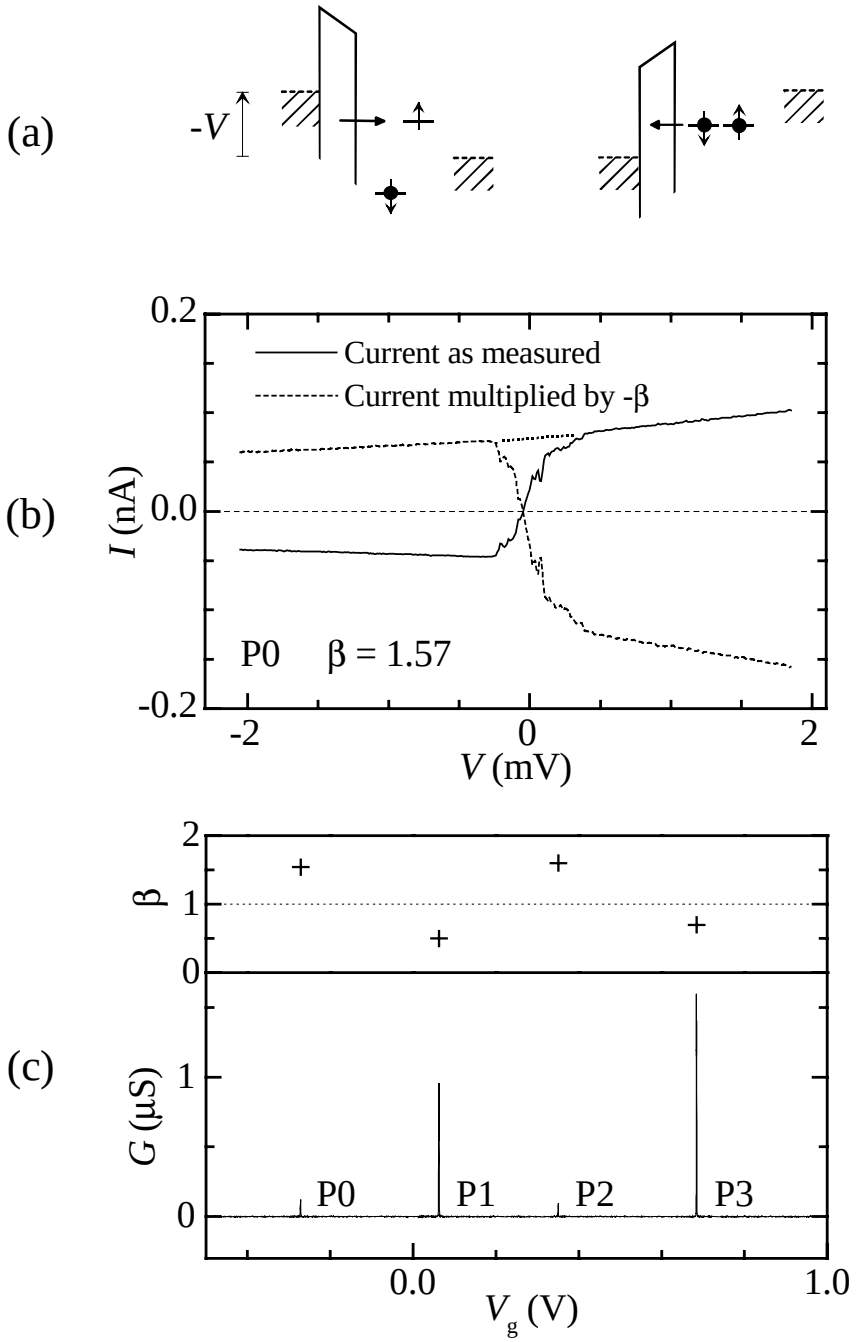

Figure 4-4: A) Current flow at high bias in the CI model. Only the larger barrier, between source and dot, is drawn. B) Solid line: I-V measured at the center of peak P0 in Figure 4-1. Dashed line: the same trace with I multiplied by $-\beta = -1.57$. Dotted line: interpolation between these. C) Lower: expanded view of the peaks P0 - P3. Upper: measured values of β for these peaks. The oscillating value of β implies that successive electrons are added with opposite spin directions (see text).

values with the predictions for $\beta = I_+/I_-$ in the previous paragraph, we see that they are perfectly consistent with our assignments of $\Delta S = +1/2$ or -1/2 from the Zeeman splitting [14].

We have seen from the Zeeman splitting and the *I-V* characteristics that the ground state spin behaves as is predicted by the CI model. However, this implies not that effects such as exchange are small, but only that they do not change the spin of the *N*-electron ground state of the system. Exchange might for instance be manifested in the excited state spectra, where one would anticipate a difference between even and odd peaks. For odd peaks, the added electron simply goes into higher unoccupied orbital levels, giving rise to a single-particle spectrum. For even peaks, however, the added electron can form singlet and triplet states with the original unpaired electron, leading to exchange splitting. A singlet-triplet splitting has indeed been seen in the excitation spectra of semiconductor dots [15]. We observe indications of this predicted behavior in peaks P0-P3. The lowest excited states visible at negative *V* on even peaks in each case form a pair (such as lines U and V on peak P0 in Fig. 4-2A), while those on odd peaks do not (such as line Y on P1). This will be investigated further in future work.

A contradiction with the CI model is also seen in the peak heights. These are predicted to be identical for a pair of peaks arising from a single orbital level [16]. However, we find that the odd peaks tend to be considerably larger than the even peaks, as apparent in Fig. 4-4C. This behavior is not understood and deserves further investigation.

In summary, our transport measurements of a short nanotube quantum dot show that the ground state of this 1D electronic system alternates between $S = 0$ and $S = 1/2$. A variety of even-odd effects are seen in the addition spectrum, some of which, such as an alternation of the peak heights, require explanations beyond the simple Coulomb blockade picture.

We thank Marvin Cohen, Cees Dekker, Noah Kubow, Dung-Hai Lee, Steven Louie, Jia Lu, Boris Muzykantskii, and Sander Tans for helpful discussions. The work at LBNL was supported by the Office of Naval Research, Order No. N00014-95-F-0099 through the U.S. Department of Energy under Contract No. DE-AC03-76SF00098, and by the Packard Foundation. The work at Rice was funded in part by the National Science Foundation and the Robert A. Welch Foundation

.

References

A similar version of Chapter 4 appeared in Phys. Rev. Lett. **81** 681 (1998).

1 D. C. Ralph, C. T. Black, and M. Tinkham, Phys. Rev. Lett. **74**, 3241 (1995); Phys. Rev. Lett. **78**, 4087 (1997).

2 L. P. Kouwenhoven *et al.*, in *Mesoscopic Electron Transport*, Eds. L. P. Kouwenhoven, G. Schon and L. L. Sohn (Kluwer, 1997).

3 S. Tarucha *et al.*, Phys. Rev. Lett. **77**, 3613 (1996).

4 D. R. Stewart *et al.*, Science **278**, 1784 (1998).

5 See, e.g., *The Many-Body Problem*, Ed. D. C. Mattis (World Scientific, Singapore, 1993).

6 E. Lieb and D. Mattis, Phys. Rev. **125**, 164 (1962).

7 N. Hamada, S. Sawada, and A. Oshiyama, Phys. Rev. Lett. **68**, 1579 (1992); R. Saito *et al.*, Appl. Phys. Lett. **60**, 2204 (1992).

8 S. J. Tans *et al.*, Nature **386**, 474 (1997).

9 M. Bockrath *et al.*, Science **275**, 1922 (1997).

10 A. Thess *et al.*, Science **273**, 483 (1996).

11 Outside this range of V_g the characteristics are complicated by charging of another dot (probably another section of nanotube.)

12 D. Weinmann, W. Hausler, and B. Kramer, Phys. Rev. Lett. **74**, 984 (1995).

13 The only expected orbital effect of an axial magnetic field results from the Aharonov-Bohm phase due to the flux ϕ through the tube [17], which may shift the levels by up to ~ 2.5 meV at 12 T. In our data the non-Zeeman energy shifts of the transitions at this field are less than 100 μeV. This can be accounted for if all levels are

shifted equally, as expected if the Fermi level is displaced away from the band-crossing points by, for example, charge transfer from the metal contacts [18].

14 From a detailed study of the *I-V*'s in this range of V_g we can deduce that $G_s < G_d$. The gradual increase of $|I|$ as V becomes more positive in Figure 4-4B is explained by electric-field lowering of the dominating source barrier, as indicated in Figure 4-4A.

15 L. P. Kouwenhoven *et al.*, Science **278**, 1788 (1997).

16 C. W. J. Beenakker, Phys. Rev. B **44**, 1646 (1991).

Chapter 5

Chemical Doping of Individual Semiconducting Carbon Nanotube Ropes

Marc Bockrath, J. Hone, A. Zettl, and Paul L. McEuen

Department of Physics, University of California and Materials Science Division, Lawrence Berkeley National Laboratory, Berkeley, California, 94720

Andrew G. Rinzler and Richard E. Smalley

Center for Nanoscale Science and Technology, Rice Quantum Institute, and Department of Chemistry and Physics, MS-100, Rice University, P.O. Box 1892, Houston, TX 77251

(April 2, 1999)

Abstract

We report the effects of potassium doping on the conductance of individual semiconducting single walled carbon nanotube ropes. We are able to control the level of doping by reversibly intercalating and de-intercalating potassium. After doping, the carriers are electrons. Typical values for the doping level are found to be ~ 100-1000 electrons/μm. The effective mobility for the electrons is μ_{eff} ~ 20-60 $cm^2\ V^{-1}\ s^{-1}$, a value similar to that reported for the hole effective mobility in nanotubes[1].

Recently, much attention has been focused on the transport properties of ~1-2 nm diameter single-walled carbon nanotubes (SWNTs). The band structure of a given SWNT depends on its chirality and is either a one-dimensional (1-D) metal or a 1-D semiconductor with a band gap on the order of 0.6 eV[2, 3]. Recent work has shown that semiconducting nanotubes can exhibit transistor action that is similar in operation to a MOSFET[1, 4]. In these experiments, a gate electrode is used to electrostatically vary the charge density in the nanotubes. The dependence of the conductance on the carrier density indicates that the carriers added to the tubes are holes.

Besides using a gate, another way to change the charge density in a semiconductor is by chemical doping. Previous work on mats of SWNTs has shown that potassium acts an electron donor to the nanotubes[5] and that their conductance is increased significantly by doping with potassium vapor[6, 7]. However, the interpretation of these experiments is complicated by the fact that mats consist of both semiconducting and metallic nanotubes, and that transport through the mats includes hopping between nanotubes and/or bundles.

Here we report the controlled chemical doping of semiconducting nanotube ropes with potassium. After doping, the carriers in the doped ropes are electrons. We estimate the number of carriers added and hence the number of intercalated potassium atoms. In addition we determine an effective mobility μ_{eff} for the electrons, which is found to be similar in magnitude to the value reported for holes[1].

The samples are made by placing ropes on top of Au electrodes that have 500 nm separation[8] as shown in the inset to Fig. 5-2. These electrodes are on top of a

degenerately doped oxidized Si wafer[9]. The degenerately doped substrate is used as a gate. Once the samples are made, semiconducting and metallic devices are distinguished by their room temperature conductance behavior with respect to gate voltage. The conductance of metallic tubes shows relatively little dependence on gate voltage, whereas the conductance of semiconducting nanotubes shows a very strong dependence[4, 10]. An example of semiconducting behavior is shown in Fig. 5-1. The open circles in Fig. 5-1 show the conductance of a 3 nm diameter rope with as a function of gate voltage. At positive gate voltages, the conductance of the rope approaches zero. As a negative gate voltage is applied, the conductance begins to increase as holes are added to the rope[4]. This increase in conductance is approximately linear in gate voltage. A similar slope has been found in all the samples we have studied to within a factor of three.

Once we have obtained samples that show the above semiconducting behavior, we then dope them with potassium. These doping experiments were carried out in a controlled environment to prevent the potassium from reacting chemically with oxygen. The doping vessel is essentially a glass tube that has wire feedthroughs in order to enable transport measurements. A diagram of the doping vessel is shown in the inset of Fig. 5-2. In an argon atmosphere, potassium is placed in the doping vessel at the opposite end from the sample. The potassium end of the doping vessel is then sealed with a

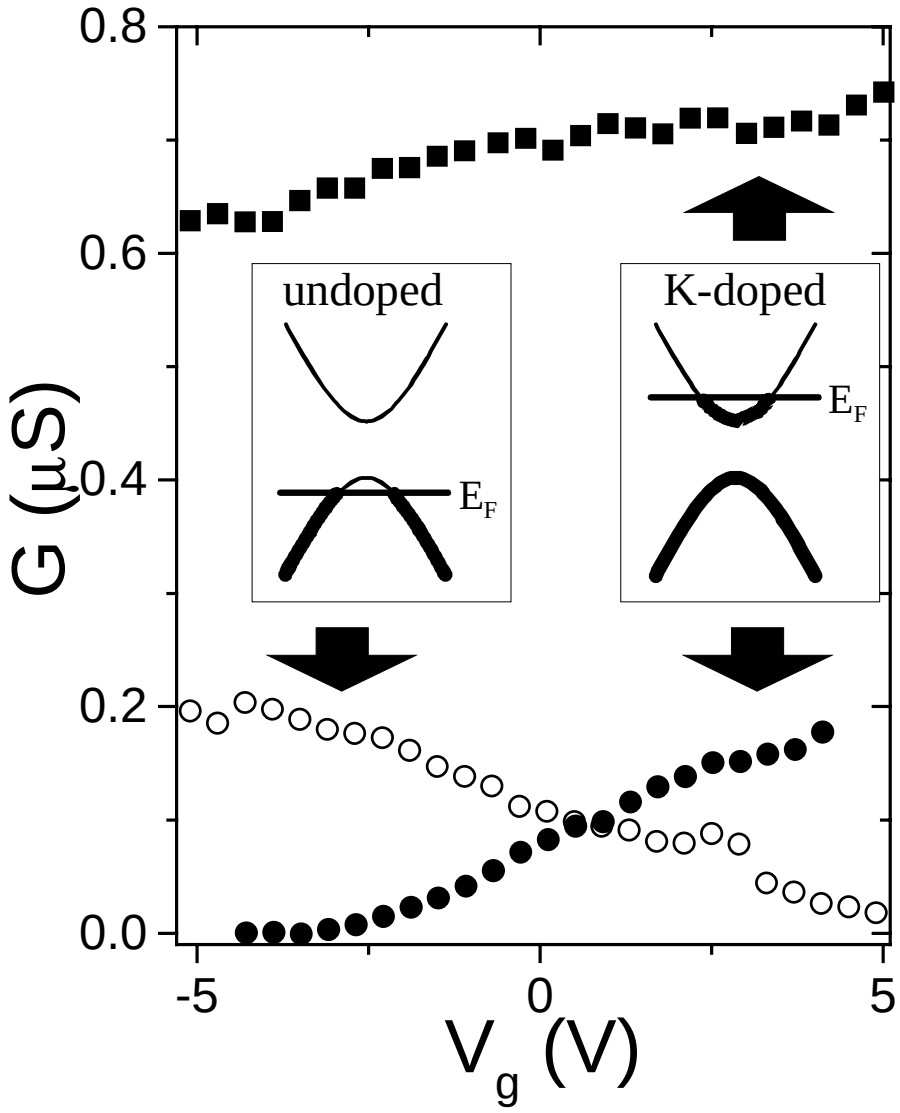

Figure 5-1: Open circles: Conductance vs. gate voltage for an undoped nanotube rope. The conductance increases with decreasing gate voltage, indicating p-type behavior. The left inset shows a schematic band structure diagram corresponding to this situation. Filled squares: Conductance of a different sample after doping with potassium. Filled circles: same sample after a cycle of de-intercalation and re-intercalation at a lower doping level. The conductance increases with increasing gate voltage, indicating n-type behavior. The right inset shows a schematic band structure diagram corresponding to this situation.

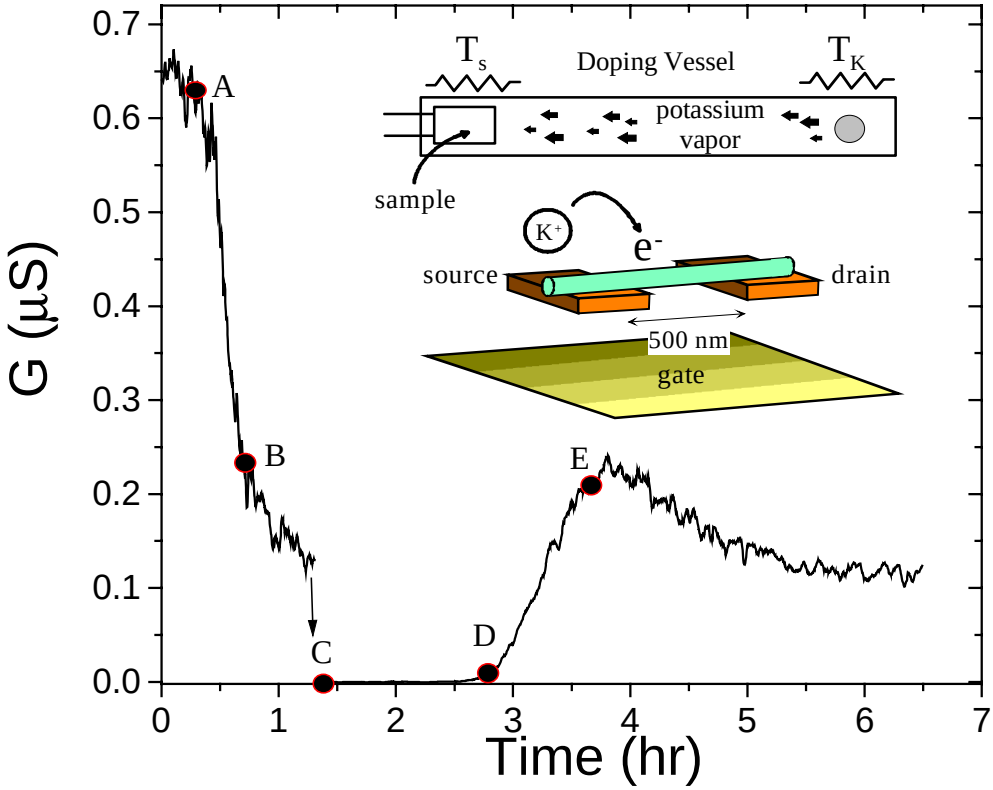

Figure 5-2: Main panel: Conductance of potassium-doped semiconducting sample vs. time. At point A heat was applied to the sample to de-intercalate potassium from the doped sample. At point B heating was stopped temporarily. At point C further heating resulted in the sample becoming insulating. Heat was then applied to the potassium. At point D, the vapor pressure of the potassium is sufficient to begin doping the sample. At point E, heating is stopped and the entire vessel begins to return to room temperature. Inset: diagram of doping vessel and device geometry.

valve. Finally, the vessel is connected to a pump and is evacuated through the attached valve.

The doping vessel is heated differentially by heaters on each end of the vessel. The temperature at each end is measured with thermocouples. The temperature at the sample end is denoted by T_s and the temperature at the potassium end is denoted by T_K. We have performed doping experiments on several samples. All of the samples yielded similar results. However, all the potassium doping data shown here is taken from a single sample.

Prior to heating the potassium, the sample is heated (T_s~400 K) while the vessel is attached to the pump. During this procedure, we find that the conductance of undoped semiconducting nanotubes decreases dramatically until the sample becomes insulating. Although we do not fully understand this behavior, we have considered two possibilities. One is that the semiconducting nanotubes become insulating as a result of changes in the local electrostatic environment of the nanotube (*e.g.* neutralization of trapped oxide charge). Another possibility is that they may be doped by molecular species that are adsorbed from the air, which are removed by heating in vacuum. A more complete understanding of this will require further work.

Following the bake-out, we have found that heating the potassium briefly with a flame causes the conductance of semiconducting nanotubes to increase from zero to a finite value. Since the potassium donates electrons to the nanotubes one expects to be able to observe n-type behavior in the doped nanotubes. Indeed, we find that this is the case, as shown in Fig. 5-1. The data plotted with filled squares in Fig. 5-1 shows the

conductance of the doped rope as a function of gate voltage after exposure to potassium vapor. Unlike what is observed for intrinsic nanotubes, the conductance of the doped nanotubes increases with increasing gate voltage. This implies that the carriers are electrons, rather than holes[11].

We have found that this doping is reversible. The main panel of Fig. 5-2 shows the conductance of a semiconducting sample after the initial potassium doping. No gate voltage is applied, unless otherwise noted. At point A, the conductance is relatively stable at a value of ~0.6 μS. At this point, we applied heat to the sample (T_s~400 K.) As time evolves, the sample becomes less conductive as the potassium is de-intercalated and electrons are removed[6, 7]. We stopped heating the sample at point B, at which time the conductance begins to stabilize at a value of ~0.1 μS. Further heating caused the sample to become insulating (not shown,) implying that the majority of the intercalated potassium has been removed.

To add potassium to the sample in a controlled way, we heated both the sample and the potassium simultaneously using the heaters. Throughout this procedure, the sample was maintained at a slightly higher temperature than the potassium (T_s-T_K~20 K) to avoid gross deposition of potassium on the sample. At point C, T_K = 400 K, while T_s = 420 K. At this point, the vapor pressure of the potassium is insufficient to dope the sample, and it remains insulating. At point D, T_K = 450 K, and the vapor pressure of the potassium becomes large enough to begin doping the sample. As time evolves, the conductance increases. At point E both the sample and the potassium are allowed to cool to room temperature. Upon cooling down from point E, the conductance decreases until the temperature stabilizes at room temperature, and the conductance stabilizes at G

~ 0.12 μS. The filled circles in Fig. 5-1 show the conductance of the sample as a function of gate voltage after this procedure. At negative gate voltages, the sample is insulating. At a threshold voltage V_{th} ~ -3.8 V, the conductance begins to increase, rising approximately linearly with gate voltage.

We now discuss these results. First, we estimate the number of potassium atoms added to the sample. When the gate voltage is zero, the charge density in the ropes is determined by their local electrostatic environment, which includes the ionized potassium donors. If we make the assumption that when the device is off that the electrons in the rope are depleted, then the number of electrons n_e at $V_g = 0$ will be given by $en_e = C_{L|}V_{th|}$. Here, C_L is the capacitance per unit length of the rope to the gate electrode. Measurements of metallic nanotubes in a similar geometry in the Coulomb blockade regime give a typical value C_L ~ 20 e^-/V-μm[9]. With the approximation that at $V_g = 0$ each potassium atom donates an electron to the rope, we have $n_K \sim n_e$. Thus from the data shown in Fig. 5-1 as filled circles we conclude that n_K ~ 100 μm^{-1}. For the higher conductance data (filled squares) we estimate that the number of carriers is n_K ~ 700 μm^{-1} from the ratio of the conductance between the two doping levels at $V_g = 0$. In comparison to the KC_8 stoichiometric doping levels reported by Lee *et al.* and Grigorian *et al.*[6, 7], this is therefore very light doping.

We note that similar to the case of p-type semiconducting nanotubes[1], the increase in conductance is approximately linear in gate voltage. We can thus determine an effective mobility for the carriers: $\mu_{eff}=L^2/C\ dG/dV_g$, where L is the length of the sample, C is the capacitance G is the conductance and V_g is the gate voltage. For the undoped sample in Fig. 5-1 we find that the hole mobility is given by μ_{eff}~ 60 $cm^2\ V^{-1}\ s^{-1}$

in agreement with values reported by others[1]. For the doped sample, the higher conductance data in Fig. 5-1 (solid squares) yields $\mu_{eff} \sim 20$ cm^2 V^{-1} s^{-1}, while the lower conductance data (filled circles) yields $\mu_{eff} \sim 60$ cm^2 V^{-1} s^{-1}. These values for the electron effective mobility are thus similar to typical values for the hole effective mobility. This indicates that the scattering mechanism for electrons and holes is likely similar.

In conclusion, we report the chemical doping of individual semiconducting nanotube ropes with potassium. We find that this chemical doping changes their conductance from zero to a value on the order of one μS. From the gate voltage dependence of the conductance, we deduce that the charge carriers are electrons. This is explained by a model in which the potassium donates electrons to the nanotube rope, resulting in mobile charge carriers at the Fermi level. The effective mobility for the electrons is similar in magnitude to the effective mobility of holes. These experiments open the way toward other experiments that require controlled doping, such as making nanoscale p-n junctions.

We would like to thank Steven G. Louie and Marvin Cohen for helpful discussions, and G. Y. McLean for experimental assistance. This work was supported by DOE (Basic Energy Sciences, Materials Sciences Division, the sp^2 Materials Initiative).

References

This chapter has been submitted to Applied Physics Letters.

1 R. Martel, T. Schmidt, H. R. Shea, *et al*., Applied Physics Letters **73**, 2447 (1998).

2 T. W. Odom, H. Jin-Lin, P. Kim, *et al*., Nature **391**, 62 (1998).

3 J. W. G. Wildoer, L. C. Venema, A. G. Rinzler, *et al*., Nature **391**, 59 (1998).

4 S. J. Tans, R. M. Verschueren, and C. Dekker, Nature **393**, 49 (1998).

5 A. M. Rao, P. C. Eklund, S. Bandow, *et al*., Nature **388**, 257 (1997).

6 R. S. Lee, H. J. Kim, J. E. Fischer, *et al*., Nature **388**, 255 (1997).

7 L. Grigorian, G. U. Sumanasekera, A. L. Loper, *et al*., Phys. Rev. B (Condensed Matter) **58**, R4195 (1998).

8 S. J. Tans, M. H. Devoret, H. Dai, *et al*., Nature **386**, 474 (1997).

9 D. H. Cobden, M. Bockrath, P. L. McEuen, *et al*., Phys. Rev. Lett. **81**, 681 (1998).

10 We note that none of the procedures described hereafter have a significant effect on metallic tubes, and thus we will focus exclusively on the properties of semiconducting tubes.

11 We have never seen n-type behavior in undoped samples, even at large positive gate voltages. We believe that this is because in the back gated geometry the contact region is screened from the gate by the leads. Thus the contact regions remain p-type regardless of the gate voltage, preventing the injection of charge into the n-type region.

Chapter 6

Disorder, pseudospins, and backscattering in carbon nanotubes

Paul L. McEuen, Marc Bockrath, David H. Cobden*, Young-Gui Yoon, and Steven G. Louie

Department of Physics, University of California and Materials Sciences Division, Lawrence Berkeley National Laboratory, Berkeley, California, 94720

Abstract

We address the effects of disorder on the conducting properties of metal and semiconducting carbon nanotubes. Experimentally, the mean free path is found to be much larger in metallic tubes than in doped semiconducting tubes. We show that this result can be understood theoretically if the disorder potential is long-ranged. The effects of a pseudospin index that describes the internal sublattice structure of the states lead to a suppression of scattering in metallic tubes, but not in semiconducting tubes. This conclusion is supported by tight-binding calculations.

Single-wall carbon nanotubes (SWNTs) are two-dimensional (2D) graphene sheets rolled into nanometer-diameter cylinders[1,2] that can either be 1D metals or semiconductors, depending on how the sheet is rolled up. This surprising behavior follows from the unusual band structure of a graphene sheet. It is a semimetal with a vanishing gap at the corners of the first Brillouin Zone (BZ) where the π (bonding) and π* (antibonding) bands touch at two inequivalent wavevectors ***K*** and ***K'***. (Fig. 6-1A). As the Fermi level moves due to chemical or electrostatic doping, the Fermi surface becomes circular arcs at the corners of the BZ, as is shown in Fig. 6-1A for hole doping. This Fermi surface can be more simply represented in the extended zone scheme by piecing together the arcs to form Fermi circles of radius *k* centered around ***K (K')*** point. When a graphene sheet is rolled up into a tube, the allowed wavevector components perpendicular to the tube axis become quantized, resulting in 1D subbands with allowed *k*'s represented by dashed lines in Figures 6-1B and 6-1C. For metallic tubes (Fig. 6-1B), one set of allowed wavevectors goes through the ***K*** point and there are propagating modes at E_f at $+k$ and $-k$. This 1D mode has a linear (massless) dispersion, as is indicated in the Figure. For semiconducting tubes (Fig. 6-1C), the allowed wavevectors do not go through the ***K*** point. For small ***k***, there are thus no allowed states at E_f, but if the tube is doped sufficiently, the Fermi circle reaches the nearest 1D subband and propagating modes exist, whose (massive) dispersion is shown in the Figure.

A wealth of scanned probe and electrical transport measurements have been performed to probe the electronic structure and conducting properties of SWNTs[2].

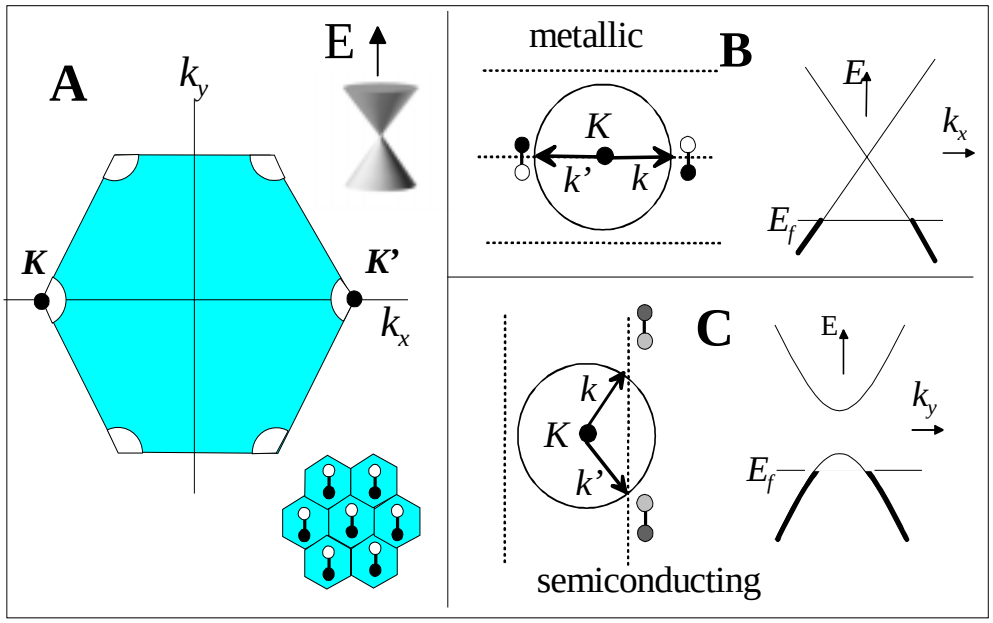

Figure 6-1 A) Filled states (shaded) in the first Brillouin Zone of a single p-type graphene sheet. The sheet contains of two carbon atoms per unit cell (lower right inset). The dispersions of the states in the vicinity of E_f are cones (upper right inset) whose vertices are located at the ***K*** and ***K'*** points. The Fermi circle around the ***K*** point, the allowed *k* vectors, and their dispersion are shown in B) and C) for a metallic and semiconducting tube, respectively. The dumbbells represent the molecular orbitals comprising the states, with white-white, white-black, and gray dumbells representing a bonding, antibonding, and mixed orbitals, respectively.

Overall, the experimental results agree with the predictions of band structure given above. Many interesting open issues remain, however, particularly concerning the effect Coulomb interactions[3-6] and disorder[7-9]on the electronic states. For example, recent theoretical work has emphasized that the effects of disorder may be significantly reduced in SWNTs for a number of reasons[7-9]. Experiments indeed give compelling evidence that a *metallic* tube can have a very long mean free path ℓ - on the order of microns[10-14] Initial experiments on doped *semiconducting* tubes, however, have yielded ℓ's that are orders of magnitude shorter[15,16]. This is perhaps surprising, since the tubes are nearly structurally identical and the amount of disorder likely very similar. In this letter, we address this apparent discrepancy between the properties of metallic and doped semiconducting nanotubes.

We begin by discussing the experimental evidence that ℓ can be very long in metallic SWNTs. Figure 6-2 shows a measurement of a nanotube rope ~ 8μm in length. At low *T*, Coulomb oscillations in the conductance *G* vs. gate voltage V_g are observed as electrons are added to the rope [10,11]. Using the charging energy U ~ 0.5 meV determined from the *T*-dependence, the effective length L_{eff} of the segment of tube to which the electrons are added can be estimated [10,11]. For this device, we find L_{eff} ~ 10 μm, which is approximately the physical tube length, as previously observed by the DELFT group[10]. Note that any significant backscattering within the tube would localize the electronic states on the scale of ℓ and effectively break the tube into a series of dots[17]. This would result in multiple Coulomb blockade periods as a function of V_g

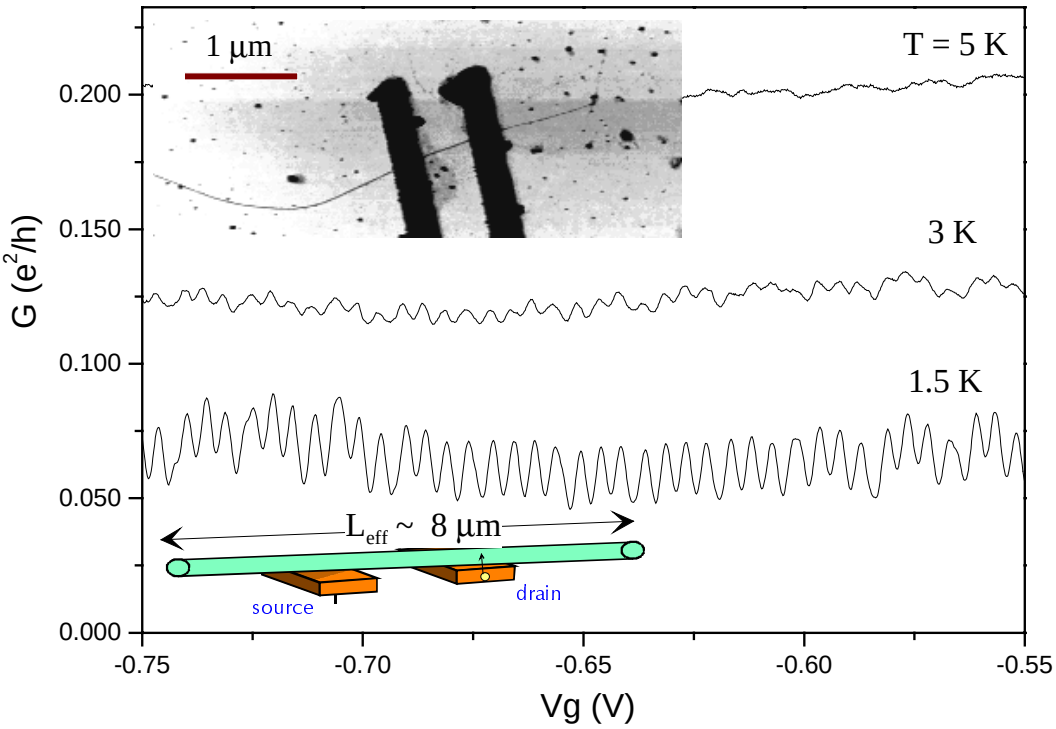

Figure 6-2. Conductance versus gate voltage at different temperatures for the metallic nanotube device shown in the upper inset. The 3 nm diameter and 8 μm long nanotube rope is draped over 2 contacts that make tunnel contact to a metallic tube in the rope. A voltage applied to the doped substrate is used to adjust the carrier density. The appearance of the CB oscillations only at very low temperatures (~1.5 K) indicates that the electrons are delocalized over the entire length of the tube, an indicated in the lower inset.

with larger charging energies. The observation of a single, well-defined, and small charging energy is thus very strong evidence that ℓ is many μms in length.

Additional evidence for large ℓ's comes from measurements of the two terminal conductance of nanotubes with near-ohmic contacts. For perfect contacts, the conductance is predicted to be: $G = (e^2/h)\sum T_i$, where T_i is the transmission coefficient for each of the four 1D channels propagating through the tube. Measurements by a number of groups[11,13,14] have yielded conductances ~ e^2/h, indicating that the T_i*'s* can be on the order of unity, even for tubes many microns in length. Clearly, then, metallic tubes can have mean free paths at the micron length scale.

We now turn to experiments on semiconducting tubes. Tans *et al*.[15] and Martel *et al*.[16] measured electrostatically doped *p*-type tubes and Bockrath *et al*.[18] measured *n*-type tubes that were chemically doped. These results can be analyzed using a model of a diffusive conductor. In the simplest version, transport though the tube is limited by scatterers spaced at a distance ℓ, each with transmission probability T_i ~ ½. The conductance of a tube of length L is then: G ≅ ($4e^2/h$) (ℓ/L). Using the physical length of the tube and the maximum measured conductance, these experiments indicate ℓ ~ 2nm at the largest carrier densities. This is *three orders of magnitude* shorter than the ℓ found above for metallic tubes.

To investigate this striking discrepancy further, we have performed extensive measurements on semiconducting tubes at both room and low temperatures. Figure 6-3 shows the G vs. V_g measured one device. At room temperature, the conductance increases as V_g is decreased and holes are added to the valence band of the semiconducting tube. (The saturation of G at large negative V_g is believed to be due to

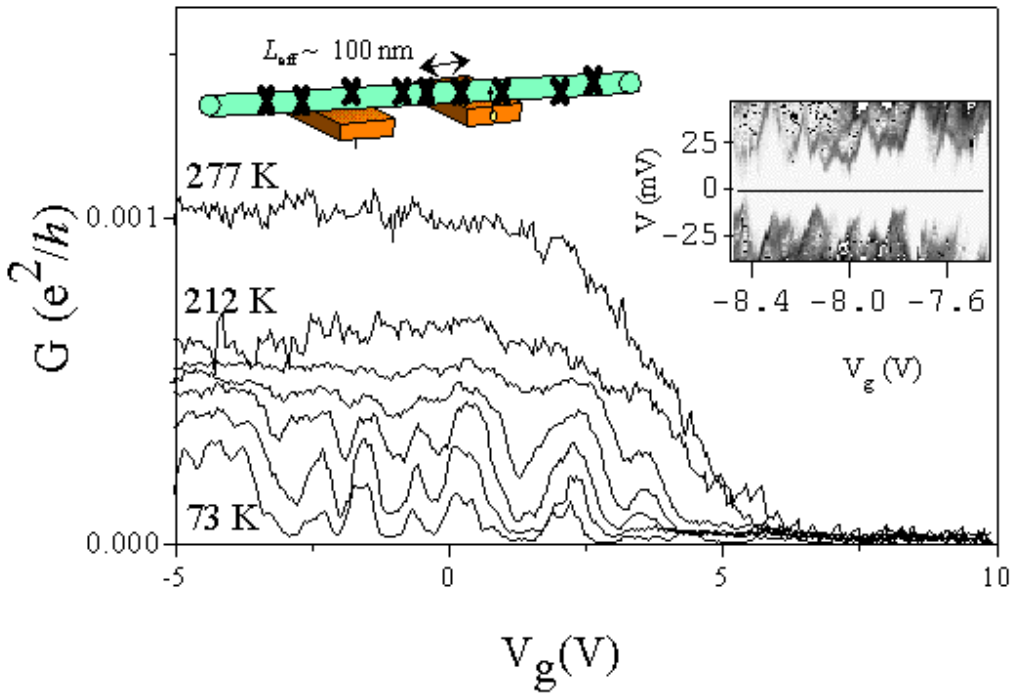

Figure 6-3. G vs. V_g for a semiconducting nanotube device with contacts separated by 0.5 μm. Holes are added to the tube below V_g = 5 V and the tube becomes conducting. Irregular Coulomb oscillations are observed below T ~ 150 K. The lower inset shows dI/dV vs. V and V_g plotted as a gray scale for a second device at T = 4.2 K. Complex structure consistent with transport through a number of quantum dots in series is seen. The T-dependence and typical charging energy indicates that the tube is broken up into segments of length L_{eff} ~ 100 nm, as indicated in the schematic.

the contact resistance for tunneling into to the tubes[15,16].) As T is lowered, G is suppressed and breaks up into a series of peaks as a function of V_g. At low temperatures (T < 20 K), G is immeasurably small at all V_g. The lower inset to Fig. 6-3 shows the differential conductance, dI/dV, for a different semiconducting tube device as a function of V_g and V at T = 4.2 K. The data is plotted as a gray scale. There is a gap around the origin where dI/dV = 0. This gap shows complex behavior as a function of V_g and is followed by a finite conductance region above V ~ 25 - 50 mV. Qualitatively similar results have been obtained on a number of devices consisting of both ropes and single tubes (as determined by AFM measurements of the rope/tube height).

The data in Fig. 6-3 are highly reminiscent of measurements of the Coulomb blockade for a number of dots in series[19,20]. In these systems, an electron must hop through a series of quantum dots, each with a typical charging energy U, for current to flow. Since at any V_g, some of the dots will be blockaded, dI/dV = 0 at low energies. Thermal energies kT or finite bias energies eV on the order U are required to overcome the Coulomb blockade and produce a finite conductance. We therefore conclude that in semiconducting tubes disorder effectively breaks the tube into a series of dots separated by tunnel barriers, as is schematically illustrated in the inset to Fig. 6-3. The conductance is thus determined by tunneling through a series of quantum dots.

We can estimate the size of these disorder-induced dots from the temperature and bias dependence of the Coulomb blockade features. Since the features appear at energy scales 100 times larger than for the metallic tube in Fig. 6-2, we find L_{eff} ~ 100 nm. Since the device is ~ 500 nm long, this implies that the effective sample consists ~ 5 dots

in series. From the conductance at room temperature, where charging effects are minimal, we estimate that the tunnel barriers between the dots each have transmission probabilites ~ 0.001-0.1.

These measurements indicate that the diffusive transport model discussed previously – consisting of a large number of scatterers each with $T_i \sim ½$ - is inappropriate for these samples. Instead, strong disorder over a much longer length scale better describes this system. It is still the case, however, that $G << e^2/h$, indicating that semiconducting tubes are much more strongly influenced by disorder than metallic tubes.

To understand this difference, we first review in detail the nature of the electronic states in graphite near E_f. The band structure in the vicinity of the ***K (K')*** point can be described within the ***k*p*** approximation by a 2D Dirac Hamiltonian for massless fermions, $H = \hbar v_F \sigma \cdot k$ [21]. Here ***k*** is the wavevector measured relative to the ***K (K')*** point and the σ's are the Pauli matrices. This Hamiltonian is well-known in both condensed-matter and particle physics; in the latter case, it is used to describe, *e.g.* a 2D massless neutrino. The states and their corresponding energies are given by[8,9,21]:

$$| k >= \frac{1}{\sqrt{2}} e^{ik\cdot r} \begin{pmatrix} -ibe^{-i\theta_k/2} \\ e^{i\theta_k/2} \end{pmatrix} \quad ; \qquad E = b\hbar v_F |k| \tag{1}$$

where θ_k is the angle that ***k*** makes with the y-axis in Fig. 6-1A and b = 1(-1) for states above(below) the energy at ***K***. Eq. 1 shows that, in addition to their real spin, the electrons possess a pseudospin - a two-component vector that gives the amplitude of the electronic wavefunction on the two sublattice atoms. Inspection of Eq. 1 reveals that

the spinor is tied to the ***k*** vector such that it always points along ***k***. This is completely analogous the physical spin of a massless neutrino which points along the direction of propagation. The states around ***K*** correspond to right-handed neutrinos (pseudospin parallel to ***k***), whereas those around ***K'*** are left-handed (pseudospin antiparallel to ***k***). For the antiparticles ($b = -1$) this situation is reversed. Physically, this pseudospin means that the character of the underlying molecular orbital state depends upon the propagation direction. For example, a negative energy state near ***K*** with a positive k_x is built from a anti-bonding molecular orbitals while the state with $-k_x$ is built from bonding orbitals. This is schematically indicated in Fig. 6-1B.

Following Ando and collaborators[8,9], we now consider scattering between these allowed states in a carbon nanotube due to *long-range disorder*, i.e. disorder with Fourier components $V(\boldsymbol{q})$ such that $\boldsymbol{q} << \boldsymbol{K}$. In this case, the disorder does not couple to the pseudospin portion of the wavefunction since the disorder potential is approximately constant on the scale of the inter-atomic distance. The resulting matrix element between states is then[8]: $|< k'|V(r)|k >|^2 = |V(k-k')|^2 \cos^2(\frac{1}{2}\theta_{k,k'})$, where $\theta_{k,k'}$ is the angle between the initial and final states. The first term is just the Fourier component at the difference in the k values of the initial and final envelope wavefunctions. The *cos* term is the overlap of the initial and final spinor states.

For a metallic tube (Fig. 6-1B), backscattering in the massless subband corresponds to scattering between $|k_x >$ and $|-k_x >$. Such scattering is forbidden, however, since the molecular orbitals of these two states are orthogonal, as was clearly emphasized by Ando et al.[8,9]. In semiconducting tubes, however, the situation is quite different (Fig. 6-1C). The angle between the initial and final states is $< \pi$, and scattering

is thus only partially suppressed by the spinor overlap. As a result, semiconducting tubes should be sensitive to long-range disorder, while metallic tubes should not. Note that *short-range disorder*, $\boldsymbol{q} \sim \boldsymbol{K}$, will couple the molecular orbitals together and lead to scattering in all of the subbands.

To support this picture, we have performed tight-binding calculations of the conductance G of metal and semiconducting tubes in the presence of a scattering potential. We employ the Landauer formalism to calculate the conductance from the transmission coefficients T_i of each subband. A Gaussian disorder potential of the form $V(r) = V_o \exp(-r^2/2\sigma^2)$ centered on one of the atoms on the nanotube wall is included in the tight-binding Hamiltonian. The transmission coefficients are obtained from boundary condition matching between the disorder-free region and the disordered region.

In Fig. 6-4, the calculated *G(E)* is shown for two realizations of a single Gaussian scatterer with the same integrated strength but different widths corresponding to long-range (dashed lines) and short-range disorder (dash-dot lines). The massless 1D band of a metallic tube is unaffected by a long-range scatter, but there is significant backscattering of the states in the semiconducting tube in the region near the threshold for transmission. There is also backscattering of the higher subband states of the metallic tube, as is expected from extending the arguments above. This calculation clearly demonstrates that the two types of subbands (massive and massless) are affected very differently by long-range disorder in a manner accurately captured by the physics of the pseudospin discussed above.

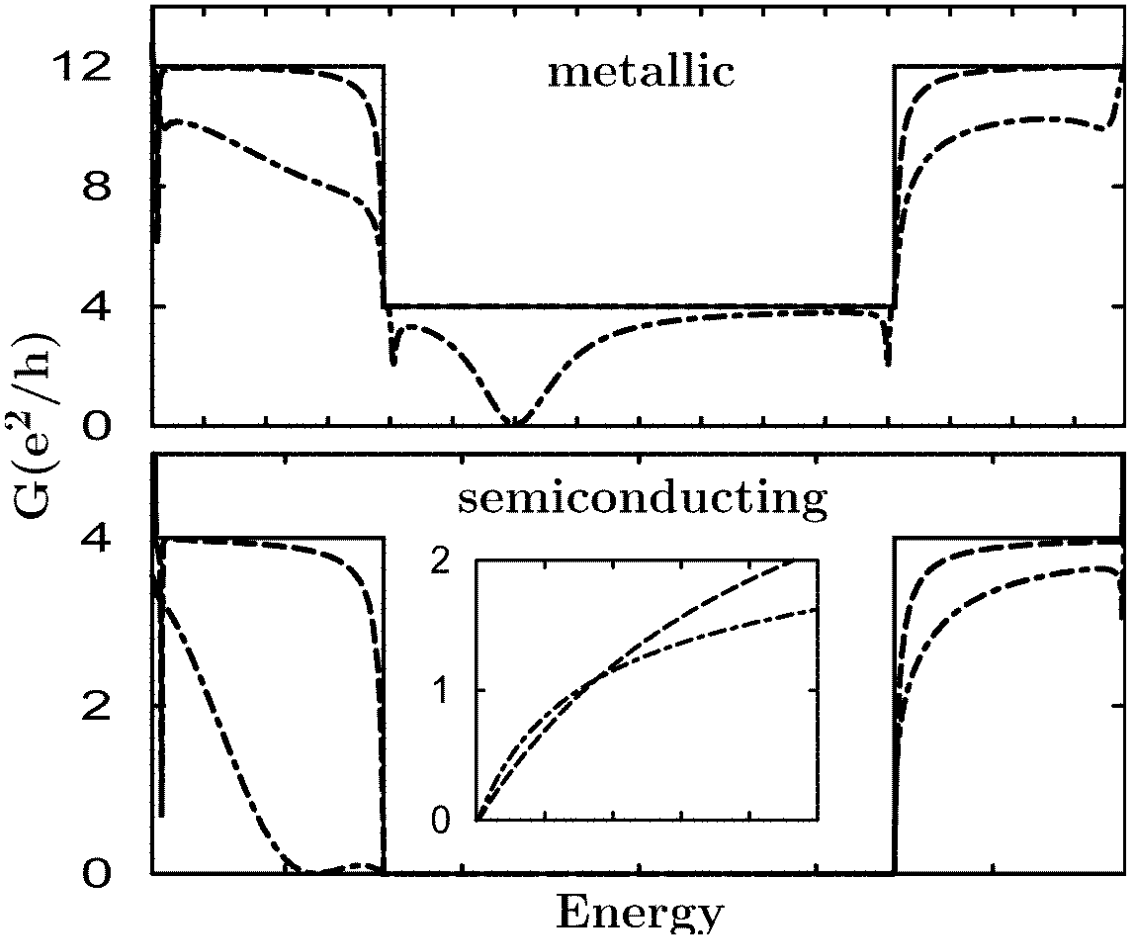

Figure 6-4. Tight-binding calculation of the conductance of an A) metallic (10,10) tube and B) semiconducting (17,0) tube in the presence of a Gaussian scatterer. The energy scale on the abscissa is 0.2 eV per division in both graphs. The solid lines show the results for a disorder free tube, while the dash and the dot-dash lines are for, respectively, a single long-range (σ = 0.348 nm, ΔV = 0.5 eV) and short range (σ = 0.116 nm, ΔV = 10 eV) scatterer centered on the wall of the tube. Here ΔV is the shift in the on-site energy at the potential center. The massless band of the metallic tube is unaffected by the long-range scatterer, unlike the massive bands of the metallic and semiconducting tube. All subbands are influenced by the short-range scatterer. The inset shows an expanded view of the onset of conduction in the semiconducting tube at positive E, with each division corresponding to 1 meV. To compare to the experimental data, we estimate that a gate voltage change V_g of 1 V in Figure 6-3 corresponds to a chemical potential change E of the on the order of 1 meV.

These theoretical considerations agree very well with the experimental results. Long-length scale disorder due to, e.g. localized charges near the tube, breaks the semiconducting tube into a series of quantum dots with large barriers and a dramatically reduced conductance. Metallic tubes, on the other hand, are insensitive to this disorder and remain near-perfect 1D conductors. In the future, it will be great interest to explore other experimental manifestations of this pseudospin degree of freedom in graphene materials.

We wish acknowledge useful and enlightening discussions with Dung-Hai Lee and thank the Smalley group for the nanotube material used in these studies. Y. Yoon acknowledges discussions with Hyoung Joon Choi and the use of his tight binding code. This work was supported by DOE, Basic Energy Sciences, Materials Sciences Division, the sp^2 Materials Initiative and by NSF DMR-9520554.

References

This chapter has been submitted to Physical Review Letters.

* Present Address: Oersted Laboratory, Neils Bohr Institute, Universitetsparken 5, DK-2100 Copenhagen, Denmark.

1 M. S. Dresselhaus, G. Dresselhaus, and P. C. Eklund, *Science of Fullerines and Carbon Nanotubes* (Academic, San Diego, 1996).

2 For a recent review, see C. Dekker, Physics Today **52**, 22 (1999).

3 C. Kane, L. Balents, and M. P. A. Fisher, Phys. Rev. Lett. **79**, 5086 (1997).

4 Y. A. Krotov, D.-H. Lee, and S. G. Louie, Phys. Rev. Lett. **78**, 4245 (1997).

5 R. Egger and A. O. Gogolin, Phys. Rev. Lett. **79**, 5082 (1997).

6 M. Bockrath *et al*., Nature **397**, 598 (1999).

7 C. T. White and T. N. Todorov, Nature **393**, 240 (1998).

8 T. Ando, T. Nakanishi, and R. Saito, J. Phys. Soc. Jpn. **67**, 2857 (1998).

9 T. Ando and T. Nakanishi, J. Phys. Soc. Jpn. **67**, 1704 (1998).

10 S. J. Tans *et al*., Nature **386**, 474 (1997).

11 M. Bockrath *et al*., Science **275**, 1922 (1997).

12 S. Frank *et al*., Science **280**, 1744 (1998).

13 A. Y. Kasumov *et al*., Science **284**, 1508 (1999).

14 H. T. Soh *et al*., preprint (1999).

15 S. J. Tans, R. M. Verschueren, and C. Dekker, Nature **393**, 49 (1998).

16 R. Martel *et al*., Appl. Phys. Lett. **73**, 2447 (1998).

17 A. Bezryadin *et al*., Phys. Rev. Lett. **80**, 4036 (1998).

18 M. Bockrath *et al*., preprint (1999).

19 A. A. M. Staring, H. van Houten, and C. W. J. Beenakker, Phys. Rev. B **45**, 9222 (1992).

20 V. Chandrasekhar, Z. Ovadyahu, and R. A. Webb, Phys. Rev. Lett. **67**, 2862 (1991).

21 C. L. Kane and E. J. Mele, Phys. Rev. Lett. **78**, 1932 (1997).

Chapter 7

Electrons in One Dimension: Theory

7.1 Introduction

Interacting electrons in 2- and 3-D are well described in terms of an approximate model of weakly-interacting quasiparticles, namely Fermi liquid theory. This model has been highly successful in explaining the properties of 2- and 3-D conductors. However, this approximate picture does not hold in one dimension. Instead, the ground state of an interacting 1-D electron gas (I1DEG) is a strongly correlated state known as a Luttinger liquid. (For review, see *e.g.*[1].) Unlike in a Fermi liquid, in a Luttinger liquid the low-energy excitations are bosonic sound-like density waves (plasmons).

One way to observe this Luttinger liquid behavior experimentally is to inject electrons into a 1-D system from an external lead through a tunneling contact and measure the resulting current. By varying the energy of the injected electrons, one can measure the tunneling rates as a function of energy. To first order and at zero temperature, these tunneling processes are described by:

$$\rho_{tun}(eV) = \frac{dI}{dV} = \frac{2e^2}{h} |M|^2 \, \rho_{lead}(E_F)\rho_{system}(E_F + eV), \qquad (1)$$

which relates the tunneling density of states ρ_{tun} at a given energy to the product of a matrix element M and the (joint) density of states $\rho_{lead}(E_1)\rho_{system}(E_2)$. One usually neglects both the energy dependence of the matrix element and the energy dependence of the density of states in the metal lead. For this reason, the differential conductance is

often referred to as the "tunneling density of states" of the system being probed by the leads, although in general the measured *dI/dV* depends on the tunneling matrix element as well. In particular, for interacting electrons the dependence of the tunneling rate on the matrix element may be very important. This is the case in 1-D, where the sudden creation of an electron in the I1DEG requires the superposition of an infinite number of plasmons. The resulting orthogonality catastrophe leads to a vanishing of the tunneling matrix elements near the Fermi level.

Our goal in this chapter is to calculate the tunneling density of states for carbon nanotubes using a phenomenological model of the Luttinger Liquid. To formulate this model, we will first find a Lagrangian that describes the low-energy behavior of a non-interacting 1-D wire with a single spinless mode. From this viewpoint, adding electron-electron interactions will then become straightforward. Finally, we will consider the more complicated case of electrons in nanotubes, where there are four conducting modes at E_F.

7.2 Low-energy Lagrangian for a single spinless mode

To find a Lagrangian that describes the low-energy behavior of a 1-D wire, we will find expressions for the kinetic and the potential energy in terms of a slowly varying change in the electron density from the ground state. The ground state of the 1-D wire, taken to have zero total energy, is shown in Figure 7-1A by the solid black lines. The 1-D momentum states are filled up to the Fermi level E_F. To find the potential energy V per unit length when the charge density is locally increased by an amount ρ, we consider

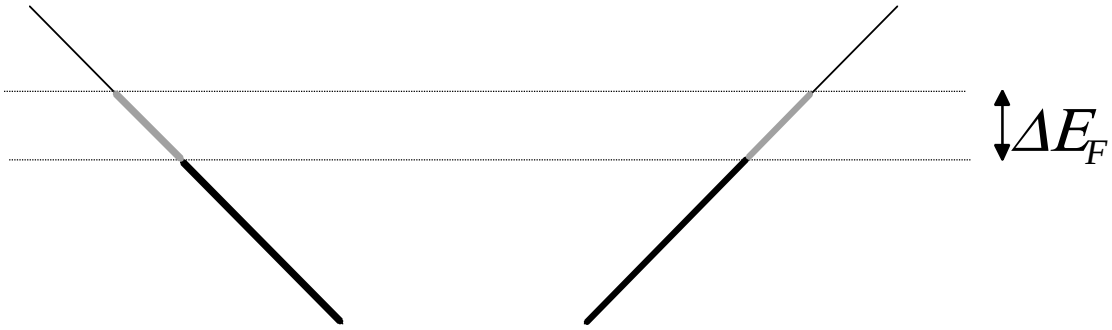

Figure 7-1A: The local Fermi level of a 1D wire is increased by adding charge (shown in gray).

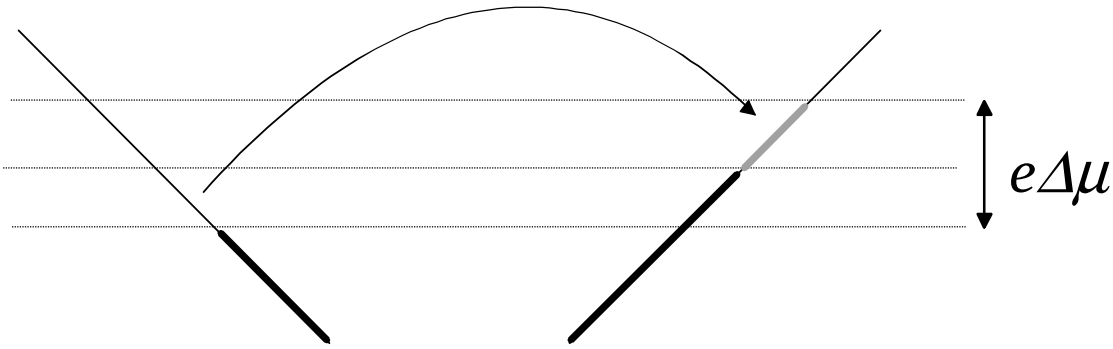

Figure 7-1B: A current is established by taking left movers in the energy range $e\Delta\mu/2$ and changing them to right movers

adding N electrons to a region of length $L>>\lambda_F$, where λ_F is the Fermi wavelength. This results in an increase in the local Fermi level by ΔE_F, as indicated schematically in Figure 7-1A by the solid gray lines. The increase in the energy per unit length is

$$V = \frac{1}{L}\int_0^N \frac{1}{2} n\delta dn = \frac{1}{4L} N^2 \delta \qquad (2)$$

where δ is the level spacing for the right or left movers in a length L:

$$\delta = \frac{dE}{dk}\Delta k = \hbar v_F \frac{2\pi}{L}. \qquad (3)$$

We arrive at the result

$$V = \frac{h}{4e^2} v_F \rho^2. \qquad (4)$$

By comparing this with the expression $V = \rho^2/2\kappa$, where κ is the compressibility of the non-interacting electron gas[1], we arrive at an expression for the compressibility: $\kappa = 2e^2/(hv_F)$.

To find the kinetic energy per unit length T requires an expression for the energy cost to dynamically change ρ. This energy cost is related to the current in the 1-D wire. To find this energy, we calculate the increase in energy when a current is established by taking some left-movers below E_F in an energy range of width $e\Delta\mu/2$ and promoting them to right-movers above E_F. This is shown schematically in Figure 7-1B. The total energy cost is just the number of electrons N= $e\Delta\mu/2\delta$ times the energy added per electron $e\Delta\mu/2$. Thus $T=(e\Delta\mu/2)^2/\delta$. The difference between the chemical potential of the right and left movers can be related to the current in the usual way for a 1-D wire: $I=e^2/\mathrm{h}\ \Delta\mu$. This leads to the result that

$$T = \frac{1}{4v_F}\frac{h}{e^2}I^2. \quad (5)$$

Since this term goes as the current squared, we define a kinetic inductance L such that T=1/2 LI^2. Thus we find $L=h/(2e^2v_F)$.

In terms of the kinetic inductance and the compressibility, we find the following Lagrange density T-V:

$$L = \frac{1}{2}LI^2 - \frac{1}{2\kappa}\rho^2. \quad (6)$$

This is the Lagrange density for a transmission line, with the kinetic inductance playing the role of the usual inductance and the compressibility playing the role of the capacitance.

Once we have the Lagrangian, we can find the equations of motion for the charge density. We expect based on the analogy with the transmission line Lagrangian that the dynamics will be determined by the wave equation. To find these equations in detail, it is helpful to introduce the displacement $\theta(x)$[1]:

$$\theta(x,t) = \int_{-\infty}^{x} \rho(x,t)dx \quad (7)$$

Using the continuity equation

$$\frac{\partial\rho}{\partial t} = -\frac{\partial I}{\partial x}, \quad (8)$$

we find

$$I = -\frac{\partial\theta(x,t)}{\partial t}. \quad (9)$$

in terms of $\theta(x,t)$ the Lagrangian is given by

$$L = \frac{1}{2} L(\partial_t \theta)^2 - \frac{1}{2\kappa}(\partial_x \theta)^2 . \tag{10}$$

Using the Euler-Lagrange equations

$$\partial_t \frac{\partial L}{\partial(\partial_t \theta)} + \partial_x \frac{\partial L}{\partial(\partial_x \theta)} = 0 \tag{11}$$

yields the equation of motion for $\theta(x,t)$:

$$L\partial_t^2 \theta - \frac{1}{\kappa}\partial_x^2 \theta = 0 \tag{12}$$

This is the wave equation, which describes waves propagating at the Fermi velocity:

$$v = \sqrt{\frac{1}{L\kappa}} = v_F . \tag{13}$$

As mentioned earlier, this is in complete analogy to a transmission line. The velocity v_{EM} of the electromagnetic wave propagation is given by $v_{EM}^2 = 1/LC$, where L is the inductance per unit length and C is the capacitance per unit length.

At this point, this Lagrangian does not give any new information about the non-interacting 1DEG. It is clear that the excitations in the non-interacting 1DEG should move at the Fermi velocity. However, from this viewpoint we can account for electron-electron interactions by adding a term to the Lagrangian arising from the self-capacitance per unit length C:

$$L_{\text{int}} = -\frac{1}{2C}\rho^2 . \tag{14}$$

This interaction Lagrangian makes several hidden assumptions that we will discuss later in the context of discussing electrons in nanotubes. For the time being, we note that the effect of this term is to add the real capacitance in series with the quantum capacitance due to the compressibility. The effective capacitance of the I1DEG is then given by

$$\frac{1}{C_{eff}} = \frac{1}{C} + \frac{1}{\kappa}. \tag{15}$$

This leads to an increased wave velocity for the plasmons:

$$v_p = \sqrt{\frac{1}{LC_{eff}}} = \sqrt{\frac{1}{LC} + \frac{1}{L\kappa}}. \tag{16}$$

The strength of the interactions is characterized by the ratio between the plasmon velocity and the Fermi velocity and is represented by the interaction parameter *g*:

$$g = \frac{v_F}{v_p} = (1 + \frac{\kappa}{C})^{-\frac{1}{2}}. \tag{17}$$

Hence $g = 1$ characterizes a non-interacting electron gas, while $g < 1$ for repulsive interactions.

Finally, we also note that

$$\frac{1}{C_{eff}} = Lv_p^2 = g^{-1}\frac{h}{2e^2}v_p, \tag{18}$$

which will be useful later.

7.3 Phenomenological Model for Nanotubes

Applying the above theory for a single spinless mode to electrons in carbon nanotubes is straightforward. The main complication is that a nanotube has four modes at E_F, two channels arising from the electron spin and two channels arising from the sublattice degeneracy that was discussed in Chapter 1. In the absence of electron-electron interactions, the Lagrangian is the sum of the single mode Lagrangians[2-4]:

$$L = \sum_{\sigma\chi}\frac{1}{2}LI_{\sigma\chi}^2 - \frac{1}{2\kappa}\rho_{\sigma\chi}^2, \tag{19}$$

Here σ is the electron spin, and χ is an index specifying which sublattice the electron wavefunction is concentrated on. The electrostatic energy is determined by the total charge density, and thus the interaction Lagrangian is:

$$L_{\text{int}} = -\frac{1}{2C}\left(\sum_{\sigma\chi}\rho_{\sigma\chi}\right)^2 . \tag{20}$$

The appearance of the total charge in the interaction Lagrangian suggests the following basis[2, 4]:

The sum of the spin density on the two sublattices (denoted by a and b,)

$$\rho_{s+} = \frac{1}{2}(\rho_{\uparrow a} - \rho_{\downarrow a} + \rho_{\uparrow b} - \rho_{\downarrow b}), \tag{21}$$

the difference in spin density on the two sublattices,

$$\rho_{s-} = \frac{1}{2}(\rho_{\uparrow a} - \rho_{\downarrow a} - \rho_{\uparrow b} + \rho_{\downarrow b}), \tag{22}$$

the total charge density,

$$\rho_{c+} = \frac{1}{2}(\rho_{\uparrow a} + \rho_{\downarrow a} + \rho_{\uparrow b} + \rho_{\downarrow b}), \tag{23}$$

and the difference in the charge on the two sublattices

$$\rho_{c-} = \frac{1}{2}(\rho_{\uparrow a} + \rho_{\downarrow a} - \rho_{\uparrow b} - \rho_{\downarrow b}). \tag{24}$$

Three of these modes are neutral, and one is charged. Note that because of the normalization factors involved in the change of basis, the charge carried by the charged mode is ½ of the physical charge. In this new basis the Lagrangian is given by

$$L = \frac{1}{2}L(I_{s+}^2 + I_{s-}^2 + I_{c+}^2 + I_{c-}^2) - \frac{1}{2\kappa}(\rho_{s+}^2 + \rho_{s-}^2 + \rho_{c+}^2 + \rho_{c-}^2) - \frac{2}{C}\rho_{c+}^2 . \tag{25}$$

Hence, these modes behave like four independent spinless 1-D modes. Interactions affect only the charged mode, which has a plasmon velocity given by

$$v_p = \sqrt{\frac{4}{LC} + \frac{1}{L\kappa}}. \tag{26}$$

This gives the following value for g_{c+}:

$$g_{c+} = \frac{v_F}{v_p} = (1 + \frac{4\kappa}{C})^{-\frac{1}{2}}, \tag{27}$$

While the $g = 1$ for the three neutral modes. We see that the addition of more modes results in a lower value for g_{c+} compared to a single mode. For a finite size system of length l, Eq. 27 can be written in terms of the mean level spacing $\Delta = h v_F/4l$, and the charging energy $U = e^2/C_{tot}$, where C_{tot} is the total capacitance:

$$g_{c+} = (1 + \frac{2U}{\Delta})^{-\frac{1}{2}}. \tag{28}$$

This expression is useful for direct comparison of theory and experiment.

As mentioned previously, the interaction Lagrangian given by Eq. 20 makes several assumptions. The first is that there is in fact a well-defined capacitance per unit length. As is known from elementary electrostatics, the capacitance per unit length C of a wire of radius R and length l approaches zero as

$$C = \frac{2\pi\varepsilon_0}{\ln(l/R)}. \tag{29}$$

Hence, in order for a local capacitance to be defined that is independent of l, the length of the wire must be greater than the screening length l_s, which is some long distance cut-off for the Coulomb interaction. In this case, C is independent of the length and is given by

$$C = \frac{2\pi\varepsilon_0}{\ln(l_s / R)}. \qquad (30)$$

Such screening arises in our experimental situation because of the nanotube's proximity to a metallic gate, as shown in Fig. 7-2.

Another assumption implicit in using an interaction Lagrangian given by Eq. 20 is that the density varies slowly on the scale of l_s. Therefore, this interaction Lagrangian only captures effects due to the long-range Coulomb interaction. From elementary electrostatics, it can be shown that the long-range Coulomb interaction and the capacitance per unit length are related by

$$C = \frac{1}{\tilde{V}(k_s)}, \qquad (31)$$

Where $V(k_s)$ is the Fourier transform of the interaction potential evaluated near $k_s=2\pi/l_s$. For nanotubes, this neglect of the short-range Coulomb interaction is an excellent approximation[4]. At distances less than the diameter d of the nanotubes, the short range Coulomb interaction is effectively constant because the electrons' wavefunctions are spread out over the circumference. This suppresses Fourier components of the Coulomb interaction at momenta greater than $1/d$. Therefore, electron-electron scattering processes that involve the short-range part of the Coulomb interaction such as back scattering can be safely ignored compared to processes that involve the long-range part of the Coulomb interaction. Thus, we expect that the Lagrangian given above by Eq. 25 should give a good description of interacting electrons in nanotubes.

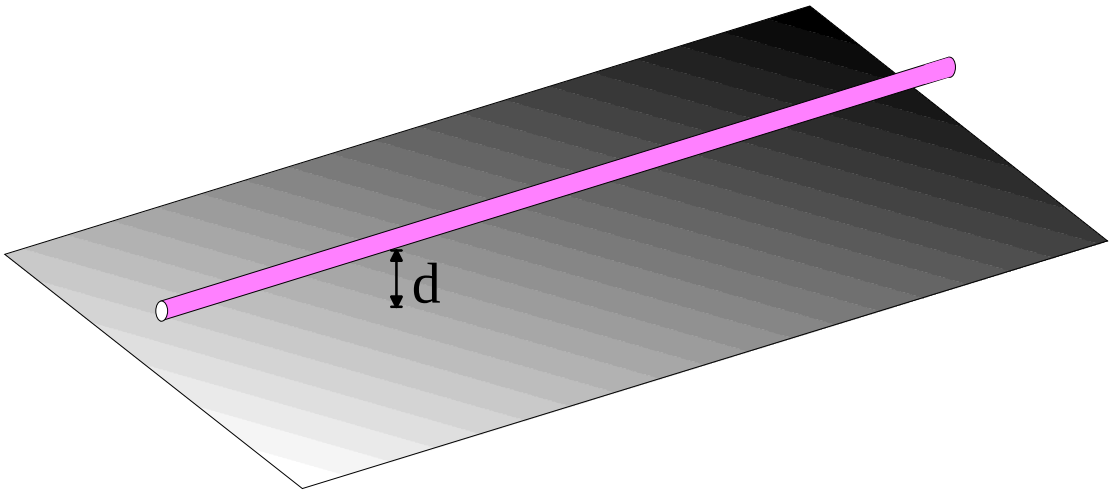

Figure 7-2: A carbon nanotube a distance *d* above a conducting plane. The presense of the conducting plane cuts off the long-range Coulomb interaction for distances greater than the screening length $l_s = 2d$.

7.4 Tunneling Density of States and the Semiclassical Approximation

With our faith in the simplified model confirmed, we can proceed to compute the tunneling density of states. In general, this is given by the expression

$$\rho_{tun}(E) = 2\pi \sum_n |< n \,|\, \psi^+(x) \,|\, 0 >|^2 \; \delta(E_n - E_0 - E)\,, \tag{32}$$

where $|n>$ are the exact eigenstates of the Hamiltonian and E_n are the energy eigenvalues, and $\Psi(x)$ is the electron annihilation operator. Using the identity

$$\delta(E_n - E_0 - E) = \frac{1}{\pi\hbar}\int_0^\infty e^{i(E+E_0-E_n)t/\hbar} dt\,, \tag{33}$$

yields the result

$$\rho(E) = \frac{1}{\pi\hbar}\,\mathrm{Re}\int_0^\infty e^{iEt/\hbar} < 0 \,|\, \psi(x,t)\psi^+(x,0) \,|\, 0 > dt\,. \tag{34}$$

The density of states is therefore related to the Fourier transform of the electron Green's function,

$$G(x,x',t') = < 0 \,|\, \psi(x',t')\psi^+(x,0) \,|\, 0 >\,, \tag{35}$$

evaluated at $x = x'$. This is the amplitude to introduce an electron into the system at $t = 0$ at x, and find it again at x at a later time $t = t'$. We will avoid the difficulties associated with quantum theory by utilizing the semiclassical approximation to compute the electron Green's function, which we will now briefly review (see *e.g.* [5].)

In general, the amplitude for a quantum system to make a transition between any two states can be calculated by summing the exponential of the classical action over all paths connecting the initial and final states. Explicitly, this reads

$$G(x,x',t) = < 0 \,|\, \psi(x',t)\psi^+(x,0) \,|\, 0 > = \int_{\text{paths}} \exp\left(\frac{i}{\hbar}\int_0^t L_{cl}\, dt'\right) Dx\,. \tag{36}$$

Since the action of the classical path is stationary, the dominant contribution to the sum over the paths comes from paths that are near the classical one. The contribution to the sum from highly non-classical paths is suppressed because of the large differences in phase between the contribution from neighboring paths. In the semiclassical approximation, one neglects the non-classical paths and assumes the propagator is given by

$$G(x,0;x',t) \sim \exp(\frac{i}{\hbar} S_{cl}) . \qquad (37)$$

Here, the propagator is known only up to an overall constant that depends on the size of the neighborhood of the paths sufficiently near the classical one to contribute to the sum over all paths.

A problem arises when one attempts to apply this approximation to computing tunneling processes: tunneling involves the motion of the system through classically forbidden configurations. Thus, it is not possible to find a classical path that connects the initial and final states. The way out is to replace t by $-i\tau$, and consider the imaginary time propagator, which is the analytic continuation of the real-time propagator:

$$G(\tau) = \int_{\text{paths}} \exp(\frac{-1}{\hbar}\int_0^\tau L_E d\tau')Dx \qquad (38)$$

where L_E is the so-called Euclidean Lagrangian, obtained by the transforming the real time Lagrangian by $t \rightarrow -i\tau$. This reverses the sign of the kinetic energy and thus the kinetic and potential energies appear in the Euclidean Lagrangian with the same sign. Pulling the minus sign out front yields $L_E = T+V$ in Eq. 38. This has the effect of inverting the potential, and the classically forbidden regions become allowed (and vice-versa.) Thus, we can now find a classical path in imaginary time that connects the initial

and final states. The imaginary time propagator in the semiclassical approximation becomes

$$G(\tau) \sim \exp(-\frac{1}{\hbar} S_{cl}) . \qquad (39)$$

Note that the transition amplitude decays exponentially with the action, which is the behavior one usually expects for tunneling through a classically forbidden configuration. In contrast with the real time formalism, the principle of least action is enforced by cutting off the non-classical paths by an exponentially small factor, rather than by canceling the contributions of neighboring paths by virtue of their rapidly varying phase.

7.5 Tunneling into a Nanotube

To compute the tunneling density of states, we now introduce a model for tunneling given in Fisher and Glazman[1]. In this model, the Luttinger liquid is interrupted by a barrier, as shown in Fig. 7-3. Tunneling proceeds through the barrier in a fast step that results in the sudden creation of a localized electron on the right hand side of the barrier. (This process leads to an overall pre-factor in the tunneling rate and we will neglect it in what follows.) However, at zero energy, the resulting configuration is classically forbidden. The tunneling process then proceeds by a slow phase in which the charge density relaxes to the ground state. Since the configuration is classically forbidden at all times during tunneling, we will use the imaginary time propagator to compute the Green's function. Also, as discussed previously, we will compute the Green's function using the semiclassical approximation[1]. By considering the action due to the charge relaxation on one side of the barrier only, we will compute the

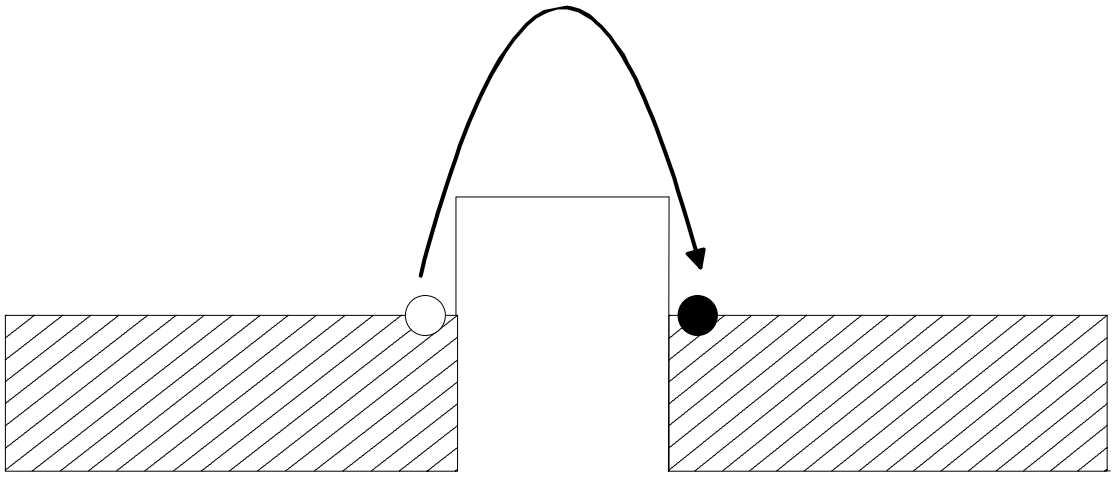

Figure 7-3: Luttinger liquid interrupted by a barrier, producing two tunnel-coupled half-infinte Luttinger liquids. The diagram depicts a tunneling process in which an electron is removed from the Luttinger liquid on the left, leaving a hole, and is added to the Luttinger liquid on the right.

tunneling density of states for adding an electron to the end of a single half-infinite Luttinger liquid.

To use this model for tunneling into a nanotube, we consider the creation of a localized electron in a specific mode, say $\rho_{\uparrow a}$. (The result is independent of the specific chosen mode.) This initial state requires the excitation all four of the modes ρ_{c+}, ρ_{c-}, ρ_{s+}, ρ_{s-}, and hence the initial conditions read:

$$\rho_{c+} = \rho_{c-} = \rho_{s+} = \rho_{s-} = \frac{1}{2} 2e\delta(x) = e\delta(x), \tag{40}$$

where the ½ comes from the normalization factor and the two comes from the fact that the density is only nonzero to the right of the barrier. The final state is given by

$$\rho_{c+} = \rho_{c-} = \rho_{s+} = \rho_{s-} = 0. \tag{41}$$

Now we must find the classical path that connects the initial state to the final state. The equations of motion are the imaginary-time wave equation (ITWE.) For the four modes, these read

$$\partial_t^2 \theta_{c/s,\pm} + v_{c/s,\pm}^2 \partial_x^2 \theta_{c/s,\pm} = 0. \tag{42}$$

with $v_{c/s,+}$ being either the Fermi velocity or the plasmon velocity as appropriate. Note that this differs from the usual wave equation by a change of sign. The general solution of this equation is

$$\theta_{c/s,\pm} = f(x + iv_{c/s,\pm}\tau) + g(x - iv_{c/s,\pm}\tau), \tag{43}$$

where $g(x)$ and $f(x)$ are arbitrary functions describing right and left propagating waves. This form, while very general, is somewhat difficult to match to the initial condition where $\theta(x,0)$ is proportional to the unit step function. There are many ways to proceed.

One way is motivated by the fact that the solution must connect a delta function density at $t = 0$ to zero density at $t \to \infty$. Thus, we try to find a solution that spreads out,

$$\theta = u\left(\frac{x}{v\tau}\right), \tag{44}$$

where u is an unknown function for which to solve. Putting this trial function into the ITWE yields the ordinary differential equation

$$(\eta^2 + 1)\ddot{u} + 2\eta\dot{u} = 0, \tag{45}$$

where $\eta = x/v\tau$. This equation is readily solved by integration to yield

$u = C_1 \tan^{-1}\eta + C_2$ where C_1 and C_2 are constants of integration. Note that this is a special case of Eq. 43 since

$$\tan^{-1}\left(\frac{x}{v\tau}\right) = \frac{-i}{2}\left[\ln(x - iv\tau) - \ln(x + iv\tau) - \pi i\right]. \tag{46}$$

It is straightforward to verify that

$$\theta_{c/s,\pm} = \frac{e}{\pi}\tan^{-1}\left(\frac{x}{v_{c/s,\pm}\tau}\right) \tag{47}$$

matches the initial conditions given by Eq. 40 and solves the ITWE. The density is then

$$\rho_{c/s,\pm}(x,t) = \frac{e}{\pi}\frac{v_{c/s,\pm}\tau}{x^2 + (v_{c/s,\pm}\tau)^2}. \tag{48}$$

This function is plotted in Fig. 7-4A and Fig. 7-4B.

Now that we have determined the classical path, we can determine the action of the classical path. This requires us to integrate the Lagrange density over space and time. As discussed previously, in imaginary time the Lagrange density is the sum of the potential and kinetic energies, rather than the difference. Therefore, the action will be the sum of the action due to the potential energy and the action due to the kinetic energy.

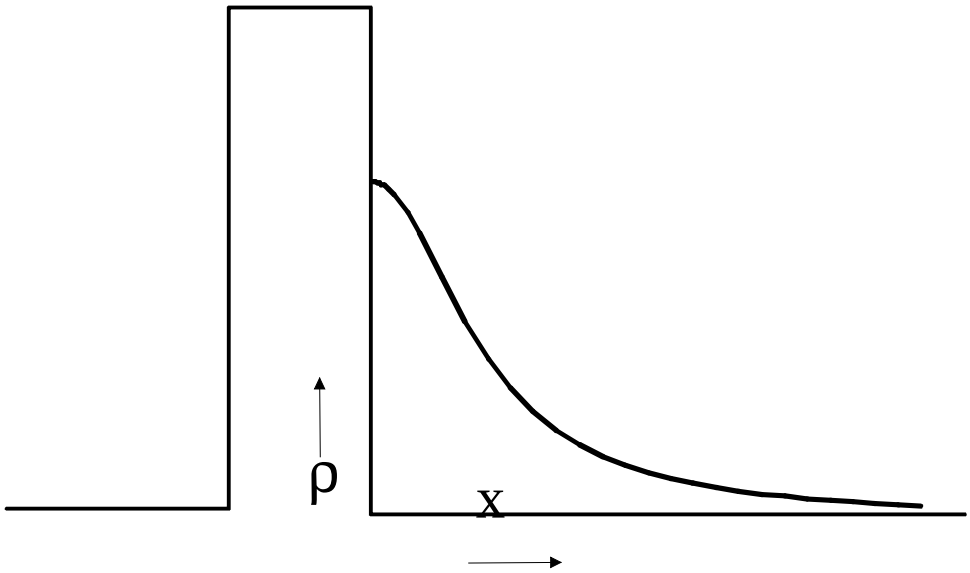

Figure 7-4A: A fast tunneling step through the barrier adds an electron and creates a local deformation in the charge density. At zero energy, this configuration is classically forbidden.

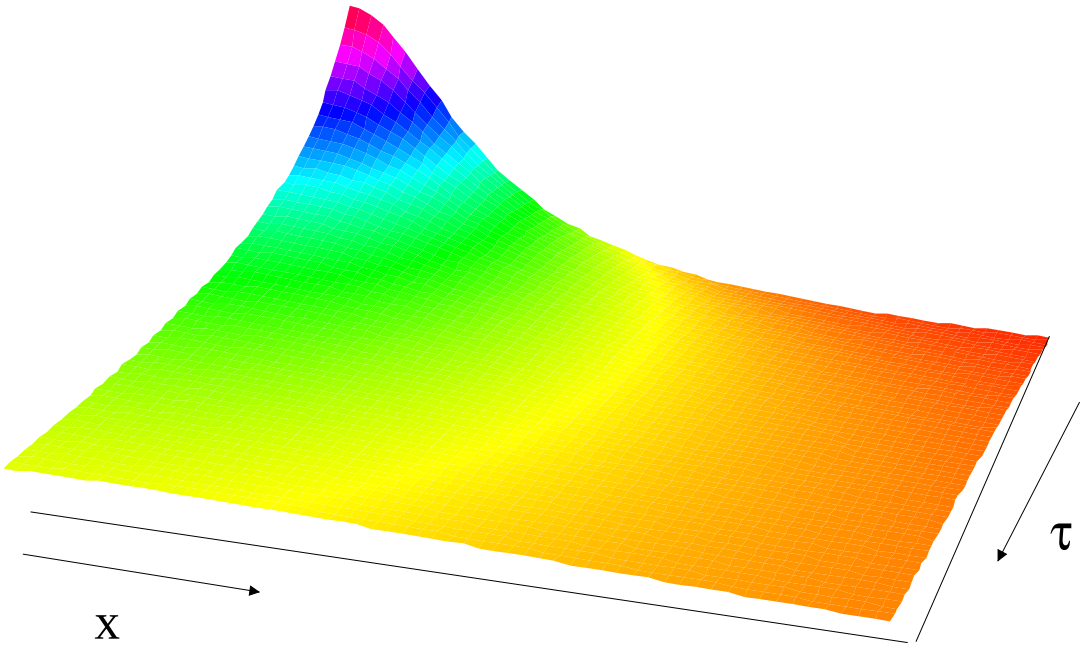

Figure 7-4B: Plot of the charge desnity as a function of position and (imaginary) time. As time evolves, the charge distribution spreads out and eventually relaxes to the ground state with $\rho = 0$.

The potential energy due to the deformation caused by the tunneling electron is the sum of the potential energies from each mode and is given by

$$V_{def}(\tau) = \frac{e^2}{2\pi^2} \sum_{c/s,\pm} g_{c/s,\pm}^{-1} \frac{h}{2e^2} v_{c/s,\pm} \int_0^\infty \left[\frac{v_{c/s,\pm}\tau}{x^2 + (v_{c/s,\pm}\tau)^2} \right]^2 dx$$

$$= \frac{h}{4\pi^2} \sum_{c/s,\pm} g_{c/s,\pm}^{-1} v_{c/s,\pm} \int_0^\infty \left[\frac{v_{c/s,\pm}\tau}{x^2 + (v_{c/s,\pm}\tau)^2} \right]^2 dx$$

$$= \frac{h}{16\pi\tau} \left(g_{c+}^{-1} + 3 \right). \tag{49}$$

Physically, this $1/\tau$ dependence arises because the density ρ goes as $1/\tau$ while the width W of the density packet goes as τ. Hence the $V_{def} \sim \rho^2 W \sim 1/\tau$. Considering zero total energy, the kinetic energy is equal to the potential energy and thus the action is

$$S(\tau) = 2\int_{\hbar/E_c}^{\tau} V_{def}(\tau')d\tau' \tag{50}$$

$$= \frac{h}{8\pi}(g_{c+}^{-1} + 3)\ln\frac{E_c\tau}{\hbar}. \tag{51}$$

Here, E_c is a high energy cut off on the order of e^2/a, where a is the typical electron spacing, or any other short range cutoff to the Coulomb interaction, *e.g.* the tube diameter. The imaginary time propagator is then given by

$$G(\tau) \sim \exp(-S(\tau)/\hbar) = \left(\frac{E_c\tau}{\hbar} \right)^{-\beta}, \tag{52}$$

with $\beta = (g_{c+}{}^{-1}+3)/4$. Hence, the exponential decay normally associated with tunneling through a classically forbidden configuration is cancelled by the logarithmic divergence of the action, resulting in power law behavior.

To arrive at the tunneling density of states we analytically continue the imaginary time propagator back to real time and compute the Fourier transform:

$$\rho_{tun}(E) \sim \frac{1}{\pi\hbar}\,\mathrm{Re}\int_0^\infty e^{iEt/\hbar}\left(\frac{iE_c t}{\hbar}\right)^{-\beta} dt \qquad (53)$$

The behavior with respect to energy can be determined via a change of variables $u = 2\pi Et/h$ (E>0). The integral then becomes

$$\rho_{tun}(E) \sim \frac{E^\alpha}{\pi}\,\mathrm{Re}\int_0^\infty e^{iu}\left(iE_c u\right)^{-\beta} du\,, \qquad (54)$$

where

$$\alpha = \alpha_{end} = \beta - 1 = (g_{c+}{}^{-1} - 1)/4. \qquad (55)$$

This implies that the differential conductance $dI/dV \sim V^\alpha$, and the conductance $G \sim T^\alpha$. Note that for arbitrarily weak interactions (for any $g_{c+} < 1$) the tunneling density of states vanishes at zero energy. This behavior is very different from that of the non-interacting 1DEG, where for energies near the Fermi level the tunneling density of states is constant. This is an essential distinction between the I1DEG and the non-interacting 1DEG.

Finally, this analysis is appropriate for determining the tunneling density of states when the electron tunnels into the end of the nanotube. If the electron tunnels into the middle, or bulk, the electron can spread out in two directions rather then one. As the electron spreads out, the charge density is half as much but spread out over twice the length as compared to the end tunneling case. Since the action is quadratic in the charge density but linear in the size of the charge packet, the action for tunneling into the middle is half the action for tunneling into the end. Hence, we expect that the tunneling exponent for tunneling into the middle should be approximately half of the exponent for

tunneling into the end. A more detailed calculation[2, 4] yields the result $\rho(E) \sim E^{\alpha}$, where

$$\alpha = \alpha_{bulk} = (g_{c+}^{-1} + g_{c+} - 2)/8. \quad (56)$$

For $g << 1$ where it is expected that semiclassical reasoning is most valid, α_{bulk} indeed approaches ½ the value of the α_{end}.

7.6 Limit of Many Modes and Connection to Coulomb Blockade Model

The above model for nanotubes with four conducting modes at E_F can be extended to the general case of N conducting modes at E_F[6]. The Hamiltonian for an N mode wire is given by

$$\mathrm{H} = \sum_n \frac{1}{2} L I_n^2 + \frac{1}{2\kappa} \rho_n^2 + \frac{1}{2C} \left(\sum_n \rho_n \right)^2, \quad (57)$$

Where ρ_n is the density of charge in the nth mode, and I_n is the corresponding current. Here as before, the interaction term depends only on the total charge. With a change of variables via a rotation to basis in which one mode is the total charge and the rest are orthogonal to this mode, this becomes

$$\mathrm{H} = \frac{1}{2} L I_{c+}^2 + \frac{1}{2\kappa} \rho_{c+}^2 + \frac{N}{2C} \rho_{c+}^2 + \sum_{n=1}^{n=N-1} \frac{1}{2} L I_{c0n}^2 + \frac{1}{2\kappa} \rho_{c0n}^2, \quad (58)$$

where ρ_{c+} is the charged mode, I_{c+} the corresponding current, ρ_{c0n} the nth neutral mode, and I_{c0n} the nth neutral current. Note that because the change in variables used here is an orthonormal transformation, the physical charge is related to the ρ_{c+} by $\rho_{physical} = N^{1/2} \rho_{c+}$. The sum in the Eq. 58 runs over the N-1 neutral modes. In this basis, the N modes

behave independently. The interaction strength g can be computed for each mode. The result is that

$$g_{c+} = \frac{v_F}{v_p} = (1 + \frac{N\kappa}{C})^{-\frac{1}{2}} \tag{59}$$

for the charged mode, and $g_{c0n} = 1$ for the N-1 neutral modes.

The tunneling density of states can be calculated using the same method employed in the previous section with the result that $\alpha_{end} = (g_{c+}{}^{-1}\text{-}1)/N$. In the limit where $N>>1$, $g_{c+} \sim (1/N)^{1/2}$. Thus we have $\alpha \sim (1/N)^{1/2}$ to leading order. Hence as the number of modes tends to infinity, the behavior of the wire tends toward the non-interacting result $\alpha = 0$. Physically, this occurs because in the limit $N>>1$, the tunneling action is dominated by the spreading out of the neutral modes, and the contribution from the charged mode becomes comparatively negligible. The result is that the tunneling density of states is thereby determined by the non-interacting neutral modes, which gives rise to the ohmic behavior expected for tunneling into a system of non-interacting electrons.

Finally, we note the connection between this theory and the theory of Coulomb blockade of tunneling in a resistively isolated tunnel junction (CB theory). (For review, see e.g. [7]). In the CB theory at low energies the tunneling rate goes as a power law in the applied bias,

$$\frac{dI}{dV} \sim V^{\alpha}, \tag{60}$$

where the exponent α is determined by the isolating impedance Z:

$$\alpha = \frac{2e^2}{h} Z . \tag{61}$$

As we will now show, this model is equivalent to the model discussed earlier in the limit of many modes. In that model, α is given by:

$$\alpha = \frac{1}{N}\left(\frac{1}{g_{c+}} - 1\right) = \frac{1}{N}\left[\left(1 + \frac{N\kappa}{C}\right)^{1/2} - 1\right] = \frac{1}{N}\left[\left(1 + \frac{N}{LCv_F^2}\right)^{1/2} - 1\right] \qquad (62)$$

In the limit that N>>1, to leading order

$$\alpha = \sqrt{\frac{\kappa}{NC}} = \frac{1}{v_F}\sqrt{\frac{1}{NLC}} = \frac{2e^2}{h}\sqrt{\frac{L}{NC}}\,. \qquad (63)$$

This agrees with Eq. 61 provided the characteristic impedance of a multi-mode wire is given by $Z = (L/NC)^{1/2}$ in the limit where N>>1. To show this, we note that only the charged mode couples to an external electric field[8]. Hence the impedance of the neutral modes is infinite and the impedance of the wire is determined solely by the finite impedance of the charged mode. The Hamiltonian for the charged mode may be written in terms of the physical charge $\rho = N^{1/2}\rho_{c+}$, and the corresponding current I. The result is

$$\mathrm{H} = \frac{1}{2N}LI^2 + \left(\frac{1}{2N\kappa} + \frac{1}{2C}\right)\rho^2\,. \qquad (64)$$

In an ordinary electromagnetic transmission line with capacitance per unit length C_0 and inductance per unit length L_0, the characteristic impedance Z_0 is given by $Z_0 = (L_0/C_0)^{1/2}$. By analogy, the characteristic impedance Z of the multi-mode wire is given by

$$Z = \sqrt{\frac{L}{N}\left(\frac{1}{C} + \frac{1}{2N\kappa}\right)}\,. \qquad (65)$$

In the limit N>>1, to leading order in N, this approaches

$$Z = \sqrt{\frac{L}{NC}}\,, \qquad (66)$$

and thus the theory given by Eq. 57 reproduces the results of the CB theory in the limit where $N>>1$.

7.7 Summary

In conclusion, we have presented a simplified phenomenological model for a I1DEG and applied it to computing the tunneling density of states of metallic carbon nanotubes. This tunneling density of states shows power law behavior with an exponent that depends on whether the electron tunnels into the end of the nanotube or into the middle. In particular, $\rho(E) \sim E^{\alpha}$, where $\alpha = (g_{c+}{}^{-1}-1)/4$ in the case of tunneling into the end, and $\alpha = \alpha_{bulk} = (g_{c+}{}^{-1} + g_{c+}-2)/8$ in the case of tunneling into the middle. This power-law vanishing of the tunneling density of states at low energies is a striking feature that signifies the correlated nature of the I1DEG.

References

1 M. P. A. Fisher and L. I. Glazman, in *Mesoscopic electron transport*, edited by L. L. Sohn, L. P. Kouwenhoven and G. Schoen (Kluwer Academic Publishers, Dordrecht ; Boston, 1997).

2 R. Egger and A. O. Gogolin, Phys. Rev. Lett. **79**, 5082 (1997).

3 R. Egger and A. O. Gogolin, European Physical Journal B **3**, 281 (1998).

4 C. Kane, L. Balents, and M. P. A. Fisher, Phys. Rev. Lett. **79**, 5086 (1997).

5 R. Shankar, *Principles of Quantum Mechanics* (Plenum, New York, 1994).

6 K. A. Matveev and L. I. Glazman, Phys. Rev. Lett. **70**, 990 (1993).

7 G.-L. Ingold and Yu. V. Nazarov, in *Single charge tunneling: Coulomb blockade phenomena in nanostructures*, edited by H. Grabert and M. H. Devoret (Plenum Press,, New York :, 1992).

8 K. A. Matveev and L. I. Glazman, Physica B **189**, 266 (1993).

Chapter 8

Luttinger Liquid Behavior in Carbon Nanotubes

Marc Bockrath*, David H. Cobden*, Jia Lu*, Andrew G. Rinzler[+], Richard E. Smalley[+], Leon Balents[#] and Paul L. McEuen*

*Department of Physics, University of California and Materials Sciences Division, Lawrence Berkeley National Laboratory, Berkeley, California, 94720

[+]*Center for Nanoscale Science and Technology, Rice Quantum Institute, and Department of Chemistry and Physics, MS-100, Rice University, P.O. Box 1892, Houston, TX 77251*

[#]*Institute for Theoretical Physics, University of California, Santa Barbara, CA 93106-4030*

Electron transport in conductors is usually well described by Fermi-liquid theory, which assumes that the energy states of the electrons near the Fermi level E_F are not qualitatively altered by Coulomb interactions. In one-dimensional systems, however, even weak Coulomb interactions cause strong perturbations. The resulting system, known as a Luttinger liquid, is predicted to be distinctly different from its two- and three-dimensional counterparts[1]. For example, tunneling in to a Luttinger liquid at energies near the Fermi level is predicted to be strongly suppressed, unlike in two- and three-dimensional metals. Experiments on one-dimensional semiconductor wires[2,3] have been interpreted using Luttinger-liquid theory, but an unequivocal verification of the theoretical predictions has not yet been obtained. Behavior consistent with a chiral Luttinger liquid has been observed in fractional quantum Hall conductors[4-6], although questions remain about the connection between theory and experiment. Electrically conducting single-walled carbon nanotubes (SWNTs) represent quantum wires[7-10] that may exhibit Luttinger-liquid behavior[11,12]. Here we present measurements of the conductance of bundles ('ropes') of SWNTs as a function of temperature and voltage that agree with predictions for tunneling into a Luttinger liquid. In particular, we find that the conductance and differential conductance scale as power laws with respect to temperature and bias voltage, respectively, and that the functional forms and the exponents are in good agreement with theoretical predictions.

Since the initial discovery of SWNTs, experiments have revealed a great deal about their electronic properties. STM measurements of individual tubes have verified that they are either 1D semiconductors or conductors, depending upon their chirality[7,8]. Electrodes have also been attached to nanotubes and ropes of nanotubes

to probe transport. These electrodes make tunneling contacts to the tubes and, for conducting tubes, the resulting structure behaves as a 1D quantum dot. It was found that for ropes transport was typically dominated by a single nanotube in the rope[9]. This is reasonable since the majority of the tubes comprising a rope are insulating at low temperatures[7,8] Measurements of such devices have been used to study the charging energy, level spacing, and spin state of a nanotube[9,10,13,14].

The devices used in these previous experiments had two distinct geometries, one which contacted the ends of a tube and one which contacted the bulk, as is discussed in the legend to Fig. 1. Here, we explore the transport properties of rope samples in both of the geometries. Fig. 1 shows the linear-response two-terminal conductance, G, versus gate voltage, V_g, for a bulk-contacted metallic rope. At low temperatures, it exhibits a series of Coulomb oscillations[15] that occur each time that an electron is added to a nanotube within the rope. From the temperature dependence, we find that the charging energy U for this sample is 1.9 meV. For $k_BT > U$ (i.e. $T > 20$ K), the Coulomb oscillations are nearly completely washed out, and the conductance is independent of gate voltage. A plot of the conductance vs. temperature in this regime is shown in the inset. The conductance drops steeply as the temperature is lowered, extrapolating to $G = 0$ at $T = 0$.

Results for a number of samples are shown in Fig. 2, where the G versus T is plotted on a log-log scale (solid lines). Fig. 2(a) shows data for end-contacted ropes, whereas Fig. 2(b) shows the data for bulk-contacted ropes. The measured data (solid lines) shows approximate power law behavior for the four samples shown. However, the range of temperature over which the power law behavior occurs is limited by the effects

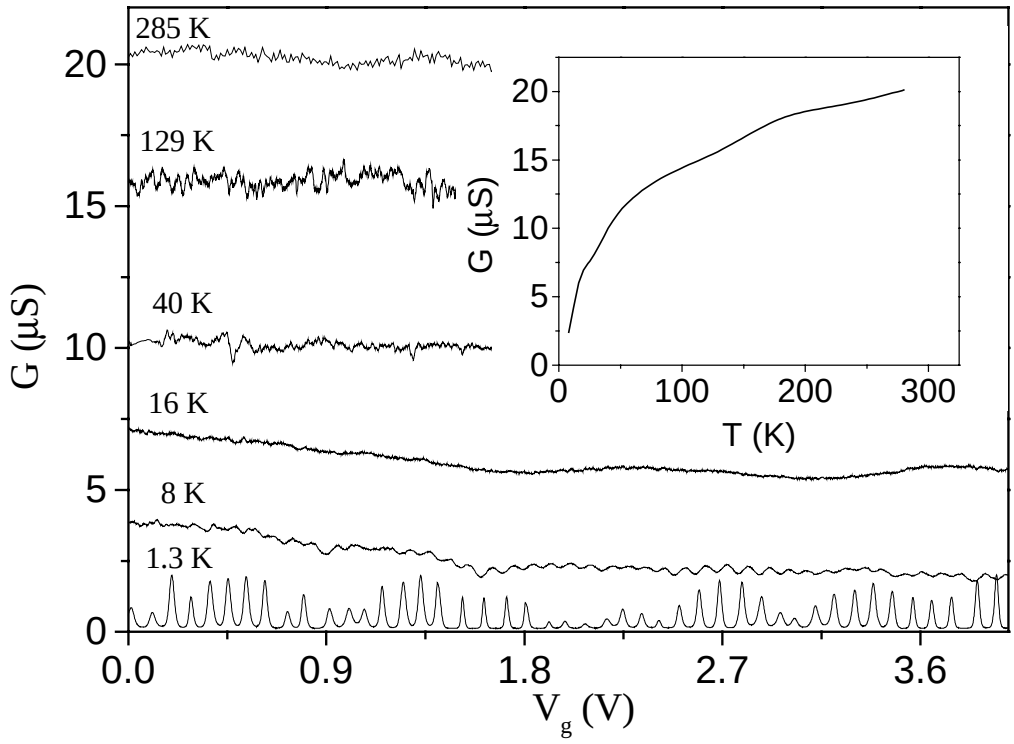

Figure 8-1: The two-terminal linear-response conductance G vs. gate voltage V_g for a bulk-contacted metallic rope at a variety of temperatures. The data show significant temperature dependence for energy scales above the charging energy that cannot be explained by the Coulomb blockade model. Inset: Average conductance plotted as a function of temperature T. The devices used in these experiments are made in one of two ways. In both methods, SWNTs are deposited from a suspension in dichloroethane onto 1-μm thick SiO_2 that has been thermally grown on a degenerately doped Si wafer. The degenerately doped silicon substrate is used as a gate electrode. AFM imaging reveals that the diameter of the ropes vary between 1 and 10 nm. In the first method[9], chromium-gold contacts are applied over the top of the nanotube rope using electron beam lithography and lift-off. From measurements of these devices in the Coulomb blockade regime, we conclude that the electrons are confined to the length of rope between the leads. This implies that the leads cut the nanotubes into segments, and transport involves tunneling into the ends of the nanotubes ("end-contacted"). In the second method[10], electron beam lithography is first used to define leads, and ropes are deposited on top of the leads. Samples were selected that showed Coulomb blockade behavior at low temperatures with a single well-defined period, indicating the presence of a single dot. The charging energy of these samples indicates a dot with a size substantially larger than the spacing between the leads, as found by Tans, et al.[10] Transport thus occurs by electrons tunneling into the middle, or bulk, of the nanotubes ("bulk-contacted").

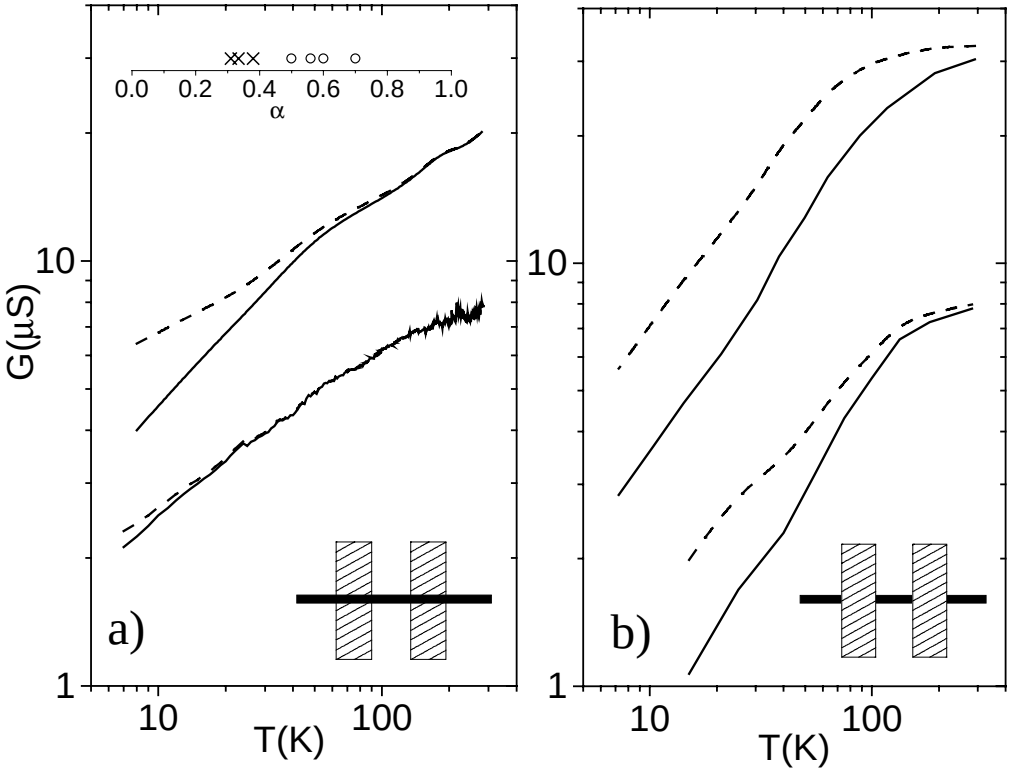

Figure 8-2: Conductance *G* plotted against temperature *T* for individual nanotube ropes. The data are plotted on a log-log scale. Figure 2a shows data for ropes that are deposited over pre-defined leads (bulk-contacted), whereas Fig. 2b shows the data for ropes that are contacted by evaporating the leads on top of the ropes (end-contacted). Sketches depicting the measurement configuration are shown in the lower right insets. The plots show both the bare data (solid line) and the data corrected for the temperature dependence expected from the Coulomb blockade (CB) model (dashed line). We correct the data by dividing the measured *G(T)* by the theoretically expected temperature dependence in the CB model. This correction factor only depends upon U/k_BT, and, since *U* can be independently measured from the temperature dependence of the Coulomb oscillations, the correction procedure requires no adjustable parameters. If the CB were the only source of the temperature dependence, the dashed lines would be horizontal. Instead they have a finite slope, indicating an approximate power-law dependence on *T*. The upper left inset to Figure 2(a) shows the power-law exponents inferred for a variety of samples. Open circles denote end-contacted devices, while crosses denote bulk-contacted ones.

of Coulomb blockade at low temperatures. After correcting for the known temperature dependence due to the Coulomb blockade[15], the corrected data (dashed lines) shows power law behavior over a greater range, with slightly different exponents. Above T~100 K, G begins to saturate for some samples. This saturation is observed in many, but not all, of the samples studied.

Focusing on the corrected data, the bulk-contacted samples show approximate power law behavior from 8 – 300 K with exponents $\alpha_{bulk} \approx 0.33$ and 0.38. The end-contacted samples show approximate power law behavior from 10 - 100 K with exponents $\alpha_{end} \approx 0.6$ for both samples. The upper inset to Fig. 2(a) shows the exponents determined from the temperature dependence for a variety of samples. Exponents marked with an 'x' and 'o' are for bulk- and end- contacted tubes, respectively. The bulk-contacted samples show a systematically lower exponent than end-contacted devices, with $\alpha_{end} \sim 0.6$ and $\alpha_{bulk} \sim 0.3$.

Figure 3 shows the measured differential conductance *dI/dV* of these devices as a function of the applied bias *V*. The upper left inset to Fig. 3(a) shows results for a bulk-contacted device at different temperatures, plotted on a log-log scale. At low biases, *dI/dV* is proportional to a (temperature-dependent) constant – *G(T)* from Figure 2. At high biases *dI/dV* increases with increasing *V*. The curves at different temperatures fall onto a single curve in the high bias regime. Since this curve is roughly linear on a log-log plot, it implies that the differential conductance is described by a power law, $dI/dV \sim V^{\alpha}$, where $\alpha = 0.36$. At the lowest temperature T=1.6 K, this power law behavior occurs over two decades in *V*, from 1 mV < *V* < 100 mV.

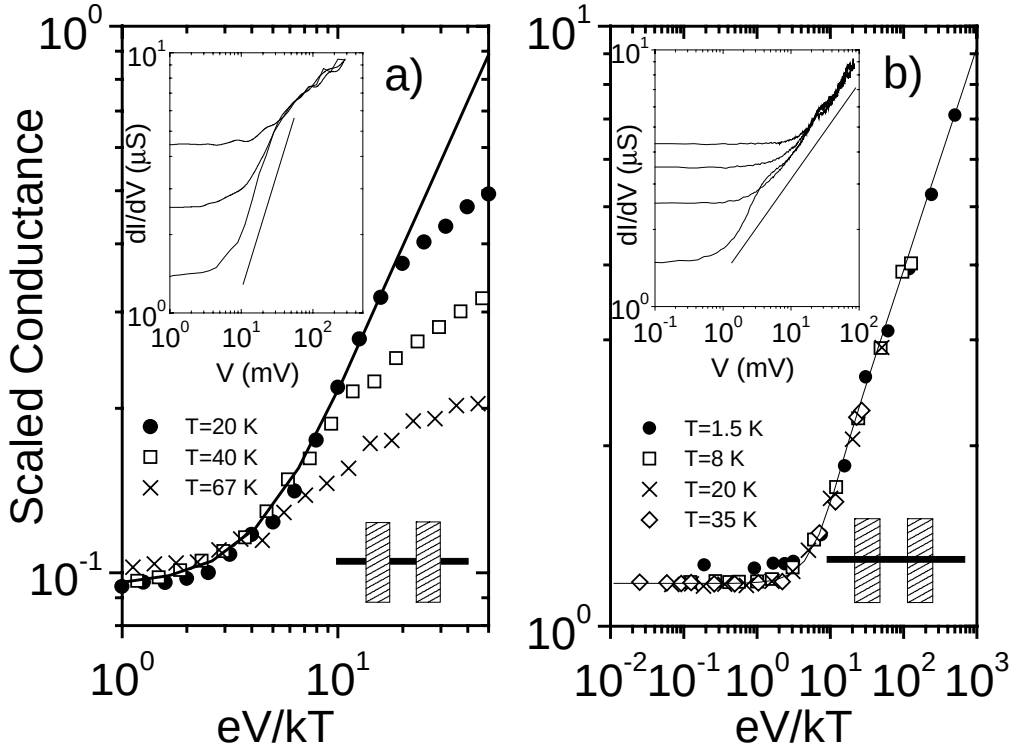

Figure 8-3: The differential conductance *dI/dV* measured at various temperatures. Figure 3a inset: *dI/dV* curves taken on a bulk-contacted rope at temperatures *T*=1.6 K, 8 K, 20 K, and 35K. Figure 3b inset: *dI*/*dV* curves taken on an end-contacted rope at temperatures *T*=20 K, 40 K, and 67K. In both insets, a straight line on the log-log plot is shown as a guide to the eye to indicate power-law behavior. The main panels show these measurements collapsed onto a single curve using the scaling relations described in the text. The solid line is the theoretical result fit to the data using γ as a fitting parameter. The values of γ resulting in the best fit to the data are $\gamma = 0.46$ in (a) and $\gamma = 0.63$ in (b).

The upper left inset to Fig. 3(b) shows *dI/dV* as a function of *V* for an end-contacted sample at several temperatures. The conductance is again a temperature-dependent constant at low biases e$V << k_BT$, whereas at higher biases *dI/dV* increases. The high bias data follows an approximate power law before rolling off to reduced slope for $V > 30$ mV. While the range of data is too small to conclude that a power law accurately describes the behavior at intermediate voltages, if a straight line is fit to the range 9 mV$< V <$ 32 mV the exponent obtained is $\alpha = 0.87$.

We now discuss the possible origins this approximate power law behavior. One possible explanation is that the tunnel barriers are strongly energy-dependent, with increased transparency at high energies. This would lead, e.g. to activated transport: $G \sim \exp(-\Delta/k_BT)$ over the barrier. However, the fact that the temperature dependence extrapolates to $G = 0$ at $T = 0$ (Figure 1 inset) is inconsistent with this functional form.

Another potential explanation is that transport occurs through multiple dots in series formed by disorder[16] or by barriers produced when the nanotubes bend over the lithographically defined contacts[17]. We rule this possibility out however, as we have chosen to study only samples where a single dominant period for the Coulomb oscillations is observed at low temperatures. This indicates the existence of only a single dot.

Having excluded these possibilities, let us consider whether the behavior can be explained by the predictions of Luttinger Liquid (LL) theory. A LL is a one-dimensional correlated electron state characterized by a parameter *g* that measures the strength of the interaction between electrons. For any $g \neq 1$, the low energy excitations

of the system are not all weakly interacting quasiparticles, and the Fermi liquid theory used to describe conventional metals is not appropriate.

In SWNTs, the long-range Coulomb interaction between electrons is expected to yield an LL with $g < 1$[11,12] For a finite length tube or rope, the Luttinger parameter g is given by:

$$g = [1 + \frac{2U}{\Delta}]^{-1/2} \qquad (1)$$

where $U = e^2/C$ is the charging energy of the tube and $\Delta = \pi \hbar v_F/2L$ is the single-particle level spacing (the two 1D subbands of the nanotube are assumed to be non-degenerate). From previous measurements and theoretical estimates[9,10] $U/\Delta \sim 6.$, yielding an expected Luttinger parameter g(theory) ~ 0.28.

Tunneling of an electron into a LL is dramatically different than tunneling into Fermi liquid. For a Fermi liquid, an energy-independent tunneling amplitude is expected for energies near E_F, where E_F is the Fermi level. This yields a temperature- and bias-independent tunneling conductance. For a clean LL on the other hand, the tunneling amplitude is predicted to vanish as a power law in E-E_F. This leads to a power-law variation of G with T at small biases $(eV << k_BT)$:

$$G(T) \sim AT^{\alpha} \qquad (2)$$

or with V at large biases $(eV >> k_BT)$:

$$dI/dV \sim V^{\alpha} \qquad (3).$$

The exponent of these power laws depends on the number of 1D channels[18] and whether the electron tunnels into the bulk or the end of the LL. For a SWNT with four conducting modes at E_F, the exponents are[11,12]:

$$\alpha_{end} = (g^{-1} - 1) / 4 \quad (4a)$$

$$\alpha_{bulk} = (g^{-1} + g - 2) / 8. \quad (4b)$$

Using equations 1 and 4, we obtain α_{end}(theory) = 0.65 and α_{bulk}(theory) = 0.24.

To compare the theoretical predictions for tunneling into an isolated nanotube through a single barrier to the experimental geometry where ropes are connected by two contacts, we must make two assumptions. First, we assume that transport in the rope is dominated by a single metallic tube, as discussed previously. Preliminary theoretical studies of ropes composed of SWNTs with a relatively small fraction of metallic tubes support this assumption. These studies find that the only significant inter-tube coupling is electrostatic. Such an interaction will introduce extra screening of the Coulomb interaction but, because of the weak (logarithmic) dependence of g on the screening length, the LL predictions are essentially unchanged. Second, we assume that the tunnel resistances into and out of the tube are the dominant resistances in the system. The circuit thus consists of two tunnel junctions in series, with the current response of each junction is described by equations 1-4. Note that the voltage drop across the highest impedance junction will be some fraction γ of the total applied bias V, where $1/2 \leq \gamma \leq 1$. If the barriers are equal, the voltage will divide equally between these junctions and $\gamma = 1/2$. Alternately, if the resistance of one junction dominates, $\gamma = 1$.

With these assumptions, the approximate power law behavior as a function of T or V observed in Figures 2 and 3 then follows from Eq.s 1-4. The predicted values of

the exponents are also in very good agreement with the experimental values. This agreement may be somewhat fortuitous due to the experimental uncertainty in the value of U/Δ and complexities associated with the screening of the Coulomb interaction by the metallic leads[11,12] Nevertheless, the measurements are both qualitatively and quantitatively described by LL theory. Remarkably, power-law behavior in T is observed up to 300 K in the bulk-contacted samples, indicating that nanotubes are Luttinger Liquids even at room temperature.

At present, we do not understand the origins of the high-energy saturation observed in the end-contacted tubes. One possibility is that, at high energies, electrons can tunnel in both directions and hence the end-contacted tubes behave as bulk-contacted tubes, with a correspondingly lower exponent. Future experiments are necessary to clarify this issue.

The LL theory makes an additional prediction for this system. The differential conductance for a single tunnel junction is given by a universal scaling curve[19,20]:

$$\frac{dI}{dV} = AT^{\alpha}\cosh\left(\gamma\frac{eV}{2k_BT}\right)\left|\Gamma\left(\frac{1+\alpha}{2}+\gamma\frac{ieV}{2\pi k_BT}\right)\right|^2 \qquad (5)$$

where $\Gamma(x)$ is the gamma function, γ is the constant introduced earlier that takes into account the voltage division between the two tunnel junctions, and A is an arbitrary constant. This equation assumes that the leads are at T = 0 K. For leads at a finite temperature, dI/dV is given by the convolution of Eq. 5 and the derivative of the Fermi distribution: $df/dE = \frac{1}{4k_BT}\sec h^2(\gamma eV/2k_BT)$.

If the above scaling relation is correct, it should be possible to collapse the data at different temperatures onto a single universal curve. To do this, the measured dI/dV at

each temperature was divided by T^{α} and plotted against eV/k_BT, as shown in the main body of Figs. 3(a) and 3(b). For both geometries, the scaled conductance is constant at as eV/k_BT approaches zero, but above $eV/k_BT \sim 7$, the scaled curve begins to increase. The data collapses quite well onto a universal curve for the bulk-contacted device, Fig. 3(a), over the entire bias range. For the end-contacted device, the data deviates from power-law behavior for biases $V > 30$ mV as discussed previously. This is reflected in Fig. 3(b) in a roll-off that occurs at lower values of eV/k_BT as the temperature is increased.

The solid lines in Fig. 3(a) and 3(b) are a plot of the curve obtained by fitting Eq. 5 (convolved with *df/dE)* to the data, with γ as a fitting parameter. The theory fits the scaled data reasonably well, especially for the bulk-contacted tube. For the samples studied, the inferred values of γ fall, within error bars, of the allowable range ($0.5 < \gamma < 1$) for two barriers in series. This indicates that energy scale at which the differential conductance makes the transition from a constant to power law behavior is well described by the theory.

Taken as a whole, the data shown in Fig. 2 and Fig. 3 provide strong evidence that the electrons in metallic carbon nanotubes constitute a Luttinger liquid. Future work will test other predictions of the LL theory, such as tunneling between LLs in end-to-end[1] and in crossed geometries[21]

We thank Steven Louie, Marvin Cohen, Dung-hai Lee, Alex Zettl, and Antoine Georges for useful discussions. This work was supported by DOE (Basic Energy Sciences, Materials Sciences Division, the sp^2 Materials Initiative). L. Balents was supported by the NSF.

References

A similar version of Chapter 8 appeared in Nature **397** 598 (1999).

1 M. P. A. Fisher and A. Glazman, Mesoscopic Electron Transport (Kluwer Academic Publishers,) Boston, (1997).

2 S. Tarucha, T. Honda, and T. Saku, *Solid State Comm.* **94**, *413 (1995).*

3 A. Yacoby *et al.,* Phys. Rev. Lett. **77,** 4612 (1996).

4 F. P. Milliken, C. P. Umbach, and R. A. Webb, Solid State Comm. **97**, 309 (1996).

5 A. M. Chang, L. N. Pfeiffer, and K. W. West, Phys. Rev. Lett.. **77**, 2538 (1996).

6 M. Grayson, *et al.,* Phys. Rev. Lett., **80**, 1062 (1998).

7 J.W.G. Wildoer, *et al*., Nature **391**, 59 (1998).

8 T. W. Odom, J. Huang, P. Kim, and C. M. Lieber, Nature **391**, 62 (1998).

9 M. Bockrath, *et al.,* Science **275,** 1922 (1997)**.**

10 S. J. Tans, *et al.,* Nature **386**, 474 (1997).

11 R. Egger and A. Gogolin, Phys. Rev. Lett. **79**, 5082 (1997).

12 C. Kane, L. Balents, and M. P. A. Fisher, Phys. Rev. Lett. **79**, 5086 (1997).

13 D. H. Cobden, *et al.,* Phys. Rev. Lett. **81**, 681 (1998).

14 S. J. Tans, M. H. Devoret, R. J. A. Groeneveld, and C. Dekker, Nature **394,** 761 (1998).

15 H. Grabert and M. H. Devoret, Single Charge Tunneling: Coulomb Blockade Phenomena in Nanostructures (Plenum Press, New York, 1992).

16 C. L. Kane and E. J. Mele, Phys. Rev. Lett. **78**, 1932 (1997).

17 A. Bezryadin, A. R. M. Verschueren, S. J. Tans, and C. Dekker, Phys. Rev. Lett. **80**, 4036 (1998).

18 K. A. Matveev and L. I. Glazman, Phys. Rev. Lett. **70,** 990 (1993)

19 M. P. A. Fisher and A. Dorsey, Phys. Rev. Lett. **54**, 1609 (1985).

20 H. Grabert and U. Weiss, Phys. Rev. Lett. **54**, 1605 (1985).

21 A. Komnik and R. Egger, Phys. Rev. Lett., **80**. 2881 (1998)

Chapter 9

Summary

Recent advances have made the bulk production of ~1 nm diameter single-walled carbon nanotubes (SWNTs) possible. These SWNTs may be considered as made from a rolled-up single sheet of graphite. They are interesting for a variety of reasons, and since their discovery, much effort has been made toward studying their mechanical, chemical, and electrical properties. This thesis work has been focused on the electrical properties of these SWNTs, which have been predicted to be either 1D metals or 1D semiconductors depending on the precise way in which the tube is rolled from the graphite sheet.

To study the electrical properties of SWNTs experimentally we have attached leads to ~1 μm long nanotubes using electron beam lithography. These leads are patterned on an oxidized degenerately doped Si wafer, which is used as a gate to modulate the charge density on the nanotubes, similar in operation to a MOSFET.

How these devices operate depends on whether the SWNTs are metallic or semiconducting. In metallic tubes, we have found that at low temperatures and biases a nanotube behaves like a 1D quantum dot. The number of electrons on the nanotube is discrete, and sharp peaks in the conductance are observed as the gate voltage is varied, corresponding to the addition of a single electron to the nanotube. We have also performed transport spectroscopy on the metallic tubes and have observed resonant

tunneling through the individual quantum levels of the electrons in the nanotubes. From these measurements, we have determined the charging energy and mean level spacing for many nanotube dots. We have found that the ratio of the charging energy to level spacing is ~6 independent of the length of the dot, giving direct experimental evidence for carbon nanotubes' 1D nature. The size of the dots as estimated from the charging energy can be quite large; the largest we have studied is ~10 μm in length. Because in 1D the elastic mean free path is on the order of the localization length, this indicates that the mean free path l_m in metallic tubes can be on the micron length scale. Finally, we have used transport spectroscopy techniques to study the electron spin states in an applied magnetic field.

These quantum-dot effects arise from the finite size of the nanotube. However, in an infinite 1D system electron-electron (e-e) interactions are predicted to strongly modify the 1D electron gas away from that of a conventional Fermi liquid. This strongly correlated state is known as a Luttinger liquid (LL). In order to observe effects arising from the e-e interactions, we therefore probed the nanotubes at energy scales well above the charging energy and level spacing. In our transport measurements, when the temperature T and/or bias V was well above the charging energy and level spacing, power law behavior of the conductance as a function of temperature or bias voltage was observed: $G \sim T^{\alpha}$ and $dI/dV \sim V^{\alpha}$. Both the power-law functional forms and the inferred exponents are in good agreement with theoretical predictions for tunneling into a LL. This is significant because it has shows that SWNTs constitute a very clean 1D system in which LL effects may be observed, thus opening new possibilities for the study of a 1D interacting electron gas.

We now turn to semiconducting nanotubes. These nanotubes have been found by others to show p-type transistor behavior, turning on at negative gate voltages and turning off at positive gate voltages. We have extended this work by showing that n-type transistors can be made from nanotubes that are doped with potassium.

Low temperature measurements of semiconducting nanotubes reveal behavior consistent with transport through multiple quantum dots. The charging energy of these dots is ~100 meV, which corresponds to a dot size of ~100 nm. This indicates that the mean free path l_s in semiconducting tubes is also typically on the order of ~100 nm. Thus we find that for most of the devices we have studied $l_s << l_m$. We believe that this results from details of the band structure of metallic and semiconducting tubes that prohibits backscattering from long range disorder in metallic tubes.

In conclusion, we have shown that carbon nanotubes constitute a nearly perfect system in which to study the physics of electrons in 1D. This relatively new field (~3 years old) has already seen tremendous progress. Despite this, the prospects for exciting developments remains undiminished. The extremely high aspect ratio of SWNTs makes them an ideal bridge between the micron scale world and the nanometer scale world. People have just begun to explore the uses of nanotubes as nanomechanical oscillators or scanned probe tips[1, 2]. In addition, future work will no doubt continue to explore their fascinating transport properties. SWNTs are truly a material for the new millenium.

References

1 H. Dai. *et al.*, Nature, **384** 147 (1996).

2 P. Poncharal *et al.*, Science,. **283** 1513 (1999).